Functional integration of newborn neurons into established neuronal circuits in the zebrafish larva visual system

Jonathan Boulanger-Weill

THÈSE DE DOCTORAT DE
l'UNIVERSITÉ PIERRE ET MARIE CURIE

Spécialité

Neurosciences

Ecole doctorale Cerveau Cognition Comportement

Présentée par

Jonathan Boulanger-Weill

Pour obtenir le grade de

DOCTEUR de l'UNIVERSITÉ PIERRE ET MARIE CURIE

Sujet de la thèse :

Functional integration of newborn neurons into established neuronal circuits in the zebrafish larva visual system

soutenue le 21 septembre 2015

devant le jury composé de :

Mr. German Sumbre	Directeur de thèse
Mr. Aristides Arrenberg	Rapporteur
Mr. Jean-Stéphane Joly	Rapporteur
Mr. Filippo Del Bene	Examinateur
Mr. Pierre-Marie Lledo	Examinateur

Acknowledgements

Je voudrais remercier German, pour m'avoir laissé la liberté de m'exercer à chercher. Au laboratoire, pour m'avoir apporté tant jour après jour. A Adrien pour cette complicité devenue essentielle. A Seba pour m'avoir appris l'usage des boucles, accolades et crochets. A Vero, pour son exemple de force et de tempérance. A Benjamin, pour sa générosité infinie et toujours oubliée sur son bureau. A Nicolas, pour son soutien depuis mes premières heures à l'ENS, son humilité et sa gentillesse. A Arturo, Morgane, Susana, Lola et Margot pour avoir contribué aux expériences balbutiantes dont je doutais horriblement. A Mathieu pour sa maîtrise des gels et conseils culinaires. A Alessia, Selma, Marika, Gerard, Guillaume, Firas, Laurent, Jeff et Aurélien pour leur aide précieuse et sourires indéfectibles.

A Hadrien, Antoine, Rémi, Rafael, Raphael et Oscar pour m'avoir appris l'art de la polémique en dépit des conditions météorologiques ; pour prendre la chance au corps et en faire naître l'émerveillement. A Guillaume, pour les sensations, la décontraction et l'attirance des hauteurs. A Margot pour tout comprendre et maîtriser si bien le dressage de la pagure. A Bastien, Benjamin, Martin, Antonin, Christophe, Jonath, Louis, Guillaume, Clement et Clement pour les escapades débridées, l'exercice de la folie et de la lobotomie. A Dominika, Nil, Sophie, Louise et Odile pour ces discussions dont on ne se remet pas. A Alexis, Charlie, Jean, Antoine, Elise et Marion pour leur amour contagieux du grès, des essences de carbones bien sèches et du tendon bien tendu. A Marvin pour les coups de pouces.

A Papa, pour m'avoir tant répété que je n'avais probablement pas assez forcé. A toi encore, mais aussi Maman, Victoria et Pierre-Louis pour votre tolérance vraisemblablement unique dans l'univers et cohésion intra-atomique. Cette esquisse n'est que vous.

Ce travail n'aurait pas été possible sans les apports constructifs de Jeff Tweedy, Bill Callahan, Bob Dylan, Death Grips, John Talabot et Akenathon. Jean Giono, Francis-Scott Fitzgerald, John Fante, Fernando Pessoa, Alexandra David-Neel et Jean-Paul Sartre furent également impliqués. Chaim Soutine m'inspira quelques visions et Pierre-François Martin-Laval m'administra des anti-dépresseurs.

Enfin, aux esprits fougueux, aux pentes terrées, aux vents chaotiques, aux éboulis vivants et aux soleils effarants.

Abstract

In the vertebrate brain, mechanisms leading to the incorporation of newborn neurons into already functional networks still remain poorly understood. Indeed, since most of the studies have been performed at the single-cell level, a detailed description of the circuit dynamics is lacking.

To investigate this phenomenon, I have developed a pioneer methodology using the zebrafish larva as an experimental model and a multidisciplinary approach combining genetics, two-photon microscopy and optogenetics to monitor the developing activity of genetically targeted newborn neurons and the surrounding matured networks, in an intact and non-anesthetized vertebrate. Using this technique I have described for the first time, and in the time course of several days, the developmental dynamics of the functional properties of newborn neurons before and during their incorporation into the mature tectal circuit, the zebrafish most complex layered structure and highest visual center.

Overall, these results suggest a developmental sequence of events during which newborn neurons capable of generating intrinsic activity dynamics first connect to their pre-synaptic sensory organ (the retina). At a second stage, the newborn neurons gradually incorporate into the tectal mature circuit showing sparse correlations with mature neurons. At a third stage, the spatial organization of the correlation between the newborn and the mature neurons is refined, becoming denser. I thus suggest that the newborn neurons first connect to a large population of sparsely located mature neurons and subsequently distant connections are pruned, permitting the newborn-labeled neuron to acquire a stable and robust functional signature (e.g. sharp receptive fields).

In the recent years, treatments based on the transplantation of neural tissue have been developed to target neurodegenerative diseases such as Parkinson's disease. Because these therapies face the problem of poor survival and long-term functional incorporation, this study may provide better understanding of neuronal circuits formation and might pave the way to improve the efficiency of stem-cells-based treatments for human-brain reparation.

Table of contents

List of figures

List of tables

Nomenclature

Acronyms / Abbreviations

AF Arborization field

BC Bipolar Cell

bsPVIN Bi-stratified interneuron

ChR2 Channelrhodopsin2

Dpe Days post electroporation

Dpf Days post fertilization

DS Direction selectivity

FAP Fast amplifying progenitors

GC Ganglion cells

IPL Inner plexiform layer

MC Mitral cell

msPVIN Mono-stratified interneuron

NSC Neural stem cell

nsPVIN Non-stratified interneuron

OB Olfactory bulb

OPL Outer plexiform layer

OS Orientation selectivity

OT Optic tectum

PCNA Proliferating cell nuclear antigen

PG Peri-glomerular interneuron

PVN Peri-ventricular neurons

PVPN Superficial interneuron

PVZ Periventricular zone

RF Receptive fields

RGC Retinal ganglion cell

SAC Stratum album centrale

SAP Slow amplifying progenitors

SC Superior colliculus

SFGS Stratum fibrosum et griseum superficiale

SGC Stratum griseum centrale

SIN Superficial interneuron

SO Stratum opticum

SPIM selective-plane illumination microscopy

Chapter 1

Introduction

1.1 From neurogenesis to brain circuits

Neurogenesis is the process that forms functional neural circuits by the differentiation of neural stem cells (NSCs) into neurons, glia and oligodendrocytes. In vertebrates, neurogenesis was traditionally viewed as a process restricted to embryonic and perinatal stages but absent in adults (Chapouton et al., 2007; Lepousez et al., 2015; Ming and Song, 2011). However, seminal results obtained in rats (Altman and Das, 1965) and canaries (Paton and Nottebohm, 1984) have demonstrated that newborn neurons are constantly produced in the adult vertebrate brain. More recently, adult neurogenesis was shown in humans (Eriksson et al., 1998), suggesting a potential role for brain repair in the aging, damaged or diseased central nervous system (Rakic, 1988). However, clinical use of NSCs or their progeny has remained limited to a very small number of preclinical trials (Tabar and Studer, 2014). Indeed, a large number of technological (but also ethical) hurdles still need to be bridged to provide patients with cell-transplantation treatments that compete with existing therapies (pharmacological agents or deep brain stimulation).

To introduce the challenge of using NSCs for therapeutic applications, I will briefly describe brain development, from the division of NSCs up to their differentiation into neurons. Then, I will present how the discovery of vertebrate adult neurogenesis has changed our understanding of brain plasticity based on functional needs. Finally, I will discuss potential applications of neuronal progenitor cells for brain repair and highlight that injected cells integration is the current limiting factor for the success of this treatment. Although invertebrate neurogenesis represents a vivid field of research (for comprehensive review see Homem and Knoblich (2012)), I restrict here to vertebrates development and adult neurogenesis.

1.1.1 Neurogenesis: from neural stem cells to functional neurons

Neurogenesis starts during embryogenesis when the undifferentiated ectoderm, one of the three germ layers, gives rise to the epidermis and neuroectoderm: a process called "neural induction" (18 days post fertilization in humans and 10 hours post fertilization in zebrafish). The neuroectoderm undergoes a process called neurulation (see **Figure 1.1**) leading to the formation of the neural tube: a neuroepithelial structure containing NSCs. Neurulation occurs either by the invagination of the neural plate (primary neurulation) or by the formation of a solid cord from the mesoderm that sinks into the embryo (secondary neurulation) (Shimokita and Takahashi, 2011). Both processes lead to the formation of a neural tube. In fish neurulation is exclusively secondary while the two modes of construction co-occur in other vertebrates. In amphibians, such as Xenopus, most of the tadpole neural tube is made of primary neurulation, but the tail neural tube is derived from secondary neurulation (Gont et al., 1993). In mammals, secondary neurulation begins around somite 35 (Nievelstein et al., 1994).

The neural tube begins as a single layer of pseudo-stratified epithelial cells : NSCs that will eventually give rise to all the cell types in the adult nervous system. Rapid proliferation leads to the formation of four distinct growth regions: prosencephalon, mesencephalon, rhombencephalon and spinal chord. Neurons, glia and oligodendrocytes are added on this primary scaffold. Newborn neurons are formed from ventricular niches where dividing cells undergo a stereotyped pattern of cell movements as they progress through the mitotic cycle. Symmetric divisions maintain the pool of progenitors while asymmetric divisions generate neuroblasts that are fully committed to the neuronal lineage. Once the fate of a neurons is fixed, it migrates, develops an arbor of processes, intrinsic excitability, gains synaptic connectivity and transmitter specification (Spitzer, 2006). Eventually, neurons form functional circuits and show spontaneous activity that is later driven by sensory stimulation (Blankenship et al., 2009; Feldt et al., 2011). In humans, ∼250,000 neurons are produced each minute at the peak of prenatal neurogenesis to reach a total of ∼100 billions neurons at ∼20 years of age, when the corpus callosum stops growing (Pujol et al., 1993). Once the peak number of neurons is reached neurogenesis progressively recedes to restricted parts in mammals while in other vertebrates it is more widespread (for extensive review see Grandel and Brand (2013)).

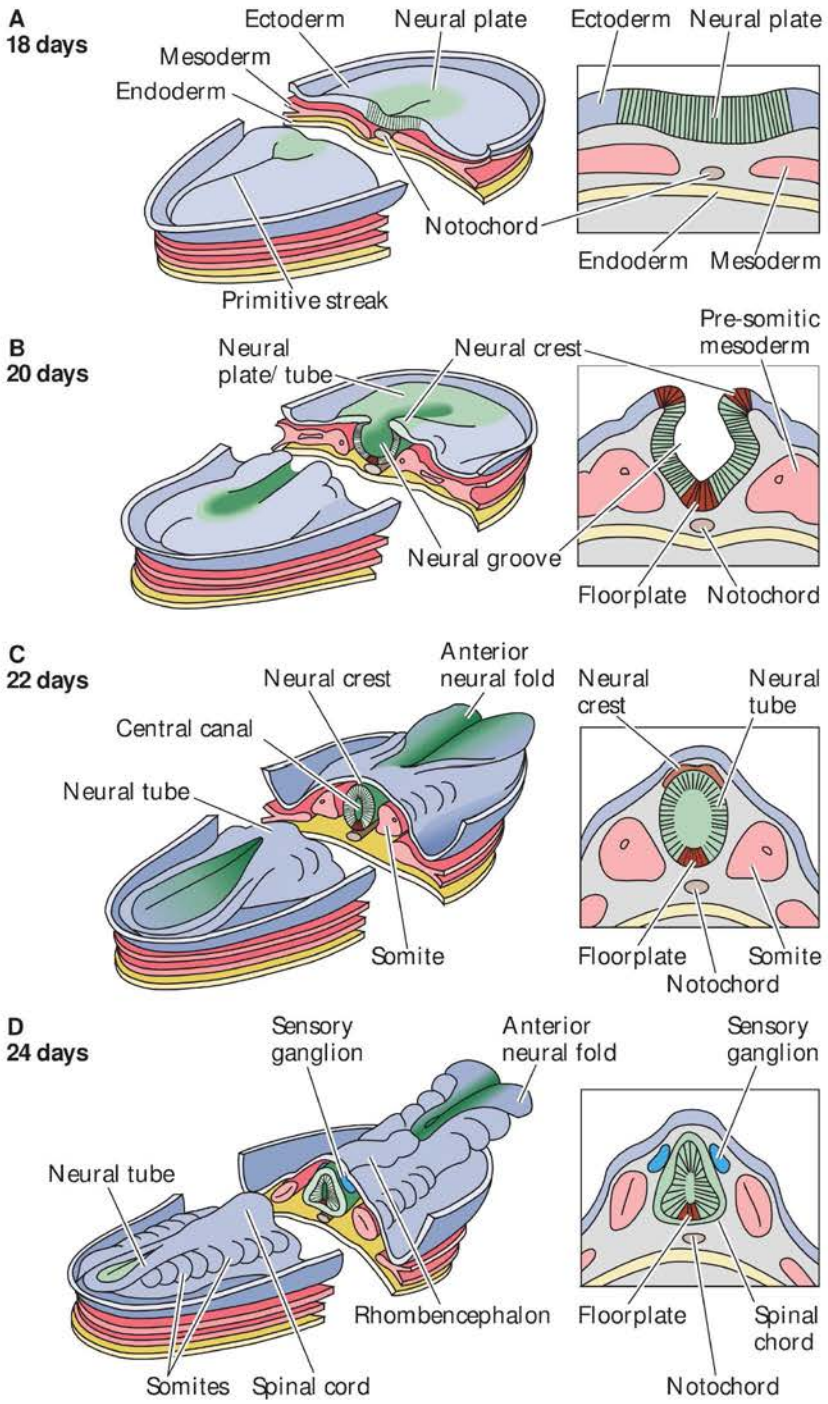

Fig. 1.1 **Neurulation in the human embryo**, legend next page

Fig. 1.1 (Previous page.) On the left: dorsal views of the embryo at progressive stages of early neural development; on the right a boxed view represents a cross section through the embryo at the same stage. **(A) 18 days post fertilization (dpf).** After gastrulation, the three embryonic layers are already established: endoderm, mesoderm and ectoderm. At the onset of neurulation, the notochord (that will later involute) forms from the mesoderm by invagination and marks a primitive streak on the ectoderm. The neural plate is a restricted ectoderm portion found over the notochord. **(B) 20 dpf.** 2 days later, the neural plate invaginates over the notochord, forming the neural groove that comprises neural crests its the dorso-lateral margins and the floor plate on its ventral pole neighboring the notochord. The neural crests will later differentiate into a diverse cell lineage: melanocytes, craniofacial cartilage and bones, smooth muscle, peripheral and enteric neurons, or glia. **(C) 22 dpf.** Once the invagination of the neural plate is completed, the neural tube forms a central canal that is located dorsally to the notochord. Below is the future epidermis and in between mesoderm-derived structures (somites) are found. They will later form musculature and skeleton. **(D) 24 dpf.** The anterior neural fold precursor becomes apparent, which will later form the telencephalon and the mesencephalon. More caudally, the rhombencephalon is already apparent and terminated by the rudimentary spinal chord. Adapted from Purves (2012).

1.1.2 Neurogenesis during development and adulthood

Adult neurogenesis is an ancient trait found in anamniotes (polyphyletic group comprising teleosts and amphibians). In teleosts, proliferation zones are distinctly localized in all subdivisions of the brain along the rostrocaudal axis. Between 12 and 16 distinct proliferation zones have been recognized in distantly related teleost species : stickleback (Gasterosteus aculeatus), brown ghost (Apteronotus leptorhynchus) and zebrafish (Danio rerio) (Grandel and Brand, 2013) (**Figure 1.2**).

In anamiotes, adult neurogenesis is thought to be the source of the regenerative capabilities of the CNS and the spinal chord. For example, regeneration can repair profound lesions such as incisions in the brain, removal of entire brain parts or transection of the spinal chord (Zupanc and Sîrbulescu, 2011).

This protracted general neuronal proliferation leads to continuous addition of neurons in sensory brain areas. Neurons are also added in downstream brain regions to process such increasing information (Grandel and Brand, 2013; Kaslin et al., 2008). Several studies have indeed demonstrated that the optic tectum (OT) and retina of amphibians as well as fish taste buds and chemosensory lobes grow in a correlated manner along the entire life of the animal (for extensive reviews see Grandel and Brand (2013); Kaslin et al. (2008)).

In mammals, adult neurogenesis has been shown to occur in several restricted brain regions: the dentate gyrus of the hippocampus (DG), the lateral ventricle (LV) and the striatum with varying turnover rates across species (**Figure 1.2**). For instance, the DG turnover greatly varies among species: from 10% in rodents up to complete replacement in humans (Spalding et al., 2013). In contrast, incorporation of newborn neurons in the OB is almost completely absent in humans (Bergmann et al., 2012). Moreover, the striatum receives newborn neurons from LV neurogenic niches in varying proportions depending on the species (Ernst and Frisén, 2015). Strikingly in humans neuroblasts are not limited to the LV walls but are also found deep within the striatum (Ernst et al., 2014). Although subject of a long debate cortical neurogenesis seems to be absent in human. Indeed, a recent study has shown that neurons in damaged cortical areas are as old as the individuals even after stroke (Huttner et al., 2014). However, the existence of chronic or injury-induced cortical neurogenesis in other mammals still remains controversial (Feliciano and Bordey, 2013).

Numerous functional implications have been attributed to adult neurogenesis. Over the recent years, pioneering studies have shown that neurogenesis is involved in recruiting local inhibition to increase pattern separation. Pattern separation is a property of neural networks which helps to discriminate between similar sensory stimuli. Data supporting this hypothesis comes from the work of Alonso and colleagues (Alonso et al., 2012) who observed that optogenetic stimulation of olfactory bulb (OB) newborn neurons enhanced mice olfactory discrimination capabilities when presented with a difficult odor-discrimination task. Adult neurogenesis has also been shown to participate in learning and memory but also in emotion and mood regulation (for comprehensive review see Lepousez et al. (2015)).

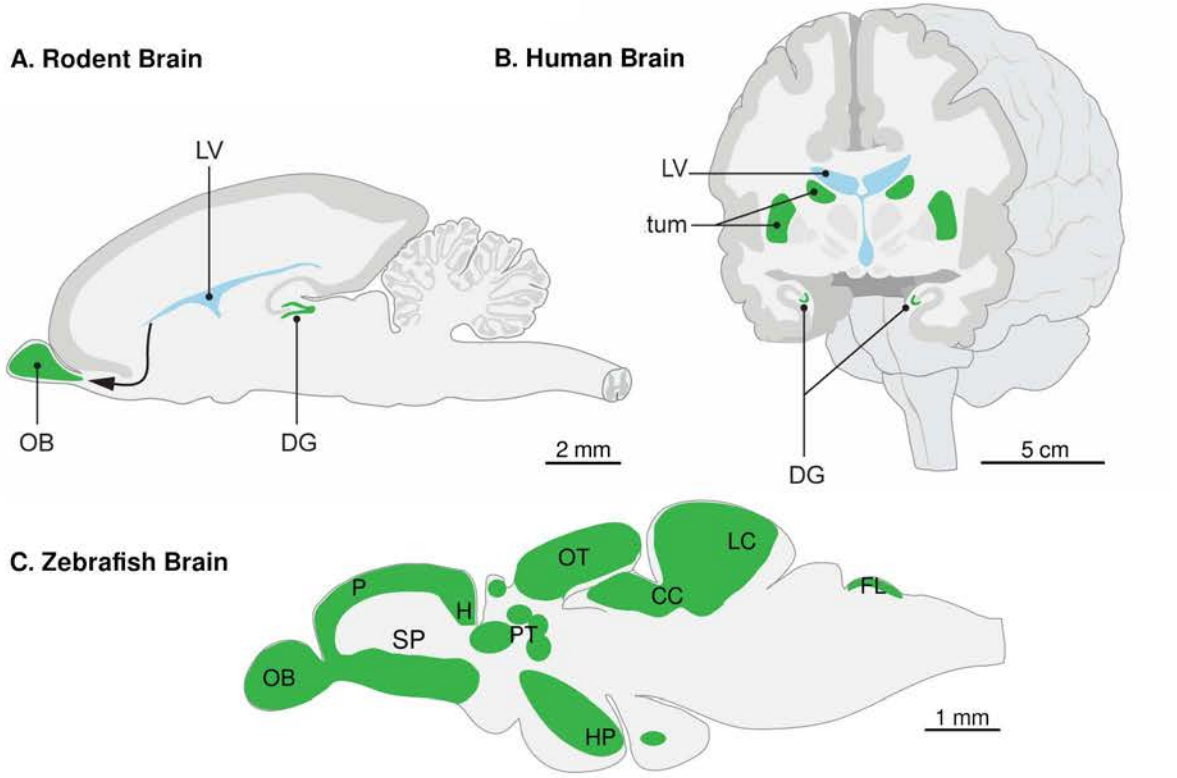

Fig. 1.2 **Schematic illustration of adult neurogenesis in the adult rodent, human and zebrafish brain. Neurogenic brain regions are indicated in green.** **(A)** Neuroblasts generated in the subventricular zone lining the lateral ventricle (LV) migrate to the olfactory bulb (OB), where they integrate as interneurons. **(B)** Neuroblasts are present in the subventricular zone also in humans, and new neurons integrate in the adjacent striatum, which plays an essential role in movement coordination, procedural learning, and memory, as well as motivational and emotional control. New neurons are also continuously generated in the DG of the hippocampus: a brain structure essential for memory generation, spatial navigation and mood control. **(C)** In fish, neuroblasts are present in all brain subdivisions. The main ones: OB olfactory bulb, P pallium , SP subpallium, H habenula, PT posterior tuberculum, OT optic tectum, HP hypothalamus, LC lobus caudalis, FL facial lobe, CC corpus cerebelli, Scale bars are located next to each brain. Adapted from Ernst and Frisén (2015) and Grandel and Brand (2013)

1.1.3 Potential clinical applications and technical challenges

Neural stem cells are a promising therapeutical approach for brain repair. However, generating precise subtypes of neurons and placing them in the proper location and ensuring subsequent network integration are difficult challenges. An important drawback of this approach is the inherent tumorigenicity of undifferentiated stem cells.

Diseases such as Parkinson's disease (PD) that affect a unique cell type (ie. Dopaminergic (DA) neurons) within a specific brain region (substantia nigra), could substantially benefit from these therapies. Indeed, drugs or deep-brain stimulation treatments targeting Parkinson's disease act upon symptoms but are inefficient at repairing or slowing down degeneration of the substantia nigra DA neurons innervating the striatum (Evans et al., 2012). The feasibility of DA neuron transplantation has been shown using human fetal tissue (Politis and Lindvall, 2012). However, despite long-term in-vivo dopamine neuron survival and dopamine secretion, the clinical benefit was modest and a subset of patients developed undesirable side effects such as dyskinesia (involuntary muscular movements Braak and Del Tredici (2008)).

Because of the large amount of cells required to restore neuronal deficits, recent studies have used grafts of stem-cell-derived DA neurons (Kirkeby et al., 2012; Yang et al., 2008) to restore large striatal deficits (injection of >100.000 DA neurons/ striatum). Although potentially useful, these grafts carry the risk of tumor formation and have been criticized for human applications. Indeed, injections of neural stem cells have been reported as a source of brain tumors in unregulated cell therapy (Amariglio et al., 2009). Also, grafts of post-mitotic neurons are limited by poor connectivity and survival (Kriks et al., 2011). They require large volume injections often leading to adverse effects such as inflammation and again to dyskynesia (Hagell and Cenci, 2005). Therefore, to develop optimized therapies using grafts of pure post-mitotic neurons it is necessary to generate cells that survive and connect efficiently to the pre-existing circuits.

However, the mechanisms by which neurons integrate into mature circuits in physiological conditions still remains poorly understood. To this end, it is important to shed light on the functional maturation of developing neurons up to their integration into mature networks. Understanding these basic principles will ***shine light on the basic mechanisms by which neuronal networks are formed during development and adulthood***, which may open new ways for developing safe high-yield cellular therapies. In the following part of this introduction I will focus on visual systems development as a model for studying neuronal circuit assembly. These studies might

improve progenitor-cells transplantation techniques to repair the diseased or lesioned brain.

1.2 Formation of visual systems

The visual system has long been used as a model to study the function and formation of neuronal circuits. Indeed, as highly visual animals, humans have an intuitive understanding of what the visual system does in contrast to other senses. Therefore, we can easily design stimulation paradigm to probe processing of visual information. Also, visual circuits have discrete starting points (photoreceptors) and are compact (unlike, for example, motor systems) and physically accessible (unlike, for example, the ear).

The formation of visual circuits is mainly guided by two factors: molecular cues and neuronal activity. I will first describe the describe the mechanisms underlying the establishment of retinotopic maps and synaptic lamination. In this section I restrict to studies that have tackled the development of retinotopically organized structures: the OT and the superior colliculus (SC). Second, I will detail recent results on the functional maturation of newborn neurons in the visual system, explaining the emergence of functional properties such as receptive fields (RF), and direction and orientation selectivity (DS and OS). Third, I will present recent studies on the assembly of local sensory circuits during development. To finish, I will highlight some technical hurdles to study the functional maturation and integration of newborn neurons into established circuits. Although I limit myself largely to fish and mice visual systems, I also support my general conclusions using data from other sensory systems, when a mechanism is much better understood elsewhere.

1.2.1 Molecular cues and patterning of visual systems

Long before molecular basis of receptors and ligands was discovered, John N. Langley (1892) proposed that "chemical relations" between neurons might underlie their connectivity. Roger Sperry's experiments on retinotectal projections provided a broad conceptual framework for this chemoaffinity (Sperry, 1963). Sperry predicted that genetically encoded labels exist in both retina and the OT, furthermore, if these labels are expressed in continuous gradients across both structures each retinal ganglion cell (RGC) axon and target would have a unique concentration of labels that could be matched until establishing a topographic organization (Sperry, 1963). Experimental

studies over the last two decades identified a plethora of molecular cues that guide their axons to their targets. Such factors indeed participate in the establishment of retinotopic maps and synaptic lamination. These two aspects of visual systems coarse patterning are developed below.

Retinotopic patterning

In order to interact with the external world, the brain first needs to generate a representation of the external sensory surrounding. In the vertebrate brain, visual space is relayed from the retina to the thalamus and SC in mammals and to the OT in anamniotes. These coarse retinotopic maps are established before the onset of vision, based on molecular cues, and later modified or refined by visual experience (Cang and Feldheim, 2013; Ruthazer and Cline, 2004). Here I detail how they interact using seminal work obtained in fish larvae, frog tadpoles and mice.

i. Mechanisms of chemoaffinity in the optic tectum and superior colliculus. The OT integrates and processes sensory inputs from different modalities to compute stimuli spatial localization and to generate adequate orienting motor behaviors. It's cardinal feature is its retinotopic organization: two neighboring tectal neurons receive visual inputs from two neighboring locations in the visual space. Studies have revealed that mapping of RGC axons along the posterior axis of the tadpole OT is controlled by matched gradients of EphA receptor kinases in the retina (temporal retina > nasal retina) and ephrin-A family of Eph ligands in particular ephrin-A2 and A5 in the tectum (caudal tectum > rostral tectum) (McLaughlin et al., 2003, Curr Op in Neurbiology). Activation of EphA by their ephrin ligands leads to axon repulsion (Flanagan and Vanderhaeghen, 1998) and inhibition of axon branching (Yates et al., 2001). Consequently, RGCs axons in the temporal retina, where EphA expression is high, cannot innervate the caudal tectum where ephrin-A levels are high (**Figure 1.3A**). Similarly, interactions between EphB and ephrin-B contribute to the dorso-ventral OT retinotopic mapping (**Figure 1.3B**).

Interestingly, Eph-ephrin (A and B) gradients also participate in building topographic maps in the mammalian superior colliculus (Cang and Feldheim, 2013). In mutants lacking several ephrins-As, SC functional maps are disrupted along the visual space nasotemporal axis. These maps are discontinuous and contain patches of SC that respond to similar but topographically incorrect spatial locations. These results demonstrate that coarse organization of SC and OT retinotopic maps is controlled by ephrins gradients (Cang et al., 2008).

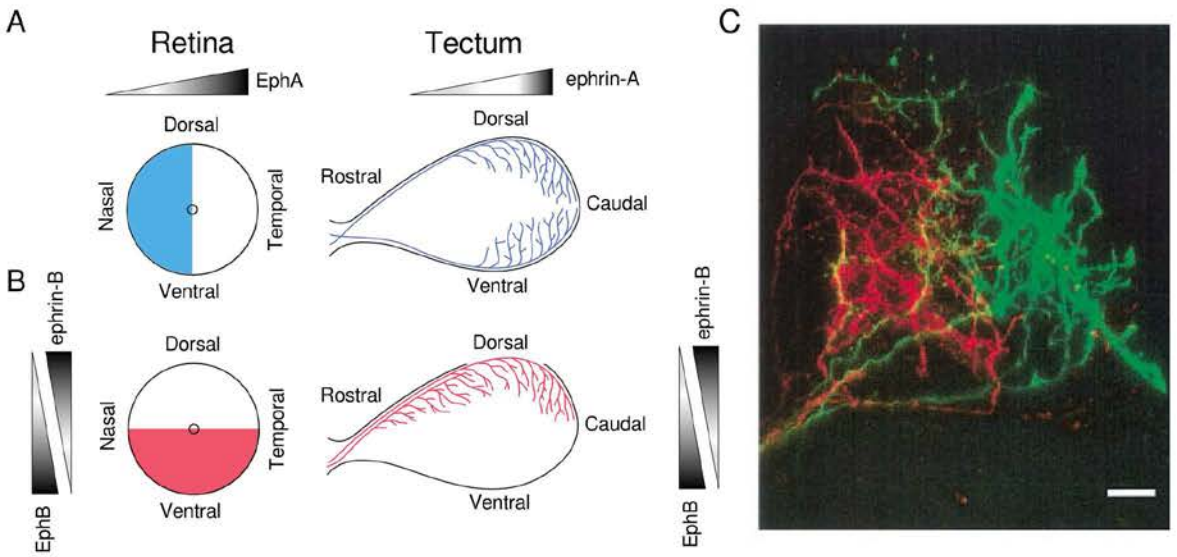

Fig. 1.3 **Sperry's demonstration of the retino-tectal topographic projections.** Regenerating retinal axons termination sites in the OT as observed in Sperry's original studies performed in goldfish Sperry (1963). Retinal halves were removed and the optic nerve of the same side severed. Fibers originating from the remaining retina regenerated and entered the OT. Regenerated fibers were unmyelinated and clearly distinguishable by silver staining after several weeks. **(A)** Ephrin-A and the EphA receptors act as chemoaffinity molecules for rostrocaudal mapping of the OT. Pattern of regeneration after removal of the temporal (right) retinal half. Note the newly formed axons originating from the nasal retina (blue) terminate in appropriate regions despite the availability of additional tectal tissue. **(B)** Ephrin-B and EphB act as chemoaffinity molecules rostrocaudal mapping in the OT. Pattern of regeneration after removal of the dorsal (top) retinal half. Note the newly formed axons originating from the ventral retina (red) which terminate in the appropriate regions despite the availability of additional tectal tissue. Graded distributions of ephrins and Eph receptors are indicated next to their appropriate structures. **(C)** Temporal and nasal retina of the Xenopus tadpole were labeled, respectively, with dil (red) and FITC-dextran (green) showing tectal inputs retinotopic organization. Orientation as in (A). Scale bar = 20 µm. Panels A. and B. are adapted from Sperry (1963). Panel C. is adapted from Ruthazer and Cline (2004).

ii. The role of neural activity in retinotopic patterning. Models for maps generation based on neuronal activity postulate that neurons with similar activity patterns are more likely to synapse on the same target cells thanks to Hebbian plasticity. Because topographic organization in the mammalian visual system is present before eye opening, its establishment has been postulated to rely on spontaneous activity patterns generated in the retina (retinal waves). Indeed, in mice, eyelids are closed during the

first postnatal week, and RGCs discharge highly correlated bursts of action potentials that propagate across the retina (Kirkby et al., 2013). The most compelling evidence for this idea comes from studies in mice that lack the $\beta 2$ subunit of the acetylcholine receptor (β2nAChR$^{-}/^{-}$). In these animals, correlated spontaneous activity had low amplitude, was brief and lacked well defined wavefront in comparison to controls (Burbridge et al., 2014). In such mutants, SC maps were more diffuse and SC neurons possessed enlarged RFs (Chandrasekaran et al., 2005; Mrsic-Flogel et al., 2005), while global retinotopic structure was still conserved.

Total disruption of ephrins gradients in the SC in $\beta 2$ KO animals completely disrupted global retinotopic organization of SC, and even abolished the discontinuous retinotopic patches (Cang et al., 2008). These observations suggest that molecular gradients and neuronal spontaneous activity interactions shape map formation in the SC.

In the zebrafish OT, the retinotopic map is generated by the projection of RGC axons to specific termination zones and restriction of their axonal arborization sizes. Indeed, excessive axonal arbor growth has been shown to perturb visually guided behavior (Smear et al., 2007). To decipher the role of activity in the formation of proper sized arborization fields, Ben Fredj et al. suppressed presynaptic neurotransmitter release in single RGCs using targeted expression of tetanus toxin light-chain fused to a green fluorescent protein (GFP) (Ben Fredj et al., 2010). Using time-lapse imaging of axonal growth in silenced neurons they observed a significant over-expansion of the territory occupied by the axonal arbor in the tectum. However, when neighboring RGCs were also silenced, single arbor area was restored to normal levels. This finding suggests that silent axons are capable of maintaining an appropriately sized territory when activity is even in RGCs population (silenced or active populations). Thus, the ability of axons to arrest growth and populate a specific brain region, is an activity dependent competitive process that participates in sculpting the precise tectal topography.

Establishment of dendritic lamination in the zebrafish optic tectum

i. Synaptic laminar-specific organization in the optic tectum. Synapses can cluster in planar laminae or spherical glomeruli. While the latter is typical of the organization of the vertebrate olfactory system, laminae are extensively found along the visual pathways, including the retina, tectum, thalamus and cortex. In these regions, laminae are stacked on top of each other. The combined output of all synaptic lamina generates a pattern of activity in the downstream neurons that is the neural substrate of a visual image. Lamination may reflect a strategy to generate synaptic specificity

avoiding interference by establishing parallel insulated channels (Kerschensteiner et al., 2009). Connectomic studies also suggest that lamination serves for wiring economy (Chen et al., 2006), when several cells converge on a single shared postsynaptic cell (**Figure 1.4**) (Baier, 2013).

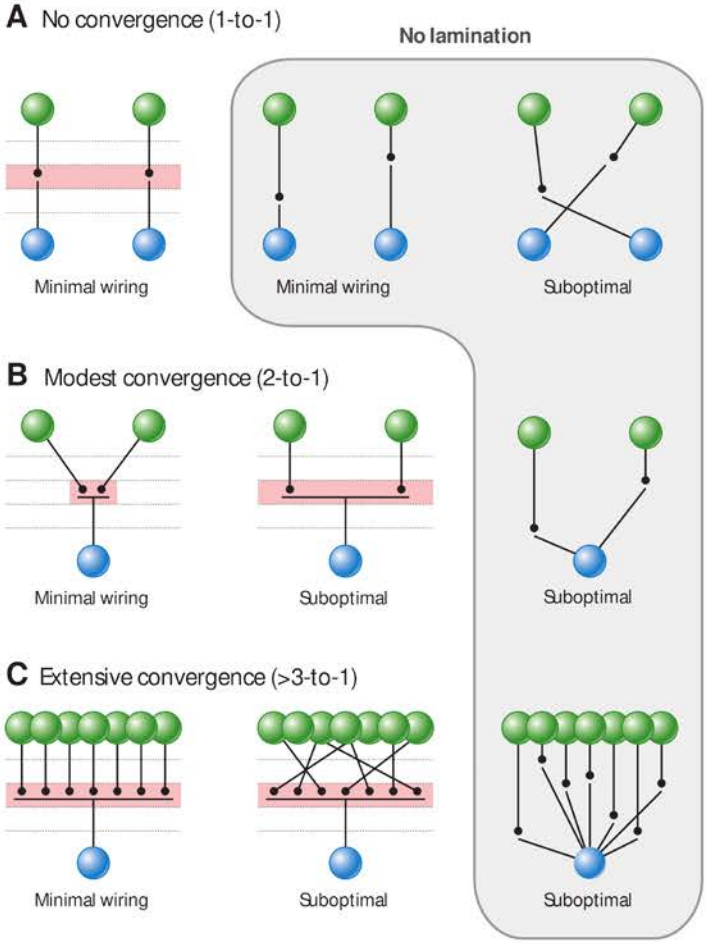

Fig. 1.4 **Wiring economy of converging inputs dictates the emergence of synaptic laminae.** Feature detectors such as RGCs receive and integrate inputs from several bipolar cells (BCs). **(A)** In a simple connectivity pattern without convergence (one-to-one connectivity between BCs and RGCs) non-straight connections are sub-optimal while straight connections provide an optimal wiring length, regardless of the placement of the synapses. Thus, the absence of convergence in the model will produce parallel, topographic wiring but not necessarily laminar architecture. **(B)** However, when low convergence (e.g., two-to-one or three-to-one) is required to extract relevant features of RGCs, wiring would result in a laminar organization although not all solutions provide identical wiring economy (compare left and middle). **(C)** When a large number of BCs converge on a single RGC (seven in this case), lamination with RGC axons projecting orthogonally towards BCs become the optimal synaptic arrangement (left). Extracted from Baier (2013).

In the zebrafish OT, molecular signaling and neuronal activity contribute to shaping synaptic lamination. Synaptic lamination in the retina and OT is depicted in **Figure 1.5**. The OT receives RGC inputs in the superficial stratum opticum lamina (SO), the stratum fibrosum et griseum superficiale (SFGS), the stratum griseum centrale (SGC), and a deep layer bordering the stratum album centrale (SAC) (**Figure 1.5**).

Other laminae receive inputs from non-visual sensory modalities and from tectal interneurons (Nevin et al., 2010; Robles et al., 2011; Scott and Baier, 2009). Retinal axons terminate exclusively in one of these four layers and are organized in arrangements that are specific to each lamina (Robles et al., 2011). Interestingly, functional imaging of visually evoked calcium responses in RGC axons indicates that axon composition of each laminae correlates with different functional properties (Gabriel et al., 2012; Nikolaou et al., 2012). This observation suggests that retinal afferents reaching the tectum are functionally and topographically organized.

ii. Several classes of molecular mechanisms control synaptic lamination. Axonal RGCs projections in the OT do not undergo developmental refinement across laminae and directly target one lamina (Robles et al., 2013). To generate such precise targeting, molecular players participate in the formation of adequate branching patterns, neurite guidance and local cell-cell recognition (for comprehensive review see Baier (2013))

Indeed, branching patterns have been demonstrated to rely on intrinsic, cell-autonomous programs. For example, introducing mutations into transcription factors such as topoisomerase 2B perturbs lamina targeting (Nevin et al., 2010) and more generally cultured neurons develop similar polarity and shapes as their counterparts in vivo (Dotti et al., 1988; Vierbuchen et al., 2010).

During the establishment of topographic sensory maps, neurite guidance relies extensively on gradients of attractive and repellent molecules. Among them, Slit1, a guidance factor produced by tectal cells that presumably forms a gradient reaching a maximum at the tectal surface. zebrafish has only one slit1 receptor, Robo2, which is is expressed in RGCs. Indeed, disruption of Robo2 function in astray mutants dramatically perturbs axonal lamination (Xiao et al., 2011).

Interestingly, work in the chick retina has shown that transmembrane adhesion molecules of the immunoglobulin-domain-containing superfamily (IgSF) are expressed in largely non-overlapping cells and can bind in an homophilic manner (Yamagata et al., 2002). Because the perturbation of the expression levels of IgSF resulted in

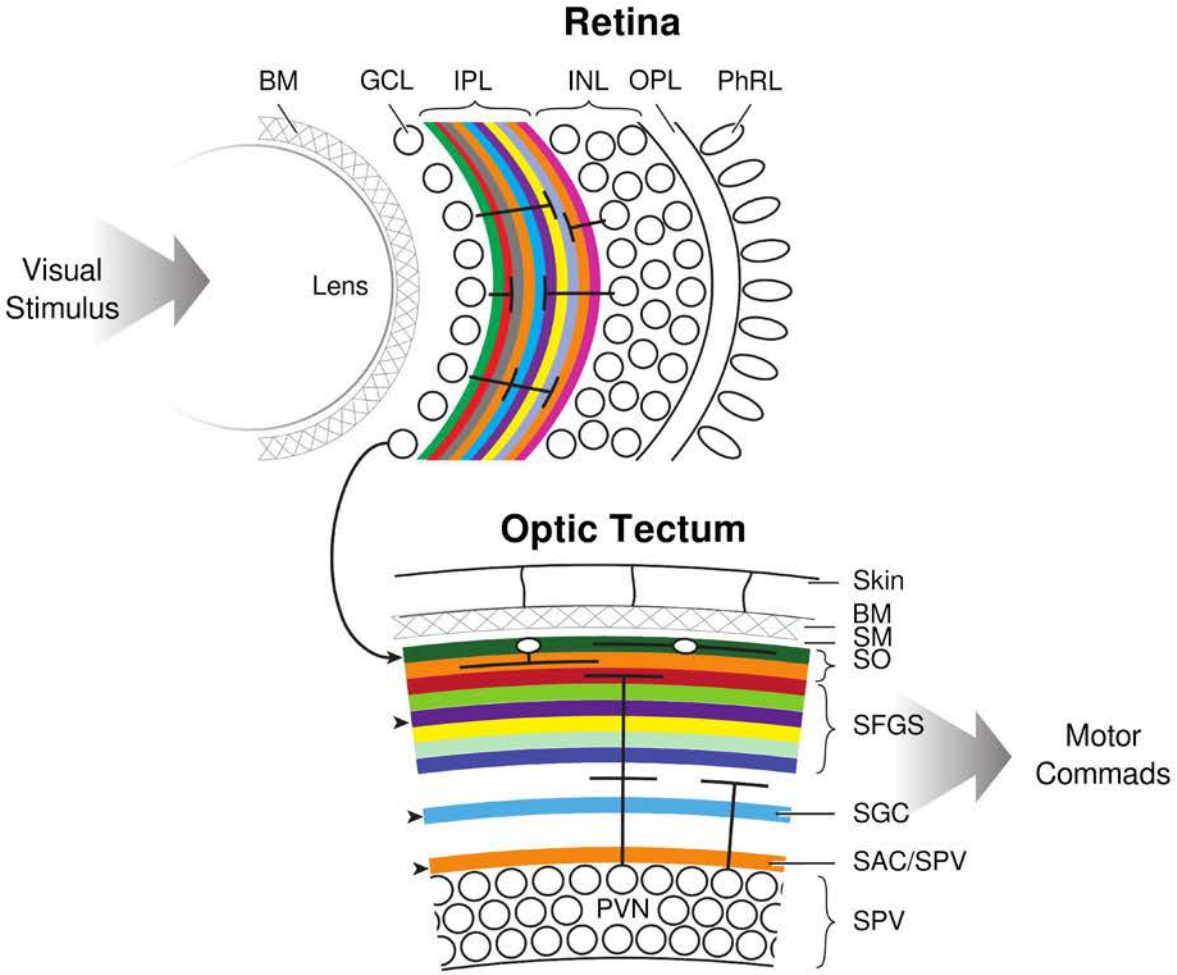

Fig. 1.5 **Synaptic lamination is a fundamental feature of the zebrafish OT circuitry.** From top-left to bottom-right: photons reflected by the visual scene enter the eye though the lens and are first converted into electrical signals by photoreceptors that form the deepest cellular layer in the vertebrate retina. Interneurons, including BCs receive this signal in a neuropil layer called the outer plexiform layer (OPL). Their cell bodies are located in the inner nuclear layer (INL). BCs project in the inner plexiform layer (IPL) where they contact both axons and dendrites of amacrine cells (ACs) and dendrites of RGCs in ∼10 layers. RGC axons leave the eye and form the optic nerve to project to several arborization fields including the OT. Arrows indicate retino-recipient areas. It contains periventricular neurons (PVNs) residing in the deep layer that extend dendrites to a laminated neuropil. RGCs innervate layers indicated by arrows. BM: basement membrane, GCL: ganglion cell layer, PhRL: photoreceptor layer, SAC: stratum album centrale, SAC/SPV: boundary between SAC and SPV, SFGS: stratum fibrosum et griseum superficiale, SGC: stratum griseum centrale, SM: stratum marginale, SO: stratum opticum, SPV: stratum periventriculare. Adapted from Baier (2013).

sublaminar mistargeting, these cell-to-cell recognition factors might play an essential role in organizing laminar sensory structures.

Contrary to zebrafish, layer-specific targeting in the rodent SC is partially subject to developmental refinement. Indeed, several RGC subtype axons project broadly before retracting to a single laminae while others directly target their final laminae (Chen and Nedivi, 2010).

iii. Accurate synaptic lamination of RGCs is independent of neuronal activity. In various models, laminar organization is strikingly resilient to perturbations of normal neural activity. For example, raising zebrafish in complete darkness or blocking synaptic transmission with botulin toxin B did not perturb laminar organization of the OT (Nevin et al., 2008). Moreover, β2nAChR$^{-}/^{-}$ mouse (showing altered retinal waves) showed normal RGCs lamination in downstream SC and lateral geniculate nuclus (LGC) (Huberman et al., 2008b).

To conclude, laminar organization in vertebrates arises independently of coordinated activity and fully relies on molecular players to define branching patterns, laminar targeting and sublaminar cell-to-cell recognition. However, the formation of retinotopic maps requires both molecular and activity dependent mechanisms to generate precise topography (Cang and Feldheim, 2013; Ruthazer and Cline, 2004). Interestingly anamniotes' OT is devoid of wave-like activity but groups of tectal neurons are spontaneously active (Demas et al., 2012; Imaizumi et al., 2013; Romano et al., 2015) and sensory transduction to the OT is present from the early larval development (Niell and Smith, 2005). In what extent these neuronal events contribute to refine the OT retinotopic map remains unexplored. This could be experimentally tested by abolishing structured activity or by generating unnatural activity patterns by optogenetics.

1.2.2 Emergence and maturation of neuronal functional properties

Once coarse patterning of retino-recipient areas is achieved, neurons undergo profound functional and morphological changes. Indeed, patterned activity (such as retinal waves) and sensory experience refine neuronal functional properties. To support this claim I will discuss three examples of the emergence and maturation of sensory induced neuronal responses in the OT, in mammalian V1 layer 2/3 neurons and in the mammalian olfactory bulb during adult neurogenesis.

Development of orientation and direction selectivity

i. Opposing mechanisms shape the development of orientation and direction selectivity in mammals. In the mouse visual system, first neuronal activity is observed early as P3 (post-natal day 3) in the superior colliculus and V1 and triggered by retinal waves (Ackman et al., 2012). However, the first visually induced responses appear at P10-12 before eye opening (through the eye-lids or after manually opening them). At these stage, strong light flashes induce responses in more that 80% of neurons (Rochefort et al., 2011).

A key feature of V1 Layers 2/3 is the presence of neurons that respond to a preferred orientation (Ohki et al., 2005). Among the OS cortical neurons, some are also DS: responding to a preferred direction more than any other (**Figure 1.6b**, neuron 1). The developmental sequence of DS and OS properties has recently been studied in the mouse and the ferret (for examples of DS and OS neurons, see **Figure 1.6b**).

In mice, drifting gratings trigger responses after eye opening or one day later with near half of the responses being OS (OSI>0.5). Interestingly, 93% of OS neurons were also DS (OSI>0.5 and DSI>0.5, Rochefort et al. (2011)). At this stage neurons displayed preference for the anterior direction along the anterior-posterior axis as well as a preference for the dorsal direction along the ventral-dorsal axis. This asymmetric distribution disappeared within 3 days and was maintained up to adulthood in dark or normally reared animals. Therefore, the developmental changes observed in mice V1 neurons are independent of visual experience and probably rely on robust intrinsic programs (genetically encoded precise wiring or spontaneous intrinsic activity).

Conversely, ferrets V1 neurons display OS responses but DS emerges 2 weeks after (White and Fitzpatrick, 2007). Strikingly, dark rearing prevents the formation of DS maps in ferrets, although adult mice and ferrets possess identical number of DS neurons in V1. This indicates a crucial role of visual experience for the emergence of DS in ferrets (Li et al., 2006). To conclude, two independent mechanisms seem to shape DS in the mammalian cortex: in carnivores, it requires visual experience while in rodents it is independent of it.

Such divergence in the maturation of DS can be explained by the RGCs properties. Indeed, RGCs are already DS in mice at eye opening and this feature is probably relayed to the visual cortex (Rochefort et al., 2011). In other species such as ferrets, cats and monkeys, this property first emerges in V1 (Huberman et al., 2008a) and might underlie different ecological needs soon after birth or be related to their opposing cortical organization: columnar vs. salt and pepper (Ohki et al., 2005).

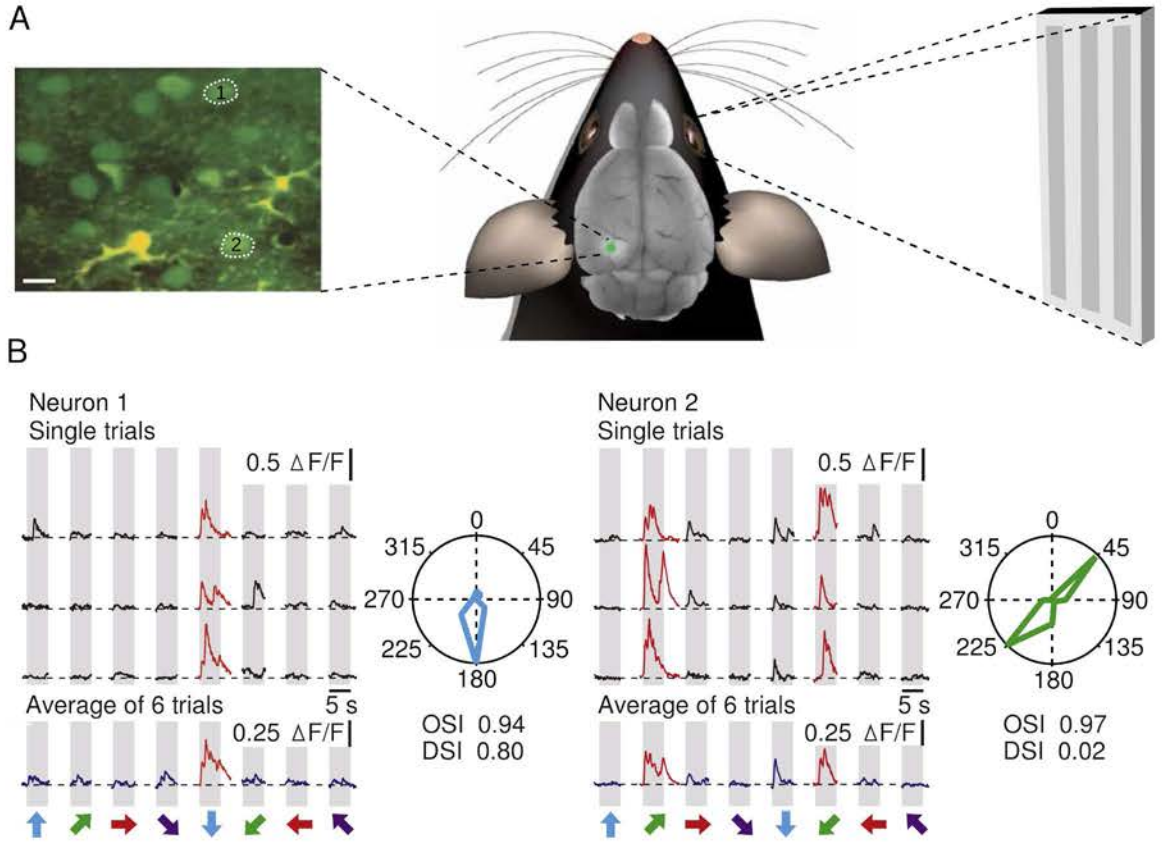

Fig. 1.6 **Recording of neuronal properties in the mouse visual cortex. (A)** Experimental set-up for in-vivo two-photon calcium imaging of visually evoked neuronal activity. Brain tissue is first exposed after craniotomy over the region of interest. The left panel shows an imaged plane in cortical layer 2/3 of the primary visual cortex (V1). Neuronal activity is estimated using a fluorescent calcium indicator as a proxy. Here the dye Oregon Green BAPTA-1 (green) has been used in combination with the glial marker sulforhodamine 101 (yellow) to detect neurons unambiguously. On the right panel, the visual stimulation (moving sinusoidal gratings) is shown to the contralateral eye. To provide stable imaging, the animal is anesthetized. **(B)** Two examples of neuronal recordings obtained in this region. Single and average calcium transients evoked by visual stimulation (left), with polar plots showing the neuron's response function to oriented drifting gratings (right). Gray regions indicate periods of visual stimulation. The arrows represent the direction of the stimulus. Three single trials are represented with black lines and the average of six trials is shown in blue. Neuron 1 is highly DS and OS: it responds selectively to a horizontal drifting grating moving in the upward direction (red calcium transients). Neuron 2 is highly OS but weakly DS. OSI, orientation-selectivity index; DSI, direction-selectivity index. Scale bars = 10 mm. Composed from Grienberger et al. (2012) and Rochefort et al. (2011).

So far, no satisfying theory has been able to explain rodent versus carnivores and primates functional organization and development divergence. Assessment of the population coding efficiency during development and up to adulthood in these two cortical architectures might reveal adaptations for their respective visual environments. This hypothesis could be tested by studying the cortical organization of carnivore rodents (killer mouse or Onychomys leucogaster).

ii. Emergence of direction selectivity in anamniotes tectal neurons. In the zebrafish larva, retinal axons begin to populate the tectal neuropil at 60 hours post fertilization (hpf) (**Figure 1.7**) and the first visual responses emerge at 66 hpf in tectal neurons (Niell and Smith, 2005). At this stage, visual responses were not spatially tuned. First DS responses were observed at 72 hpf, and by 78 hpf (just 12 h after the first visually evoked responses could be recorded), the proportion of DS cells was similar to that of mature 9 days post fertilization (dpf) neurons.

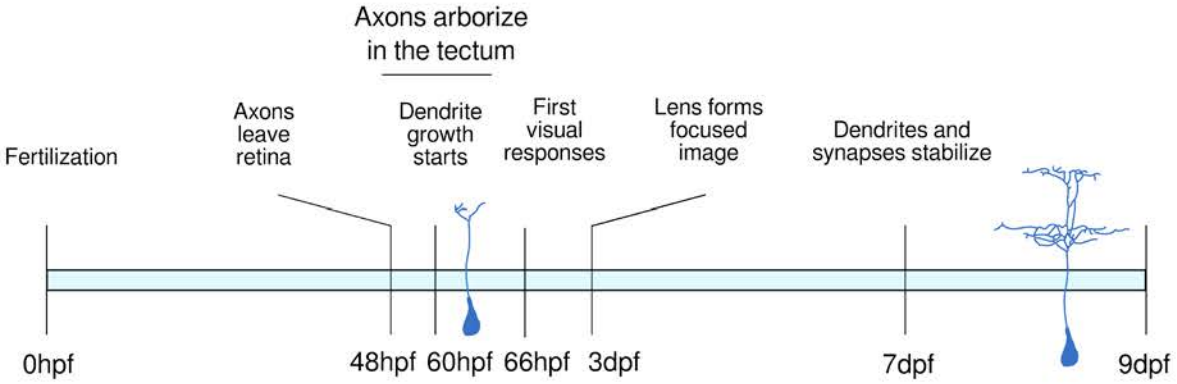

Fig. 1.7 **Timeline of the morphological development of zebrafish tectal neurons.** At 48 hpf, RGCs axons leave the retina and start to innervate the OT at 60 hpf. The first visual responses in tectal neurons were observed at 66 hpf although the lens development is not yet completed. At 3 dpf, the lens forms a focused image on the retina and tectal neuronal morphology maturates. At 7 dpf, tectal neurons ares still plastic (Niell et al., 2004) but their dendritic arbors have reached their final sizes and mature cell types are observed.

At 78 hpf, tectal neurons are still morphologically immature (**Figure 1.9**) and the number of synapses they receive are ~10 times smaller than their mature counterparts at 7 dpf (Niell et al., 2004). The authors suggest that the first synapses are already specific and that the addition of new synapses probably represent highly dynamic functional or immature contacts that do not perturb the overall neuronal function (Niell and Smith, 2005). These transient contacts might be stabilized through Hebbian activity-dependent plasticity (Munz et al., 2014), and probably serve other functions

than DS. Indeed, the net increase of synaptic contacts might contribute to decreasing response variance as observed in ferrets (Smith et al., 2015) or for increasing visual acuity necessary for prey capture (Gahtan et al., 2005).

Interestingly, larvae raised in the dark showed similar distribution of DS index in the recorded neurons indicating that the emergence of this feature is independent of visual experience. However, in the tadpole OT DS could be rapidly modified by presenting a series of repetitive moving bars (Engert et al., 2002, Nature) suggesting basic inter-species differences of neuronal functional development. However, Neill et al., have suggested that this activity-induced plasticity might be required for the maintenance of functional responses but not for their initial establishment in zebrafish (Niell and Smith, 2005).

Refinement of the tectal neurons receptive fields

i. Emergence of receptive fields in tectal neurons. A distinctive property of mature tectal neurons is the matching of their excitatory and inhibitory RFs (Tao and Poo, 2005). Since inhibitory inputs were delayed relatively to excitatory ones (∼3,94ms in tadpole tectal neurons), this delay has been suggested to arise from local feed-forward inhibition (**Figure 1.8**) (Akerman and Cline, 2006; Tao and Poo, 2005; Zhang et al., 2011). The delayed inhibition probably serves to enhance the temporal fidelity of visually induced responses which is in accordance with results obtained in hippocampal pyramidal cells (Pouille and Scanziani, 2001).

To decipher the mechanisms shaping the nascent RFs Zhang et al., performed voltage-clamp recordings in zebrafish tectal cells from 4 to 8 dpf while mapping the excitatory and inhibitory RF (eRFs and iRFs) (Zhang et al., 2011). eRFs and iRFs were recorded at 70 and 0mV: reversal potentials of glutamatergic and GABA/glycinergic synaptic currents, respectively. The authors observed a development of the RFs according two main stages: first, eRFs expanded from 4 to 6 dpf followed by a refinement at 8/9 dpf. Interestingly, the eRF size at 8–9 dpf was not significantly different from that at 4 dpf, which is consistent with previous observations Niell and Smith (2005). Conversely, iRFs were initially broad and diffuse and later and refined to match the eRFs at 8/9 dpf.

To test the contribution of intratectal excitatory inputs in the eRFs, the inhibitory inputs were blocked by applying muscimol (a GABAa receptor agonist) whose diffusion was calibrated not to affect retinal inputs. Zhang et al., observed that this manipulation spared ∼70% of the magnitude of the visually induced responses, but more importantly it drove only modest changes in RF sizes. This demonstrates that changes in RFs size

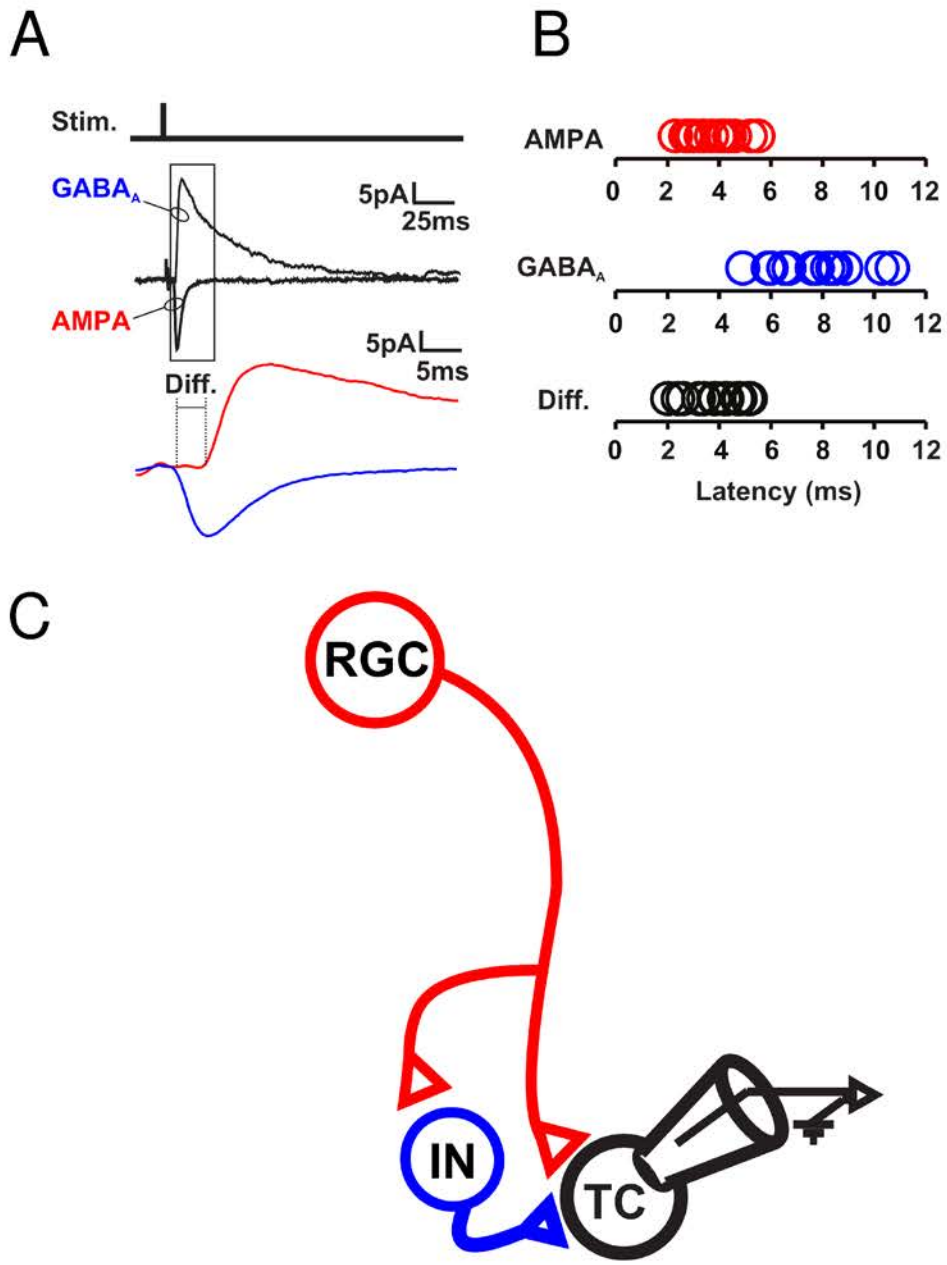

Fig. 1.8 **Retinal activity drives a feedforward GABAergic circuit in the tadpole optic tectum.** **(A)** Super imposed current traces of : GABAa and AMPA synaptic currents. A single stimulus to the optic chiasm evoked a monosynaptic AMPA response (Holding potential of -70 mV) that was followed by a delayed GABAa response (Holding potential of 0 mV) in the same tectal neuron. GABAa synaptic currents evoked by retinal afferent electrical stimulation were delayed with respect to AMPA currents. **(B)** The latency from stimulation of both GABAa and AMPA synaptic currents are summarized for several recordings. GABAa responses are delayed compared to AMPA responses. **(C)** Proposed disynaptic feedforward GABAergic circuit along the retino-tectal pathway. Retinal afferents (RGC) synapse directly to tectal cells (TC) and to GABAergic interneurons (IN) providing feedforward GABAergic input to TC cells. Adapted from Akerman and Cline (2006).

throughout development could be mainly explained by the modulation of direct retinal inputs and not by a reorganization of intratectal feedback loops.

ii. Receptive fields and dendritic arborization. In various sensory systems a correlation exists between RF size refinement and axonal pruning during development. It has been shown to occur in the retinal projection to the rodent SC (McLaughlin et al., 2003) and in the chick tectum (Nakamura and O'Leary, 1989). However, this process seems to be absent in the fish and the tadpole RGCs (Meyer and Smith, 2006; Sakaguchi and Murphey, 1985). In fish tectal neurons, a monotonic increase is observed of the total arbor length from 3 to 7 dpf followed by a stabilization period. Therefore, there is no correlation between dendritic arbor size and RF size during zebrafish tectal cells development. Synaptic reorganization, independently of tectal morphology is probably the main driver for the maturation of the visual responses during early development.

In accordance with results obtained on the DS, visual deprivation only drove minor changes in the RFs size (Niell and Smith, 2005), indicating that early functional development mainly relies on intrinsic hard-wired programs rather than on sensory experience. However, such observation doesn't exclude that sensory deprivation can be compensated by homeostatic plasticity. Homeostatic synaptic plasticity is a type of plasticity in which synaptic strength is adjusted throughout a neuron to compensate for changes in neural activity. Typically, homeostatic plasticity occurs by either increasing or decreasing synaptic strength to optimize the neuron's dynamic range (Deeg and Aizenman, 2011; Turrigiano, 2012). Additionally, neurons can compete for RGCs inputs in an activity-dependent manner shaping in return the extent of their RFs. Therefore, subtle single-neuron modification of their intrinsic functional properties have to be modified to address the role of activity during development.

iii. Neuronal intrinsic activity instructs receptive fields development. In a recent study, Dong and Aizenman explored to what extent activity of developing tectal neurons could shape their RFs during development (Dong and Aizenman, 2012). More precisely, they asked whether neural activity has an instructive or permissive role. Indeed, it is not clear whether activity patterns shape neuronal properties (instructive) or whether the presence of activity suffices to trigger other developmental mechanisms (permissive), such as molecular factors that sculpt appropriate neuronal connections and morphology (Ruthazer and Aizenman, 2010).

To get insights into the role of activity (instructive or permissive) in a developing neuronal system, it is necessary to change the structure of the neural activity in single neurons while keeping the global network activity at constant levels. This can be achieved by altering the spiking probability for low currents while maintaining the spiking probability identical at high currents. To this end, Dong et al., expressed a Shaker-like Xenopus Kv1.1 potassium channel in sparsely labeled tadpole tectal neurons. This tool impairs the intrinsic excitability of developing neurons while sparing their maximal spike output. Kv1.1 expressing neurons retained immature characteristics: larger RF, reduced sharpness and importantly displayed persistent recurrent excitation compared to controls (Dong and Aizenman, 2012). This suggests that functional development of tectal neurons depends on structured spontaneous activity, a process that cannot be revealed using manipulation of activity levels of the entire visual system (using dark rearing as in Niell and Smith (2005). However, spontaneous activity frequency and amplitude as well as dendritic arbor total length were spared.

Overall, these results indicate that intrinsic activity has an instructive role to refine the neuronal visual RF, probably participating in pruning local recurrent inputs. However, other neuronal features (such as morphology) probably do not need patterned activity to normally develop. A summary of the tectal neurons morphological and functional refinement during early development is illustrated in **figure 1.9**.

Olfactory newborn neurons maturation during adult neurogenesis

The previously described studies focused on neuronal maturation after eye opening in mammals or during early larval stages in anamniotes. The mechanisms described orchestrate global circuit maturation in a relative synchronous manner after a massive production of newborn neurons. Conversely, in the rodent olfactory bulb (OB) ∼1% (∼80.000 neurons) of the total resident granule cells (GC) incorporates in already mature circuits every day (Kaplan et al., 1985). Therefore, the OB is an invaluable system to decipher how functional maturation and integration occur without perturbing already established networks, and to understand how sensory experience influences the incorporation process.

i. Olfactory bulb circuits. The OB relays information from olfactory receptor neurons (ORNs) of the olfactory epithelium located at the roof of the nasal cavities (**Figure 1.10A**). ORNs project to the superficial layer of the OB that contains ∼2000 spherical neuropil structures called glomeruli where they contact mitral cells (MCs) and tufted cells (TCs) subsequently innervating the piriform cortex (Zou et al., 2009)

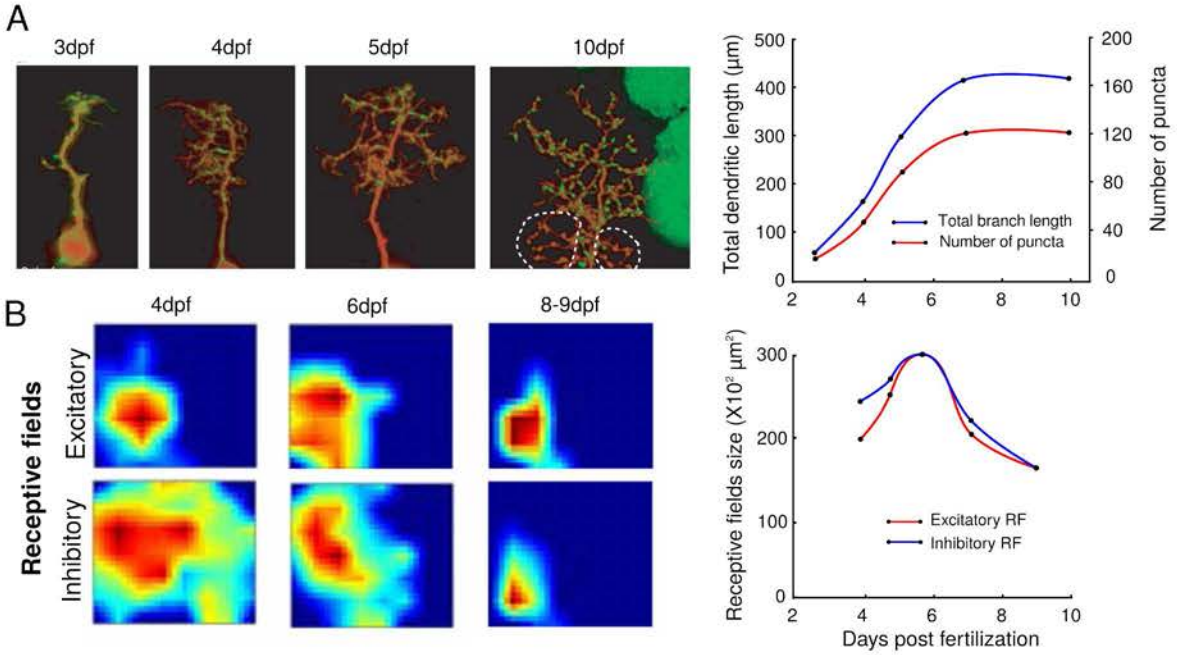

Fig. 1.9 **Morphological and receptive fields maturation of the larva's tectal neurons.** **(A)** Morphological maturation of tectal neurons from 3 to 10 dpf. Left panels: pictures of one developing neuron at 3, 4, 5 and 10 dpf labeled with DsRed to monitor morphological changes and PSD-95:GFP to monitor post-synaptic densities (punctae). Note that both the dendritic total length and the number of puncta increase from 2 to 7 dpf and then stabilize. Scale bar: 10 µm. Remark that PSD-95:GFP labeling is excluded from the proximal dendritic arborization (dotted line). Auto-fluorescence of the skin is visible in the upper-right corner of 10 dpf. Right panel: Quantification of total branch length and number of puncta at the different developmental stages. Adapted from Niell et al. (2004). **(B)** Maturation of inhibitory and excitatory RFs (iRFs and eRFs, respectively) of tectal neurons recorded using whole- cell patch clamp while presenting visual stimulation tiling the visual space. Left panels: examples of iRFs and eRFs at these 4, 6 and 8-9 dpf. Right panel: inhibitory and excitatory RFs sizes development from 4 to 8-9 dpf. iRFs initially cover larger portions of the visual spaces than eRFs. Note that iRFs and eRFs sizes increase from 4 to 6 dpf and then recede up to 8-9 dpf to match in sizes. Adapted from Zhang et al. (2011).

(**Figure 1.10B-C**). An important property of the OB is the over-representation of inhibitory interneurons compared to excitatory output neurons (MCs and TCs): ∼100:1 Nissant and Pallotto (2011). Periglomerular interneurons (PGs) extend neurites into multiple glomeruli contacting both MC and TC apical dendrites and express either GABA or dopamine. GCs are GABAergic synapse on MCs in a peculiar dendro-dendritic fashion (Petreanu and Alvarez-Buylla, 2002) (**Figure 1.10D**). They comprise ∼75% of the sub-ventricular zone (SVZ) newborn neurons generated during adulthood Menini (2009). Here I briefly summarize current knowledge about the mechanisms by which adult-born GCs progressively gain excitability, form synaptic outputs and reach maturity.

ii. Synaptic integration and maturation of functional connectivity. Maturation of GCs is typically studied by injecting replication defective GFP expressing viruses into the cerebral ventricle/SVZ (Carleton et al., 2003; Petreanu and Alvarez-Buylla, 2002) or directly in the RMS (Bardy et al., 2010; Livneh et al., 2014; Panzanelli et al., 2009). The process of morphological maturation lasts ∼2-4 weeks (Petreanu and Alvarez-Buylla, 2002) during which five morphological stages can be observed after SVZ injection: tangentially migrating neuroblasts within the rostral migratory stream (RMS) (Stage 1, days 2-7), radially migrating immature neurons (Stage 2, days 7-9) in the GC layer, GCs with dendrites that do not reach the mitral cell layer (MCL) (Stage 3, days 9-13), GCs with dendrites in the external plexiform layer (EPL) devoid of spines (Stage 4, days 11-22) and finally, mature GCs with spines (Stage 5, days 15-30) (**Figure 1.11A**).

Before entering the OB circuitry (stage 1), neuroblasts are already sensitive to GABA released by the neuroblasts themselves and glutamate released by the astrocytes surrounding the RMS in a non synaptic manner (Platel et al., 2007) (Figure 1.11B). These neurotransmitters control proliferation of precursors, migration and survival of neuroblasts: GABA reduces SVZ proliferation Liu et al. (2005) and decreases neuroblasts migration speed (Platel et al., 2008) and promotes survival (Platel et al., 2010).

When reaching the OB, stage 2 immature neurons (∼3 days post RMS injection, dpi) already receive GABAergic and glutamatergic synaptic inputs (Panzanelli et al., 2009) but the first occurrence of action potentials is observed at stage 4 (∼11-22 dpi) (Bardy et al., 2010; Carleton et al., 2003) (**Figure 1.11B**). To test whether such nascent spikes could suppress the activity of neighboring MCs, Brady et al., injected a Channelrhodopsin2 (Chr2) expressing construct into the RMS. By optically

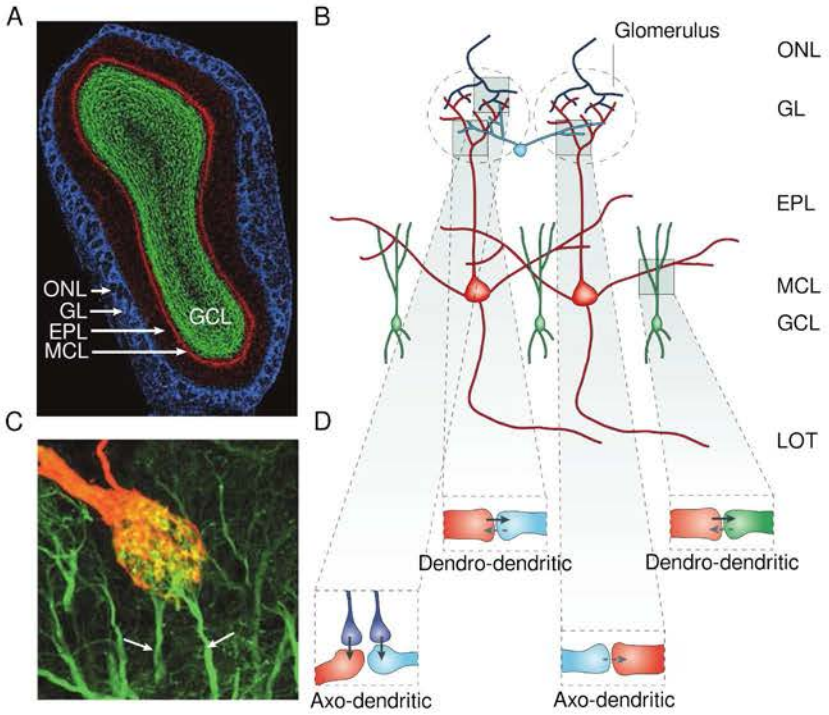

Fig. 1.10 **Neuroanatomy of the olfactory bulb and micro-circuits in the olfactory glomerulus. (A)** Cross section of the mouse olfactory bulb (OB) showing concentric cellular and neuropil layers. The outermost layer is the olfactory nerve layer (ONL) that receives axons from the olfactory epithelium located in the roof of the nasal cavities (blue). These axons enter the glomeruli in the glomerular layer (GL, in blue) and synapse with MCs and PGs. The cell bodies of mitral cells are found in the thin mitral cell layer (MCL) lining the granule cell layer (GCL) which contains migrating immature interneurons (shown in green). Between the GL and the MCL lies the external plexiform layer (EPL), where extensive interactions occur between the apical dendrites of GCs and the lateral dendrites of MCs. **(B)** A confocal image of a mouse glomerulus. OSN axons are shown in orange and MCs and TCs are shown in green. Arrows point to the apical dendrites of mitral or tufted cells. **(C)** Glomeruli coarse organization. OSN axons (dark blue) contact both MCs and PGs. Each MC innervates only a single glomerulus with its apical dendrites and also extends lateral dendrites around the OB that synapse extensively with a population of interneurons known as GC, shown in green. Finally, the axons of MCs, form the lateral olfactory tract (LOT) and project to the piriform cortex (or primary olfactory cortex) which is the presumed site of higher olfactory processing. Note that TCs and glial cells are not represented. **(D)** The glomerular neuropil contains three forms of synaptic contacts: axodendritic synapses that connect the axons of OSNs to the dendrites of MCs and PGs; reciprocal dendrodentritic synapses between the dendrites of MCs and the dendrites of PGs, providing a second source of input to PGs; and inhibitory axodendritic synapses connecting axons of PGs to the dendrites of mitral cells, which mediate either feedback or feedforward inhibition. In addition, in the external plexiform layer, reciprocal dendrodendritic synapses are observed between MCs dendrites and GCs dendrites. The extensive interactions of these synapses are thought to be crucial for controlling the output of MCs. Reproduced from Zou et al. (2009).

stimulating newborns GCs and recording MCs they observed the emergence of light-induced post-synaptic inhibitory currents beginning at 13 dpi. However, the proportion of GCs connected to MCs increased sharply from 4 to 6 weeks post injection suggesting that their integration into the resident circuitry occurs long after they acquire the ability to spike (Bardy et al., 2010). Such a delay between synaptic input and output establishment has been suggested to participate in the competitive survival of newborn neurons (Lepousez and Lledo, 2013; Nissant and Pallotto, 2011).

To conclude, OB adult born neurons first receive synaptic inputs (∼3dpi) and then gradually form synaptic outputs (∼2-6 wpi). This process is markedly different from what can be observed during OB embryogenesis where spiking activity if first acquire before GABA, NMDA and AMPA conductances emerge Lledo et al. (2004). In contrast, adult hippocampal neurogenesis seems to recapitulate embryonic development (Espósito et al., 2005).

iii. Activity dependent control of neuron survival and synaptic integration. Approximately 50% of adult OB newborn neurons do not survive more than a few weeks after maturation (Petreanu and Alvarez-Buylla, 2002) probably due to activity dependent processes. Indeed, sensory deprivation using naris occlusion decreases their survival (Petreanu and Alvarez-Buylla, 2002) while sensory enrichment increases it (Rochefort et al., 2002). Activity is also required for GCs to form inhibitory outputs towards MCs (Kelsch et al., 2009). Other experiments have also highlighted the existence of critical periods when neuronal activity effects on survival, and circuit integration are maximal. For example, Mouret et al., have shown that the survival of newborn neurons of 18-30 days was increased when that animal was exposed to an olfactory based discrimination learning paradigm (Mouret et al., 2008).

iv. Maturation of sensory responses of peri-glomerular cells Although the previous studies began to decipher how newborn neurons incorporate into the adult OB, the maturation of their sensory responses has only been studied recently. By exposing adult mouse to seven different monomolecular odors, Livneh et al. recorded the developing functional responses of PGs from 2 to 8-9 wpi (Livneh et al., 2014). They observed that the number of odors that a newborn PGs responded to was maximal at 4 wpi and later receded to match the adult population.

To test whether these changes could be explained by morphological maturation, they quantified their dendritic length and found no correlation between sensory sensitivity and morphological features. However, when quantifying the activity of neighboring

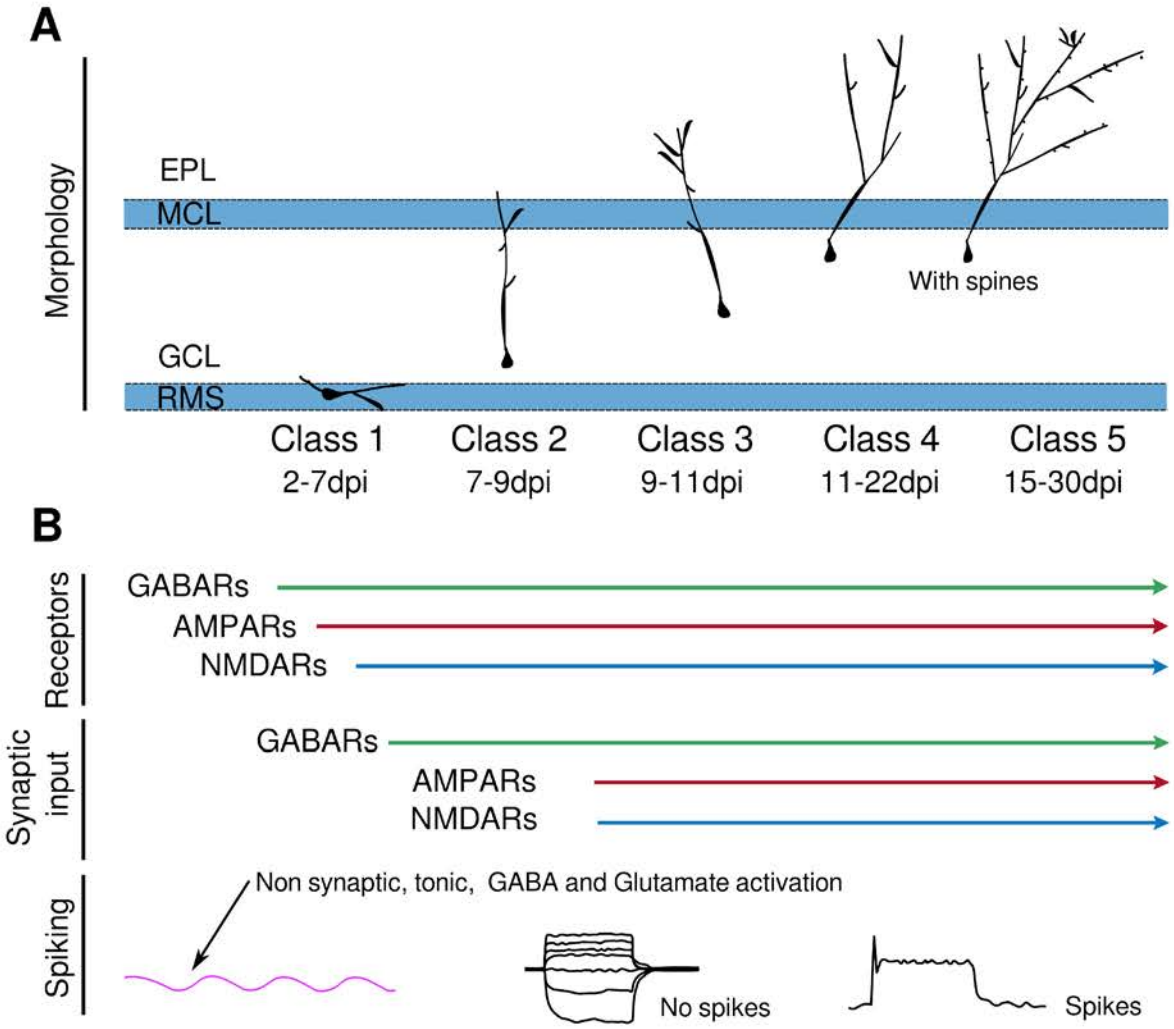

Fig. 1.11 **Morphological and functional development of adult-born olfactory bulb granule neurons.** **(A)** Morphological development time course. Classes and corresponding approximate days post viral injection are indicated below as in Petreanu and Alvarez-Buylla (2002). **(B)** Functional maturation time course. Receptor expression precedes synaptic activation: in the RMS newborn neurons express GABA and Glutamate receptors and respond to both neurotransmitters tonically in a non-synaptic fashion. Newborn neurons show atypical maturation, generating only sodium-based action potentials after they have begun to receive synaptic input. Note that functional maturation continues after the represented stages. Adapted from Petreanu and Alvarez-Buylla (2002) and Lledo et al. (2006).

glomeruli by performing intrinsic signal imaging (measurement of activity-correlated changes in oxygen saturation) they observed that 4 wpi neurons were, on average, correlated with more glomerular activity "hot-spots" than 8-9 wpi and adult neurons. These results suggest that the detected increased sensory sensitivity might arise from a transient pattern of synaptic connectivity. Interestingly, sensory enrichment during the period of high responsiveness critically modified the sensory selectivity of 8-9 wpi neurons in comparison with their counterparts from naive mice. These results demonstrate that adult-born neurons can become functionally distinct from their resident counterparts if exposed to new odors during a developmental critical period lasting from 2-5 wpi.

To conclude, these results suggest that neuronal fate is not predetermined but can be strongly modified by modulation of sensory inputs during limited periods of their development. Such plasticity probably provides flexibility to the OB, enabling to adapt to sensory changes in the environment by generating cells that are specifically tuned towards new sensory cues.

1.2.3 Development of visual system microcircuits

Processing in cortical areas operates in a cooperative circuit manner where the activity of individual neurons is less relevant. Indeed, it is population activity that matters to select appropriate interpretations from cortical inputs (Douglas and Martin, 2004). For example, control of the eyes (Lee et al., 1988) and arm position (Georgopoulos et al., 1986) are predicted with higher accuracy when studying neural populations than single neurons.

In the vertebrate brain, sensory processing occurs in microcircuits in which synaptic connectivity is highly structured (Song et al., 2005). In some species, including primates and carnivores, cortical neurons with similar response properties and shared connectivity are grouped together into radial columns, forming organized maps of stimulus features. In rodents, cortical neurons with different orientation preferences are inter-mingled in a "salt-and-pepper" fashion (Ohki et al., 2005). Nevertheless, rodents exhibit fine-scale specificity in the organization of synaptic connections (Yoshimura and Callaway, 2005; Yoshimura et al., 2005) and preferential connectivity among neurons with similar orientation tuning (Bock et al., 2011; Ko et al., 2011).

Until recently the developmental mechanisms of such microcircuits have remained elusive due to the lack of tools to study neuronal sensory responses and interrogate their synaptic connectivity. Several outstanding studies have started to answer these question in the mammalian visual cortex that is both amenable to functional two-

photon imaging and electrophysiological recordings. Two-photon imaging typically enables to probe neuronal sensory response in vivo while multi-units electrophysiology enables assessing of direct synaptic connectivity. Here, I will summarize studies that have addressed the question of local circuits formation.

Ontogenetic columns are functional columns.

The radial-unit hypothesis was first proposed by Rakic (Rakic, 1988) who suggested that "ontogenetic columns" formed by clonally related neurons migrating along a unique radial-glia fiber provided the basis of canonical circuits and general brain architecture. Viral labeling of radial glia progeny firmly proved this hypothesis (Noctor et al., 2001) and opened the way to the interrogation of functional similarity within ontogenetic columns. Recently, three studies have provided insights on how sister cells arising from identical radial glia progenitors develop preferential connectivity and share similar functions.

i. Preferential connectivity among sister cells. Clonally related excitatory neurons ("sister cells") belonging to ontogenetic radial columns can be labeled by in-utero intraventricular injection of enhanced green fluorescent protein (EGFP) expressing retrovirus, around the onset of neurogenesis. By performing multiple-electrode whole-cell recordings (Yu et al., 2012) showed that labeled cells preferentially acquire electrical coupling through gap junctions with each other rather than with adjacent non-sister excitatory neurons during early postnatal stages. This preferential coupling allowed selective electrical communication between clonally related excitatory neurons, promoting the generation of action potentials and synchronous firing.

Interestingly, electrical synapses formed by gap junctions provide the first form of communication between yet to be synaptically connected newborn neurons. In mammals, gap junctions coupling declines from P1–P2 and is nearly absent by P6 (Yu et al., 2012), with preferential chemical synaptic connectivity emerging at P10–P17. Surprisingly, blocking electrical communication impairs the subsequent formation of specific chemical synapses between sister excitatory cells in ontogenetic columns (Yu et al., 2012). These results suggest a strong link between lineage-dependent transient electrical coupling and the assembly of precise excitatory neuronal microcircuits in the neocortex.

ii. Functional similarity and divergence of sister cells. To ask whether such preferential connectivity was correlated with similar function. Li et al. used the same

retrovirus based technique combined with two-photon imaging to probe the orientation preference of clonally related neurons. They demonstrated that sister cell pairs are more likely to have similar orientation preferences than non-sister ones, and that this similarity depends on the presence of functional gap-junction communication during the first postnatal week (Li et al., 2012b).

In this study the authors focused on cells separated by ∼120 μm shortly after eye opening (P12-P17). However later on, radial glia progeny eventually dwell over larger cortical volumes (tangential diameter 300–500 μm) spanning to layers 2–6 in older animals (P49-P62) (Ohtsuki et al., 2012). Using a transgenic mouse expressing Cre in a low number of progenitor cells Ohtsuki et al., labeled the entire clonal unit of neocortical progenitors and recorded their functional properties in layers 2-4. Although they reproduced the results of Li et al., they observed diversity within the clonally related population of neurons, with nearly half of all neuron pairs showing differences in orientation preference greater than 30° and a quarter exhibiting differences greater than 60°.

The authors suggest that clonal identity cannot be the only factor determining the response selectivity of neurons, and other mechanisms, such as activity-dependent processes may influence this original scaffold and determine the final selectivity of cortical neurons in adult animals. Taken together, these results provide compelling support for cell lineage as a significant factor in determining the priming of connection specificity that underlies functionally defined cortical circuits in rodents.

Interestingly, functional similarity of clonally related neurons was also observed in the tadpole OT (Muldal et al., 2014). In this study, the authors performed dye electroporation to label individual tectal progenitors in the proliferative zone. Labeling was only transmitted to daughter cells enabling to record their RF and compare it to non clonally related neurons. Clonally related neurons had significantly more similar Rf centers than non-clonally related neurons indicating that neuronal lineage influences the topography of the retinotectal map. Taken together, the results suggest that ontological mechanisms that shape neuronal microcircuits are evolutionary conserved in vertebrates.

Features selectivity and recurrent connectivity

Although the previous results highlight the role of electrical synapses as scaffold for the proper establishment of neuronal connectivity, they did not shed light on how their functional properties develop together with an appropriate set of synaptic connections. Here I describe one outstanding study that has provided great insight into the emergence

of functional microcircuits in the visual cortex (Ko et al., 2013). To probe neuronal functional properties together with their synaptic connectivity the authors performed in-vivo two-photon calcium imaging followed by in-vitro multi unit recordings of the same neurons.

Surprisingly, L2/3 pyramidal cells in the mouse visual cortex were already highly feature selective at eye opening. However, neurons with similar responses (high signal correlations) were not yet preferentially connected. Later, local connectivity reorganized extensively: more connections formed selectively between neurons with similar visual features and eliminated between visually unresponsive neurons while the overall connectivity did not change. Interestingly, these results suggest that neurons rely on their functional similarity to form preferential connections providing the basis for microcircuits assembly.

The same group further asked whether visual experience was required to shape these microcircuits. They showed that dark rearing was not required for the preferential coupling of similarly tuned neurons. However, it prevented the elimination of connections between neurons that did not respond to visual stimuli, after eye opening. Overall, these results suggest that wiring of similarly tuned neurons relies on spontaneous activity, but elimination of excessive connections requires visual experience (Ko et al., 2014).

Noise correlation and sensory discrimination

Noise correlation has traditionally been attributed to common inputs or direct connectivity between pairs of neurons (Moore et al., 1970; Shadlen and Newsome, 1998). Indeed, a recent study has found significant correlations between the NC of pairs of neurons and the probability of synaptic connectivity between them (Ko et al., 2011) .

In numerous mammals, spontaneous cortical waves are observed in the retina and propagate to the superior colliculus and cortex (Ackman et al., 2012; Wong, 1999). Using two-photon calcium imaging of the ferret's visual cortex at eye opening, Gordon et al, noticed that induced activity could also trigger wave-like responses. During such events, neuronal responses displayed strong pair-wise noise correlation, large variability and poor OS. Interestingly, they observed that wave-like responses were only transient disappearing at $\sim$2 weeks and then replaced by sparse responses Smith et al. (2015). Simultaneously, OS increased and noise correlation and variability decreased.

By deriving a discriminability index of motion direction they observed that variance and noise correlation had a strong effect in population coding performance of neural ensembles. Indeed, reduction of variance and noise correlation dramatically increased

discriminability in developing neurons and during training with moving gratings. These results indicate that changes in response variance and noise correlations reflect cortical maturation in ferrets. The authors suggest that this might occur together with an increase of preferential connectivity among neurons responding to similar stimuli (Ko et al., 2013) and the development of cortical inhibition (Le Magueresse and Monyer, 2013).

Since wave-like activity in the immature cortex has also been observed in various mammals, including monkey and ferret (Wong, 1999), independent of their cortical functional organization (columnar or salt and pepper) this work probably emphasizes an evolutionarily conserved mechanism that serves the refinement of neuronal networks to promote better sensory direction discrimination.

Development of neuronal functional properties: Key questions and technical challenges

A fundamental topic in neuroscience is to understand how neurons acquire their functional properties. In particular how intrinsic or extrinsic processes regulate such development during embryogenesis and adulthood, remains unclear. Indeed, does receptive fields or DS are acquired mainly through genetic programs during development or can neuronal functional properties be modulated by already matured neurons through a functional "dialogue" between them?

To answer these question it is necessary to monitor the properties of newborn neurons along development while presenting sensory stimuli. However, studying the developing brain in an intact behaving animal (vertebrate, or invertebrate) represents an important technological challenge (Albright et al., 2000). In mammals, where a significant part of the development occurs in utero, having access to the full developmental sequence of neurons without perturbing the physiology, is not yet feasible. Current in in vivo studies, require surgery and extensive use of paralyzers and anesthetics (Livneh et al., 2014), therefore most of the studies use brain slices preparation where it is impossible to perform sensory stimulations (Carleton et al., 2003; Ge et al., 2006; Song et al., 2012). Also such studies overlook whole-circuit effects and putative fate selection based on already functional neurons (to avoid redundancy for example).

Newly developed tools such as long-term cranial windows might enable to bridge that gap in juvenile animals (Holtmaat et al., 2009). However, implementing these tools in developing mammals still seems impossible due to cranial growth and extensive cerebral morphogenesis. Therefore the essential principles that guide the functional maturation and circuit assembly during vertebrate neurogenesis either embryonic or in

the adult, remain largely unknown. Interestingly, the embryonic brain of anamniotes and in particular zebrafish is highly amenable to both circuit and single-cell studies using genetically encoded optical indicators (GECI) of neuronal activity and single-cell labeling (Ben Fredj et al., 2010; Romano et al., 2015). Moreover, these recordings can be performed without the use of paralyzers or anesthetics just by embedding the animal in a drop of agarose. Due to a continuous growth of the brain during the fish's lifespan (Kaslin et al., 2008; Recher et al., 2013) it is possible to study mature circuits and newborn neurons development in parallel. Therefore, I believe that the zebrafish offers unique properties to study neuronal circuit's assembly.

1.3 The zebrafish model

1.3.1 Zebrafish as a vertebrate model for systems neurosciences

The zebrafish (Danio rerio) is a small gregarious teleost fish originating from eastern Asia (**Figure 1.12A-C**). It belongs to the Cyprinidae family: stomachless fish with toothless jaws. Adults grow up to ∼4 cm and become sexually mature at ∼3 months. They are commonly found in shoals of a dozen of individuals and are omnivorous. They thrive in various environments: shallow waters with low current but also rice fields, streams or ponds. They are found in remote and pristine waters but also in contact with men in canals or rice paddies (**Figure 1.12D-F**). They consume plankton, insects, small crustaceans but also algae, plant material and assorted detritus. They are exposed to a large array of predators: birds such as kingfishers or herons, insects (dragonfly larvae) and many species of fish, at different stages of their development (**Figure 1.12G-O**). Interestingly, most of the behavioral repertoire of zebrafish has been observed in laboratory conditions and field observations are anecdotal (Parichy, 2015).

Zebrafish was first selected as a genetic model ∼35 years ago by George Streisinger and colleagues (Streisinger et al., 1981). It's genome has been completely sequenced and comparison with the human genome has revealed that 70% of human genes have at least one obvious zebrafish ortholog (Howe et al., 2013) . Numerous models for human diseases have been generated over the past years including melanoma (White et al., 2011), Alzheimer's disease (Paquet et al., 2009) and Rett syndrome (Pietri et al., 2013).

In recent years, the zebrafish larva has become an appealing vertebrate model for neuroscience research. Indeed, zebrafish are easy to breed and transparent at embryonic

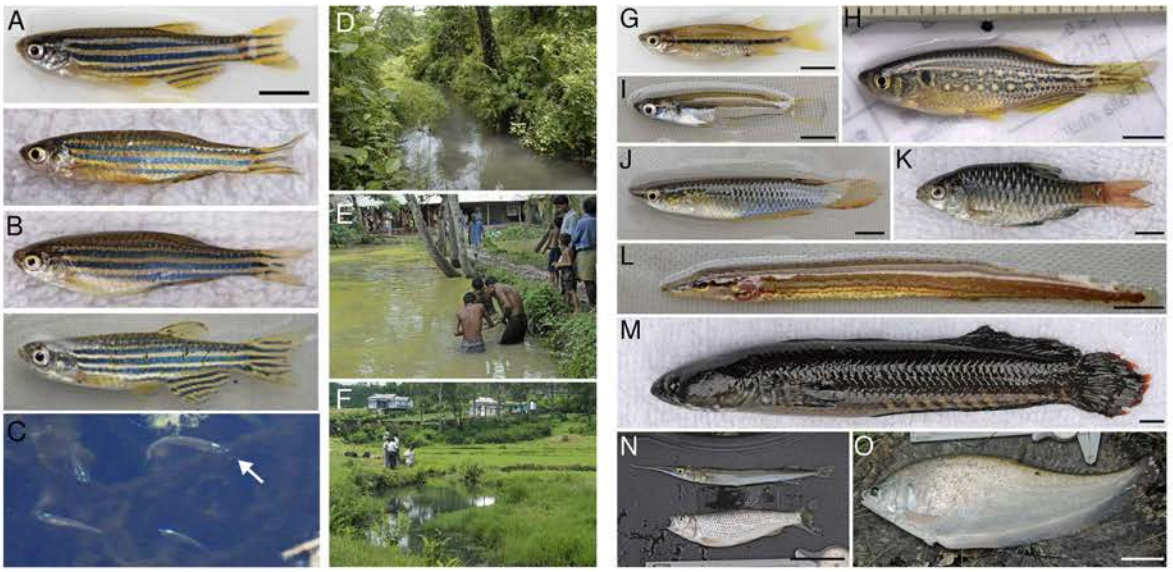

Fig. 1.12 **Zebrafish ecology. (A-B)** Several adult zebrafish from northeastern India. The upper two fish are males and the lower two fish are females. Scale bar: 5 mm **(C)** Shoaling zebrafish (a single fish is highlighted with the arrow) in a stream-side pool in Meghalaya, India, north of Bangladesh. **(D-F)** Zebrafish habitat is diverse: pristine stream **(D)**, man made canals **(E)** and rice paddies **(F)**. **(G-K)** Examples of zebrafish competitors E. danricus **(G)**, D. dangila (juvenile; **H**), Oryzias (I), Aplocheilus panchax **(J)**, and P. shalynius (K). **(L–O)** Potential predators are Mastecembalus **(L)**, Channa **(M)**, Xenentodon (top) and Barilius **(N)**, and Notopterus **(O)**. Scale bars: 5 mm **(G–M)**; 5 cm **(N, O)**. All pictures reproduced from Parichy (2015).

and larval stages. At 6 dpf the vitellus lipids are exhausted and the larva needs to catch prey and avoid predators. This strong evolutionary pressure leads to a rapid development of functional sensory systems in general, and vision in particular, and a large repertoire of motor behaviors (Friedrich et al., 2010; Portugues and Engert, 2009). At this stage the brain is ~500 mm thick and ~3 mm long, making virtually all brain and spinal-cord neurons accessible to functional imaging using two-photon microscopy (**Figure 1.13A-B**). Its rapid external development makes the zebrafish an ideal preparation to understand how genetic and activity dependent programs shape the development of sensory motor circuits.

Additionally, the zebrafish larva is ideal for the implementation of optogenetic tools to monitor and manipulate neuronal activity and behavior (Douglass et al., 2008; Schoonheim et al., 2010), which in combination with optical techniques such as two photon microscopy, selective-plane illumination microscopy (SPIM) (Ahrens and Engert, 2015) and holographic stimulation enables the study of neural circuit dynamics and motor behavior with single-cell resolution (Zhu et al., 2012). All these

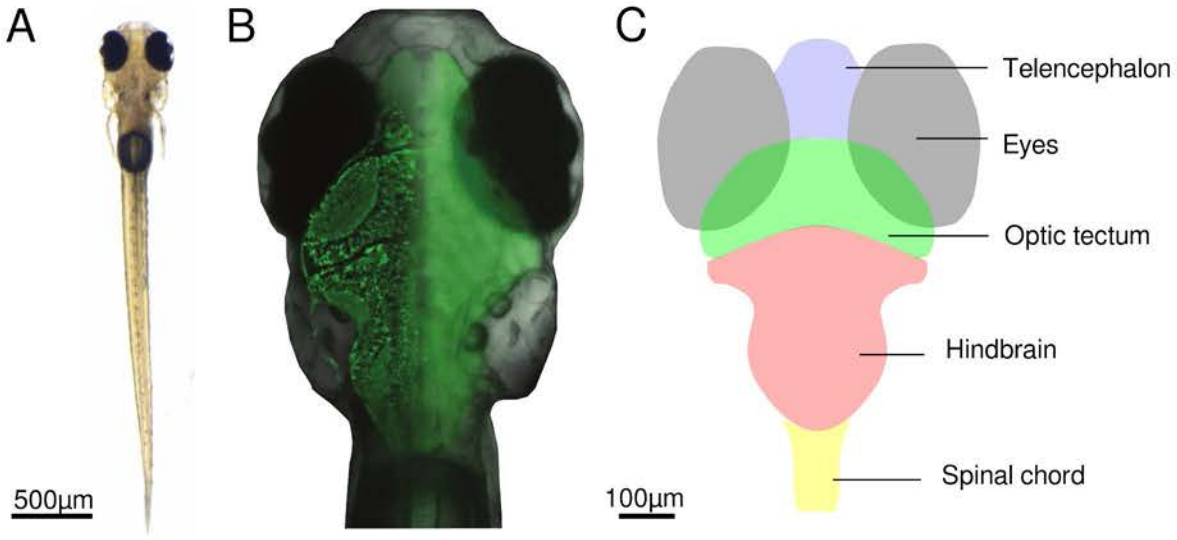

Fig. 1.13 **Brain anatomy of the zebrafish larva at 6 dpf. (A)**. Bright-field image of a zebrafish larva. **(B)** Overlay of a bright-field image of the larva head with images of it's brain acquired using two-photon microscopy (left part of the brain) and fluorescent imaging (right part of the brain). Note the spatial resolution on the left part obtained with two-photon microscopy. Neurons are labeled with the green fluorescent calcium indicator GCaMP5G. Image reproduced from Fetcho (2012). **(C)** Schematic drawing of the larval zebrafish brain showed in **(B)** representing the main parts of the brain (telencephalon, OT, hindbrain and spinal chord) and the eyes. Scale bar is common for **B** and **C**.

manipulations are commonly performed in an "all optical" fashion without the need for surgery, anesthesia or paralyzing drugs, just by embedding the larva into a low-melting agarose gel.

1.3.2 Zebrafish visual system neuroanatomy

Teleosts brains display basic vertebrate brain organization and their main projection pathways are similar to that of other vertebrate classes (Friedrich et al., 2010). However, the visual system components ie. OT and retina are relatively enlarged, certainly because of evolutionary pressure on vision immediately after hatching. In this chapter, I discuss basics aspects of the neuroanatomy of the visual system of the zebrafish larva.

The retina

Zebrafish possess a typical vertebrate retina organization consisting of three nuclear layers, separated by two plexiform (synaptic) layers (**Figure 1.5**). The outer retina, which is in close contact with the retinal pigment epithelium (RPE) contains rod and

four types of cone cells, including an ultraviolet-sensitive cone type. The wavelength response of the cone photoreceptors ranges from ∼350 to ∼580 nm (Endeman et al., 2013) although tectal responses to UV illumination are completely absent (Fosque et al., 2015).

The inner retina comprises cell bodies of bipolar, horizontal, and amacrine interneurons, and Müller glia-cell somata. Synaptic contacts between photoreceptors and the inner retina are formed in the outer plexiform layer. Closest to the lens is the ganglion cell layer, containing displaced amacrine cells and RGCs (**Figure 1.5**). The axons of the RGCs form the optic nerve and project to 10 different arborization fields (AF) within the larva's brain (Nevin et al., 2010).

Retino-recipient areas: arborization fields

RGCs project to at least ten AF (see **Figure 1.14**) but ∼95% project to the OT (AF-10). RGCs project to at least one AF (Semmelhack et al., 2014) and Baier H., unpublished results, and all ten AFs are contralateral. AF-1 also receives ipsilateral innervation throughout the hypothalamus (Burrill and Easter, 1994).

Several lines of evidence indicate that AFs are probably specialized in detecting relevant features of the external world and generating appropriate behaviors. For example Semmelhack and colleagues demonstrated that AF-7 is activated specifically by the optimal prey stimulus (3 angular degrees, noted 3°) and that ablation of this areas markedly reduced prey-capture behavior (Semmelhack et al., 2014). Similarly, two retino-recipient brain areas, AF-6 and AF-8, were shown to respond robustly, although not exclusively, to looming stimuli (two-dimensional representation of an object approaching on a collision course, which may represent a predator or an obstacle) (Temizer et al., 2015).

RGCs projections are organized in a retinotopic manner in AF10: neighboring RGCs terminate at neighboring positions in the OT. Nasal RGCs axons terminate in posterior regions and dorsal RGCs axons terminate on the ventral regions (**Figure 1.15**).

The optic tectum, AF10

Apart from direct (AF10) retinal efferents, the OT receives direct and indirect inputs from all sensory organs and other brain regions. It is mainly composed of GABAergic and glutamatergic neurons although few cholinergic neurons have been observed (Nevin et al., 2010). The majority, ∼95% of them are periventricular (PV) while the rest are found in the neuropil. The OT neurons can be categorized into five periventricular

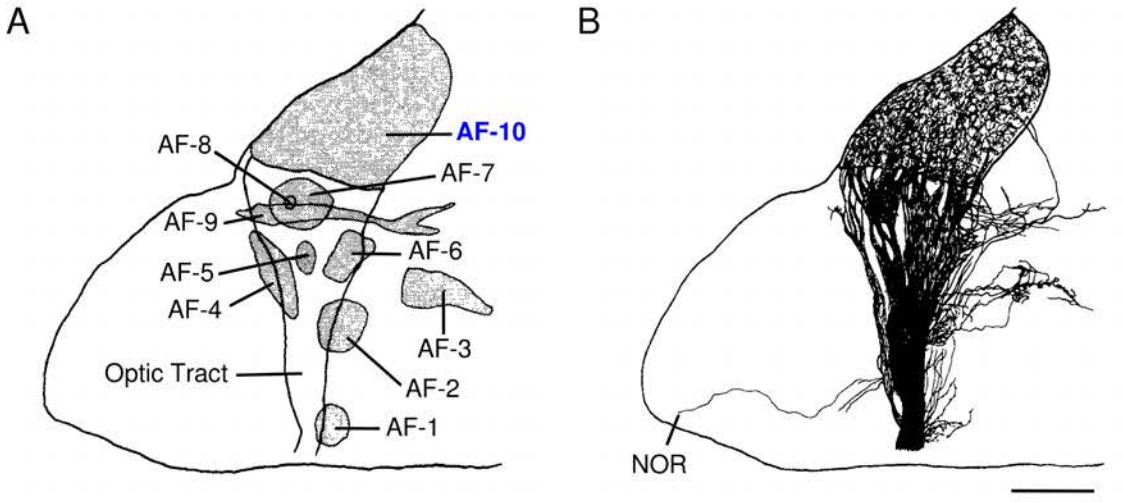

Fig. 1.14 **Zebrafish retinofugal arborization fields at 6-7 days post fertilization.** **(A)** Schematic representation of the retinofugal arborization fields (AFs). AF-10, the OT, is the largest retinofugal AF. **(B)** Schematic drawing of the observed intermingled projections in a larva labeled intra-ocularly with DiI (1,1'-dioctadecyl-3,3,3',3',tetramethylindocarbo- cyanine perchlorate). Note that one axon from the nucleus olfactoretinalis joins the optic tract. This structure has been suggested to modulate the sensitivity to visual cues in response to sexually relevant olfactory stimuli in teleosts (Rosillo et al., Neurscience, 2013). Reproduced from Burrill and Easter (1994).

morphological types (Nevin et al., 2010) (**Figure 1.16**) whose relationship between functional specialization and neurotransmitter type is still elusive. Indeed, recent results have demonstrated that a given morphological class (bi-stratified PV neurons) can involve both GABAergic and glutamatergic neurons (Gabriel et al., 2012; Robles et al., 2011).

Reports suggest that at least four functional PV classes exist although clear cut boundaries where not observed using two-photon calcium imaging (Niell and Smith, 2005). Briefly, two groups display strong receptive fields (width = ~40°) with one being poorly DS. A third group responds preferably to stationary stimuli and a fourth to whole-field decreasing illumination. In this study ~5% of recorded cells where left unclassified and probably comprise glia, immature non-excitable cells, neurons dedicated to other sensory modalities or unresponsive to the displayed stimuli.

Two reports have investigated functional properties of morphologically and neurotransmitter defined neuronal subtypes. The first, has provided convincing evidence that a sub-population of orthopedia^{+} (otpa) GABAergic bsPVINs neurons are strongly

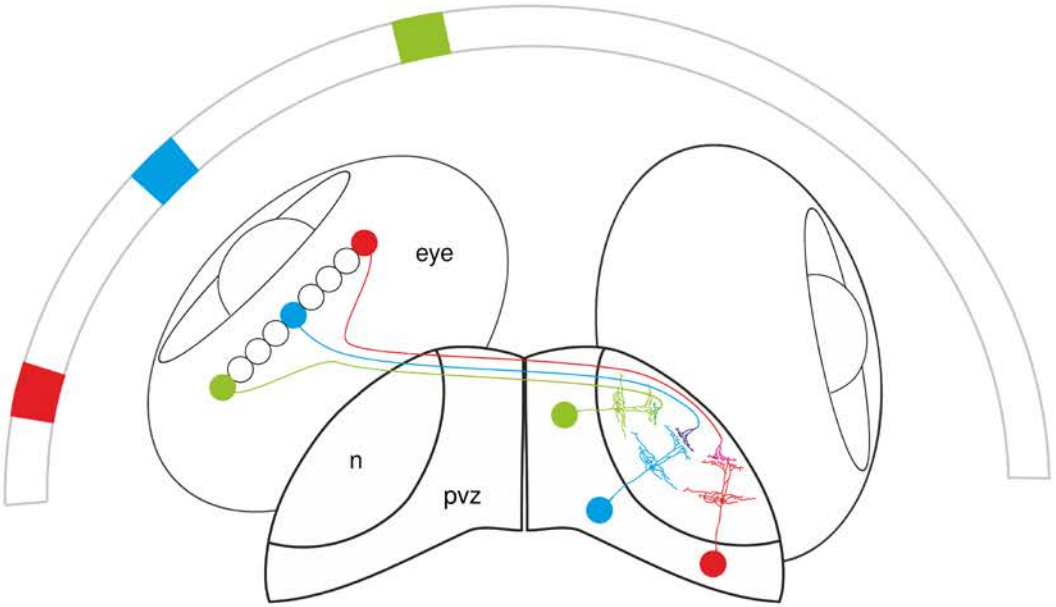

Fig. 1.15 **Zebrafish retinotopic organization of RGC inputs.** Neighboring RGCs project to neighboring regions of the OT in a contralateral manner. Therefore, there exists a map of the visual field embedded in the tectal tissue. The synaptic contacts occur in the laminated neuropil. n: neuropil, pvz: periventricular zone.

DS (Gabriel et al., 2012). The second, showed that superficial interneurons (SINs) from the neuropil participate in filtering visual inputs sizes and are required to capture preys (Del Bene et al., 2010). Apart from these reports, the functional structure of the OT at the cellular level remains unknown.

The OT projects directly to the opposite tectal hemisphere or indirectly through the nucleus isthmi [Meek 1983] and to hindbrain motor centers (Sato et al., 2007a) and indirectly to the spinal cord (Gahtan et al., 2005). Two identified tectal PV projections neurons have been observed: dlx5/6^{+} GABAergic neurons that project to rombomeres R1-R4 and brn3a^{+} glutamatergic neurons that project to R2 and R6 (Robles et al., 2011; Sato et al., 2007a). Recent studies using two-photon microscopy or SPIM have started to decipher how retino-tectal circuits participate in decoding visual signals to perform relevant behavior. Seminal results obtained in the OT are summarized below.

1.3.3 Optic tectum neurophysiology

As suggested by RGCs projections, a functional retinotopic tectal map of the contralateral visual field is an essential property of the OT (Niell and Smith, 2005; Romano et al., 2015). Indeed, contralateral dorsal and ventral visual hemifields are represented

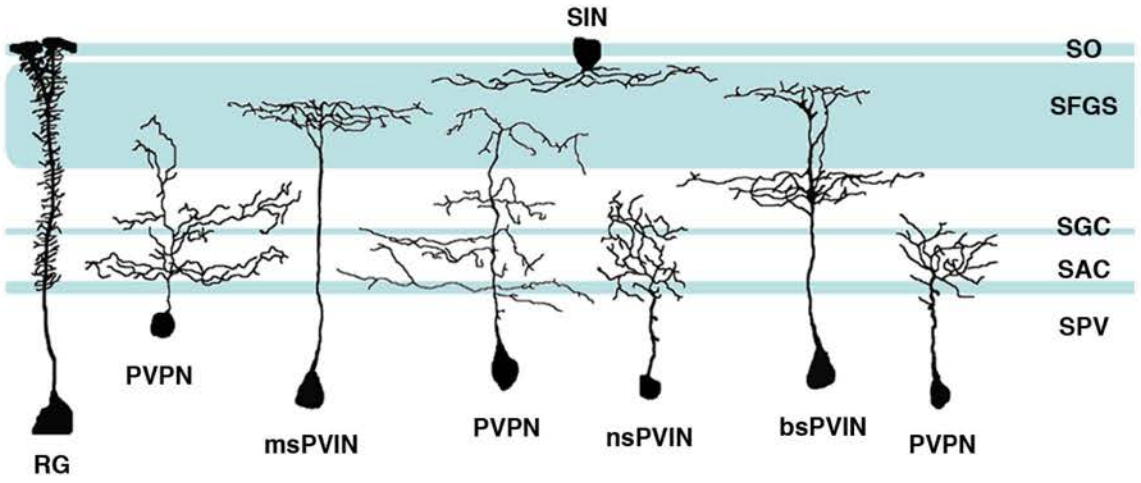

Fig. 1.16 **Cell-type diversity in the zebrafish larva optic tectum.** Commonly found cell types: RG: Radial glia extending one large process toward the pial surface of the OT, PVPN: periventricular projection neurons. periventricular projection neurons (PVPNs), periventricular neurons (PVINs) and superficial interneurons (SINs). Retinorecipient laminae in the tectum are indicated by light-blue shading. PVINs have been observed containing arbors that are non-stratified (nsPVINs), mono-stratified (msPVINs) or bi-stratified (bsPVINs). SO: stratum opticum, SFGS: stratum fibrosum et griseum superficiale, SGC: stratum griseum centrale, SAC: stratum album centrale, SPV, stratum periventriculare (or periventricular zone). Reproduced from Nevin et al. (2010).

in the dorso-ventral tectal axis, whereas the nasal and temporal hemifields are mapped in the rostro-caudal tectal axis.

Several functional roles have been attributed to the zebrafish OT among which: prey capture (Gahtan et al., 2005), time-interval memorization (Sumbre et al., 2008), computation of direction and orientation inputs (Hunter et al., 2013), filtering of objects sizes (Del Bene et al., 2010; Preuss et al., 2014) and looming evoked escape responses (Temizer et al., 2015). However, whether the OT is solely dedicated to performing these computations is unclear. Here I describe how the zebrafish retino-tectal circuit has been implicated in such computations and provide basic knowledge to study how visual micro-circuits are assembled during development.

Prey capture and tectal spontaneous dynamics

A recent study on the tectal spontaneous activity has shed light on the functional structure of OT neuronal network (Romano et al., 2015). Indeed, the OT spontaneous activity structure reflects the functional retinotopic map, organized in functional neu-

ronal assemblies. Strikingly, after characterizing the tuning curves of tectal neurons the authors showed that spontaneously active groups mimic activity patterns induced by visual stimulation. These spontaneously active assemblies comprised ∼80% of the significant neuronal pair-wise correlations observed in the tectal population and therefore account for a large fraction of the correlation structure of the OT population. Also, after removal of retinal inputs, they observed that the frequency and topological structure of spontaneous events remained unchanged. This suggests that OT spontaneous events do not reflect correlated feed-forward inputs from the retina, but it rather represents the local computations performed by the OT recurrent circuitry. Assemblies represented all-or-nothing "preferred" network states shaped by competitive dynamics, features reminiscent of attractor-like circuits. Furthermore, some of the functional neuronal assemblies features match those observed during prey-capture behaviors, and some of the assemblies were predictive of directional self-generated tail movements. These results suggest a behavioral correlate of spontaneous activity patterns and highlight their biological relevance. Indeed, they could be necessary to reduce the high dimensionality of the external world and extract relevant visual information of the visual scene in low-contrast cluttered environments.

Interestingly, these spontaneous neuronal assemblies might not underly direct neuronal connectivity but rather functional processing modules (Harris, 2005). However, no information exists on the neuronal subtypes (morphology, neurotransmitter types) forming these spontaneously active ensembles as well as the mechanisms underlying their formation.

OT computation of motion direction and orientation

Several groups have studied how extraction of the direction of motion is performed by the OT. The pioneering work of Niell and Smith showed that tectal cells are DS, a property that emerges 12 hours after the onset of the visually evoked responses (78 hours post fertilization) (Niell and Smith, 2005). These findings were confirmed by Ramdya and Engert by surgically removing a single tectal lobe, they forced the RGCs' axons to project and enervate the ipsilateral remaining tectum. In this single remaining tectum, they found neurons responding to apparent visual moving stimuli (two dots appearing at nearby locations with a given delay are perceived as a moving dot), where each dot was presented at a different eye. Several neurons responded to this apparent motion stimulus in a DS manner, responding equally well to moving stimuli presented to one or both eyes. Thus, they suggested that DS is an emergent property of the recurrent tectal circuitry (Ramdya and Engert, 2008). This mechanism

was later confirmed by Grama and Engert. The authors performed electrophysiological recordings of DS tectal neurons and found that their inhibitory inputs were strongly biased toward the null direction of motion, whereas the excitatory inputs showed little selectivity (Grama and Engert, 2012).

Opposite results were obtained by Gabriel et al. who found that DS in the OT neurons emerges from the combination of DS excitatory inputs and inhibitory inputs, selective to the null directions. It is possible that this ambiguity arises from recordings of different neuronal subpopulations (Gabriel et al., 2012). In this line, Hunter and Lowe et al. concluded that both studies are correct and the apparent disparity between the two reflects the full repertoire of DS processing in the retino-tectal system (Hunter et al., 2013).

Classification of visual stimuli by size

In the late 50's, neuroscience pioneer Jerome Lettvin was struck by the counterintuitive observation that immobile prey did not drive any capture behavior in frogs (Lettvin and Maturana, 1959). Later, when recording from RGCs he could detect so-called "bug-detectors", cells that where strongly activated by small dark spots moving within the field of view. He therefore concluded that prey detection is only determined by size and motion. From these influential experiments emerged the concept of "feature-detectors": neurons or circuits that extract behaviorally relevant signals out of sensory noise.

Using the zebrafish retino-tectal system, the neuronal substrate of such filtering has been partially resolved. In a recent work, Del Bene et al. presented small moving bars to immobilized larva and recorded the calcium fluctuations in the tectal neuropil using GCaMP1.6. Because the fluorescence rise was indistinguishable for different stimulus sizes they concluded that retinal input does not carry information about the size of the presented stimuli (Del Bene et al., 2010). However, when recording the fluorescence rise in PV neurons projections they observed that large stimuli were less efficient at exciting deep tectal projections suggesting that size filtering is an emergent property of the OT. The authors later identified GABAergic SINs located in the SO as spatial frequency filters. First, they showed that they preferably responded to large stimuli and second, that their selective ablation equalized responses to large stimuli in all tectal layers. Therefore, they concluded that the SINs participate in filtering of large stimuli to allow the tectum to respond to small size objects such as prey to drive feeding behavior.

A recent study has nevertheless challenged the idea that the tectum is the sole contributor to spacial filtering. By studying in details the RGCs projecting to the OT Preuss et al. remarked that the OT receives size tuned inputs. Conspicuously, superficial SFGS inputs were already tuned to small stimuli while deep inputs were tuned to large stimuli. Because GABAergic SINs had already been suggested to act as spatial frequency filters (Del Bene et al., 2010) the authors investigated whether their position within the SFGS could predict their functional inputs. Strikingly, the authors demonstrated that two SINs populations co-exist: SFGS projecting SINs responding phasically to large stimuli and SO projecting SINs responding phasically to small stimuli. Thus, superficial interneurons process small and large-size-selective signals depending on their dendritic target layer, consistent with the functional organization of retinal ganglion cell inputs (**Figure 1.17A-B**). The authors speculate that inhibitory SINs provide lateral inhibition to tectal sub-networks, participating in fine tuning of the spatial localization about small objects. Additionally, they could be instrumental in balancing downstream networks between two states: one that drives avoidance and the other that drives approach by selective inhibition (**Figure17C**).

However, SINs are not purely GABAergic (Boulanger-Weill et al., unpublished results) which might hamper the comprehension of their functional role. Further work is required to understand how size selective SINs process information and serve as relays to downstream tectal circuits and in what extent the OT participates in the fine-tuning of these inputs.

To conclude, classification according to the size of stimulus is not an emergent property of the OT since it is already present in RGCs. Overall, these results show that the OT relies on already tuned RGCs inputs to further refine sensory responses and perform behaviorally relevant classification to generate adequate directional motor behaviors.

1.3.4 The optic tectum as an ideal model to study circuit functional assembly

As illustrated before, the OT possess many technical advantages that helped improved our understanding of sensory processing in the visual system. Here I propose to use the zebrafish OT as a model to study the physiological development of newborn neurons and their integration into a functional visual circuit.

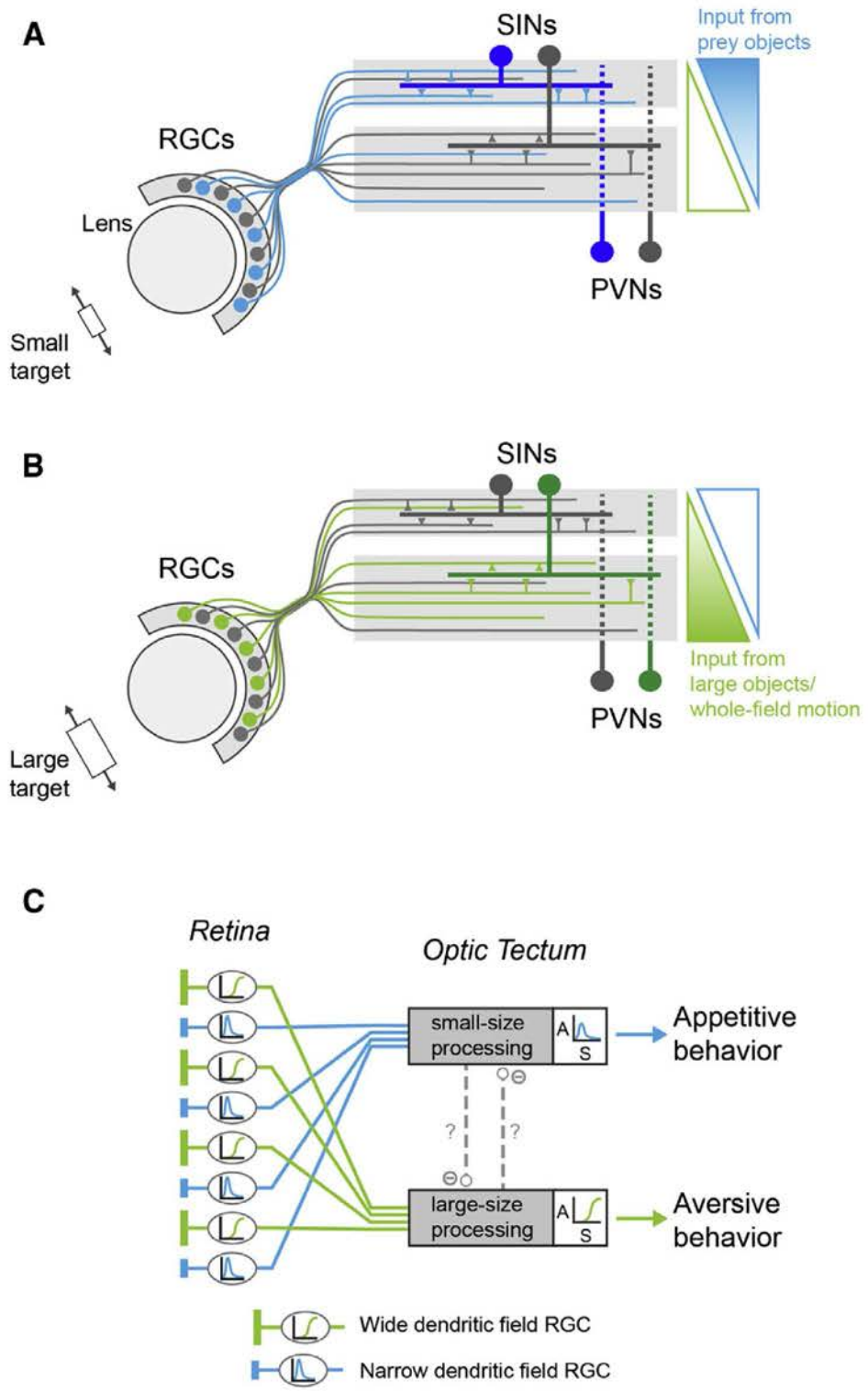

Fig. 1.17 **Proposed connectivity of size-selective circuits participating in object size classification**, legend next page.

Fig. 1.17 (Previous page.) **(A)** RGCs tuned for small sized objects project to superficial layers of the tectal neuropil (mainly in the stratum opticum, SO). A population of superficial interneurons (SINs) inputs receive these inputs and synapse with sized tuned periventricular neurons (PVNs). Their size tuning could result from specific connections in superficial or deeper retinorecipient layers. The proportion of inputs tuned for prey sized objects decreases as deeper layers of the neuropil are reached. **(B)** RGCs tuned for large sized objects project to deeper layers of tectal neuropil: mainly the stratum fibrosum et griseum superficiale (SFGS). A population of SINs receive these inputs and synapse with size tuned periventricular neurons (PVNs). Conversely, the proportion of inputs tuned for large "predator like" objects increases as deeper layers of the neuropil are reached. Note that the position of the SINs dendrites but not their soma, correlates with their size tuning. **(C)** Proposed tectal circuit for object classification and size-selective response selection. Size tuned RGCs project to two loosely defined different layers of the tectal neuropil (SO ans SFGS) and contact PVNs. These parallel inputs might form sub-networks that inhibit each-other (dashed lines). RGCs tuning curves are indicated in the insets in activity (A) versus size (S) plots. Reproduced from (Preuss et al., 2014).

The OT development is suitable for functional studies

Due to the larva's transparency, the entire brain activity can be recorded using two-photon microscopy or SPIM imaging without the need for surgery. This non-invasive preparation enables monitoring neuronal dynamics for up to ∼6 hours with SPIM, (Jouary et al., unpublished results) or chronic recordings of the same neurons (up to 4 days in a row with two-photon imaging, Boulanger-Weill et al., unpublished results). Due to the larva's small size, and the dense periventricular layer of the OT, a large number of neurons can be simultaneously recorded (up to ∼1000 neurons simultaneously, ie. ∼15% of the OT), which provides an unprecedented sampling of the vertebrate visual system.

Genetic tools can be used to sparsely label neurons: electroporation (Tawk et al., 2009) or Cre/lox conditional labeling (Sato et al., 2007a) and perturb their function (Hua et al., 2005). Optogentic tools can also be used to map connectivity (Kubo et al., 2014), or suppress neuronal activity (Arrenberg et al., 2010). Moreover, recently developed trans-synaptic viral tracing techniques (Mundell et al., 2015) will enable mapping connectivity of nascent or mature circuits.

Neuroepithelial neurogenesis in the OT

Neurogenesis in the OT occurs in two phases: primary neurogenesis that forms a neuronal scaffold up to 2 dpf and secondary neurogenesis that adds up neurons upon the

scaffold (Chapouton and Bally-Cuif, 2004; Recher et al., 2013). Secondary neurogenesis in the OT has been compared to a conveyor belt because of the spatiotemporal correlation between the maturation state of a cell and its position (Recher et al., 2013) (**Figure 1.18**). Indeed, migration doesn't seem to be a prominent feature of the OT neurogenesis (in adults: Zupanc et al. (2005), in larvae: Recher et al. (2013) and Boulanger-Weill J, personal observations) except for neuropil neurons (such as SINs) that must displace in the neuropil to reach their final positions.

OT neural progenitors form a monolayer, referred as the 'posterior midbrain layer' (PML) (**Figure 1.18**). The PML wraps the embryonic OT posteriorly and laterally and is composed of slow amplifying progenitors (SAPs) expressing neuroepithelial markers such as atypical protein kinase C and Zona occludens protein 1. SAPs then give rise to tectal fast amplifying progenitors (FAP) that differentiate into neurons. Interestingly, a different neurogenic system is present in the telencephalon where radial glia serves as NSCs (Rothenaigner et al., 2011). However, Ito et al., have observed that a few non-dividing adult tectal radial glia express the proliferating cell nuclear antigen (PCNA) and might serve as long-lasting progenitors Ito et al. (2010).

The molecular properties of the OT neural progenitors are still unclear but Recher et al., have suggested that Her5^{+} stem cells at the junction between the mid and the hindbrain (MHB) might contribute to neurogenesis in the OT (Recher et al., 2013).

To conclude, in the OT slow dividing neuroepithelial progenitors give rise to FAP located in the tectum. The cells exit the cell cycle and differentiate into neurons. They are constantly pushed anteriorly by the division of NP located more caudally (**Figure 1.18**). This continuous growth matches the growth of the retina and probably improves vision spatial resolution. Interestingly, the process that ensures the formation of such retinotopic circuits, while maintaining the functional structure of already matured networks, remains unknown. Studying this process is simpler in anamniotes because neurons are progressively added to already functional circuits while during mammalian development, massive waves of post-mitotic neurons maturate simultaneously while sensory transduction is still absent.

Using, the zebrafish OT, I addressed two open questions that are relevant to the assembly of sensory circuits: 1) What are the functional steps that undergoes a developing newborn neuron before and during the integration into mature sub-circuits? 2) To what extent developing cells change their fate when they integrate into mature sub-circuits, and how do these mature circuits influence the functional properties (RFs and DS) of the developing newborn neuron?

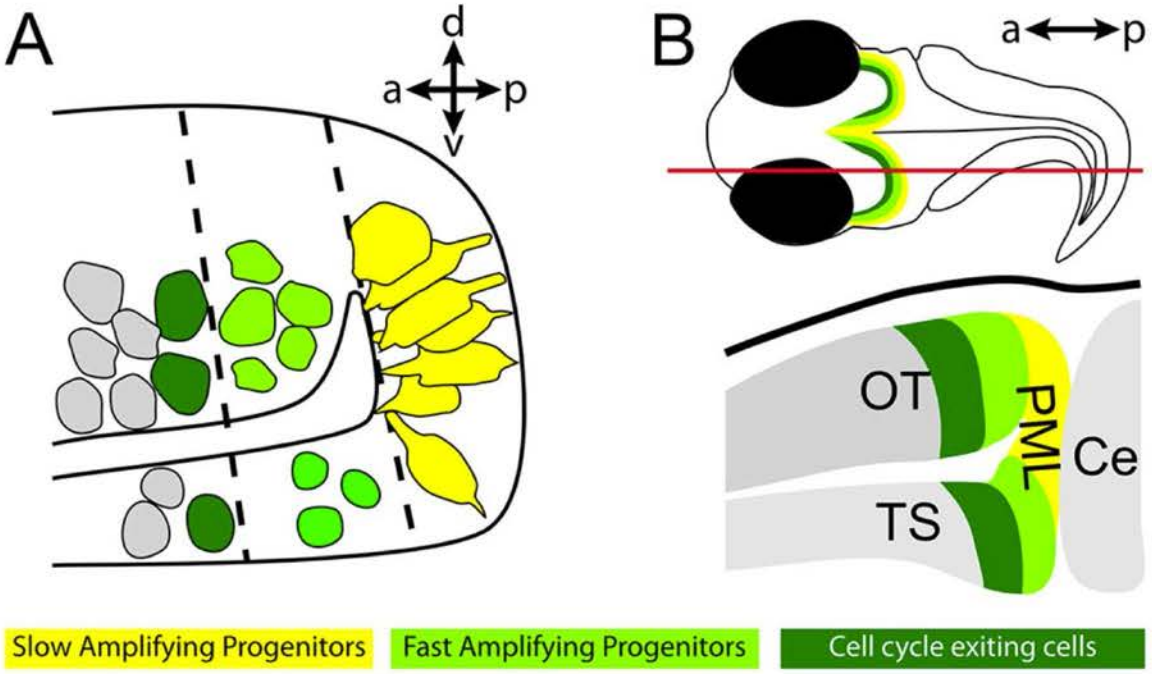

Fig. 1.18 **Neuroepithlial neurogenesis in the optic tectum (A)** At the posterior margin of the tectum lies the posterior midbrain layer 'PML' that connects with the torus semicircularis (TS). This layer is composed of neuroepithelial progenitors that give rise to fast amplifying progenitors in both structures (OT and TS). These cells exit the cell cycle and give rise to differentiated neurons. **(B)** Conveyor belt organization of the previously described stages in the OT at ~2 days post fertilization. Red line indicates the parasagittal section shown in the bottom panel. Ce: Cerebellum. Reproduced from Recher et al., 2013.

For this purpose, I had to genetically label newborn neurons and monitor their morphology and neuronal activity, and that of the surrounding mature neurons, for several days during the incorporation process. Specifically, I: **1.** developed a genetic method for labeling newborn neurons and follow their functional differentiation. **2.** Monitored, using two-photon imaging and optogenetics, the visually induced and spontaneous activity of newborn and mature neurons for several days. **3.** Developed tools to analyze the morphological and functional properties of newborn neurons and those of their mature counterparts.

Chapter 2

Material and methods

2.1 Zebrafish larva

2.1.1 Zebrafish husbandry

Embryos were collected and raised at 28.5 °C in 0.5x E3 embryo medium (E3 in mM: 5 NaCl, 0.17 KCl, 0.33 CaCl2, 0.33 MgCl2 pH 7.2 (Westerfield, 2000). Larvae were kept under 14/10 hours light/dark cycles and fed after 6 dpf. All experiments were approved by the Comité d'Éthique pour l'Expérimentation Animale Charles Darwin (Ce5/2009/027).

2.1.2 Transgenic and mutant zebrafish lines

For imaging experiments I used nacre (mitfa$^{-}/^{-}$) background zebrafish between 5 and 8 dpf. The nacre fish strain lacks melanophores (black pigmentation) but have a normal retinal pigment epithelium (Lister et al., 1999). Nacre larvae have a transparent skin enabling the monitoring of brain activity in an intact organism without the need for surgery or the use 1-phenyl 2-thiourea (PTU) to reduce pigmentation (PTU has been described to block pigmentation, but also decrease eye size and affect behavior).

For pulse-chase experiments I used wild-type zebrafish. For whole mount immunochemistry I used casper larvae (White et al., 2008). Casper line consists of a double mutation: nacre (mitfa$^{-}/^{-}$) crossed with roy orbison (roy$^{-}/^{-}$) mutants. Roy orbison (roy) zebrafish is a spontaneous mutant, and has a complete lack of iridophores, uniformly pigmented eyes, sparse melanocytes, and translucent skin.

To localize the neurogenesis sites in the OT, I used *Tg(EF1:mAG-zGem(1/100))* (Sugiyama et al., 2009). This line expresses a chimeric protein composed of mAG

(monomeric Azami Green fluorescent protein) and the N-terminal 100aa of zebrafish geminin. Geminin expression rises during the S phase and decreases during the G1 phase of the cell cycle. The amount of protein is controlled by an ubiquitination domain (1-100aa) throughout the cell cycle. Thus, the chimeric mAG-zGem(1-100aa) denoted mAG-zGem labels cells in S/G2/M phase.

To identify the neurotransmitter types of neurons I used *Tg(vglut2a:loxP-DsRed-loxP-GFP)* (Miyasaka et al., 2009) which labels glutamatergic excitatory neurons. *vglut2a* is a zebrafish orthologue of the mammalian gene encoding the vesicular glutamate transporter Vglut2a (Smear et al., 2007). Inhibitory GABAergic neurons were labeled in *Tg(gad1b:GFP)* (Satou et al., 2013). These lines were generated using the BAC (bacterial artificial chromosome) homologous recombination technique with either the I-Sce I-mediated method (Kimura et al., 2006) or the Tol2-mediated method (Suster et al., 2009). The two previously described transgenic lines were provided by Shin-Ichi Higashijima (Okazaki Institute for Integrative Bioscience, Japan).

2.1.3 Generation of transgenic lines

We performed recordings of brain activity by using calcium imaging as a proxy. This was achieved using two-photon excitation of the genetically encoded calcium indicator GCaMP5G (Akerboom et al., 2012) under the control of the pan-neuronal HuC promoter. A tol2 HuC:GCaMP5G vector was built by insertion of a 3.2kb fragment of the zebrafish *HuC* (*elav3*) promoter (gift from HC. Park, Kyungpook National University, Korea) (Park et al., 2000), then the GCaMP5G calcium probe (gift from L. Looger, Howard Hughes Medical Institute, Ashburn, Virginia, USA (Akerboom et al., 2012) was inserted into pT2KXIG in (from K. Kawakami, National Institute of Genetics, Shizuoka, Japan). *HuC* is a pan-neuronal promoter driving the expression of a RNA-binding protein, and involved in neuronal differentiation. In zebrafish, the 3.2kb proximal region encompassing 2771 base pairs of the 5'-upstream sequence up to the translation start site in +383/+385, has been shown to be sufficient to target all differentiated neurons (Park et al., 2000).

One-cell-stage nacre zebrafish embryos were injected with ∼20 ng of the plasmid DNA and ∼25 ng of transposase RNA (generated from pCS-TP plasmid, K. Kawakami). Injected embryos were raised to adulthood and crossed individually with nacre fish to obtain F1 embryos. These embryos were then screened and selected according to their level of transgene expression. The embryos with the highest expression were raised to adulthood and incrossed to obtain the homozygous *Tg(HuC:GCaMP5G^{GS16})* line.

2.2 Labeling of newborn neurons

2.2.1 Plasmids for electroporation

In vivo electroporation is a method for delivery of DNA, RNA or organic dyes in various tissue that offers precise temporal control. The following protocol was adapted from (Hoegler and Horne, 2010; Tawk et al., 2009) to label sparse tectal cells.

Three vectors were co-electroporated to perform long lasting labeling, yet without toxicity, of tectal neurons.The injected plasmids were based on the yeast Gal4/UAS (upstream activating sequence) system. Gal4 is a DNA binding protein which binds to the UAS sequence: CGG-N_{11}-CCG, where N can be any base and drives transcription of downstream coding sequences. Adapting the number of UAS repeats can be used to directly control the levels of transgene expression.

The first plasmid consisted of a tol2 HuC:Gal4 vector (obtained from Suresh Jesuthasan, Temasek Life Sciences Laboratory, Singapore, D'Souza et al. (2005)). The second plasmid was a 2XUAS:tdTomatoCAAX vector by successive ligations. The two UAS repeats upstream of the tdTomato fluorescent reporter sequence fused to the RAS derived CAAX sequence for membrane targeting, were chemically synthesized (Eurofins Genomics, Germany) and ligated into a Tol2 GFP destination vector designed using the Tol2Kit (Kwan et al., 2007). After trying several red fluorescent proteins (mCherry, mKate2, TagRFP-T, DSRed, mRFP and FusionRed), tdTomato was selected for it's low toxicity and good spectral separation using two-photon microscopy. Two UAS repeats were chosen to obtain low tdTomato expression. The latter was important for optimal spectral separation when imaging with a two-photon system (see following section). To further enhance spectral separation I added a Ras CAAX peptide to the 3' end of tdTomato coding sequence to target the protein to the membrane leading to spatial separation from GCaMP5G (GCaMPs are typically expressed in the cytoplasm minimally penetrating the nucleus). The third plasmid consisted of a 2XUAS:transposase vector generated by successive ligations. The co-electroporation of a transposase has been shown the enhance the stable genomic integration of transgenes and enables long lasting transgene expression in chicken embryos (Sato et al., 2007b). A pT3TTS-Tol2 (Balciunas et al., 2006) construct expressing the medaka transposase was used as a destination vector. The 2XUAS sequence was PCR amplified from the previously described 2XUAS:tdTomatoCAAX vector and ligated upstream of the transposase open reading frame. Co-electroporating vectors flanked by Tol2 sequences (**Figure 2.1A**) has been shown to drive stable transgene integration and long-term expression (Sato et al., 2007b).

To determine the neurotransmitter types of immature neurons I generated a 10XUAS:EGFP vector. Vectors containing a 10XUAS and EGFP sequences were obtained from the CB. Chien lab (The University of Utah, Salt Lake City, USA). The EGFP coding sequence was inserted into the 10XUAS vector by classical cloning methods (**Figure 2.1B**). This vector was co-electroporated with the previously described HuC:Gal4 and 2XUAS:transposase constructs in *Tg(vglut2a:loxP-DsRed-loxP-GFP)* to determine if neurons labeled by electroporation were glutamatergic. To test whether the neurons were GABAergic, I electroporated the constructs depicted in **Figure1A** in *Tg(gad1b:GFP)* (Satou et al., 2013).

To test in what extent the observed labeling was promoter dependent, I cloned ∼3,0kb fragments of the 5'-flanking sequences of the musashi1 (*msi1*) and cyclinb2 (*ccnb2*) genes as controls. *msi1* has been used as a marker for pluripotency in the medaka OT (Alunni et al., 2010) and ccnb2 is a key cell-cycle regulator involved in S to M phase transition (Duffy et al., 2005). I expected that these promoters would drive transgene expression in neuronal progenitors. Sequences upstream of the human homologs of *msi1* and *ccnb2* coding sequences were PCR amplified from genomic DNA of 5-week-old wild-type zebrafish and inserted into a PCRII vector using TOPO cloning (Life Technologies, USA). The isolated promoters were sequenced and then cloned up stream of the EGFP and tdTomatoCAAX coding sequences, respectively (**Figure 2.1C**).

2.2.2 Electroporation setup

Before electroporation, larvae were embedded in a drop of 1.8% low-melting agarose (Invitrogen, USA) in Evans solution (134 mM NaCl, 2.9 mM KCl, 2.1 mM CaCl2, 1.2 mM MgCl2, 10 mM glucose and 10 mM Hepes at 290 mOsm and pH 7.8) and covered with E3 medium. The electroporation device consisted of two 125 μm platinum-iridium (90/10%) 120 μm wires (GoodFellow, UK) spaced by ∼1mm mounted on a micro-manipulator. Glass injection needles were pulled from capillaries (1.0 mm outer diameter, 0.5 mm inner diameter, without filament, FHC, USA) on a Kopf 720 puller (David Kopf Instruments, USA) and back loaded with DNA solution. The needle tip was broken off with forceps. The injection solution consisted of 2XUAS:tdTomatoCAAX vector diluted to a final concentration of 2 μg/μL with other vectors at 1 μg/μL (**Figure 2.1A**). For better visualization of the injection, phenol red was added to the solution in a final construction of 0,05%. The solution was injected by several pressure pulses at 4 dpf (corresponding to 0 days post electroporation) until the tectal ventricle was swollen with red solution (**Figure 2.2**) using a pneumatic picopump

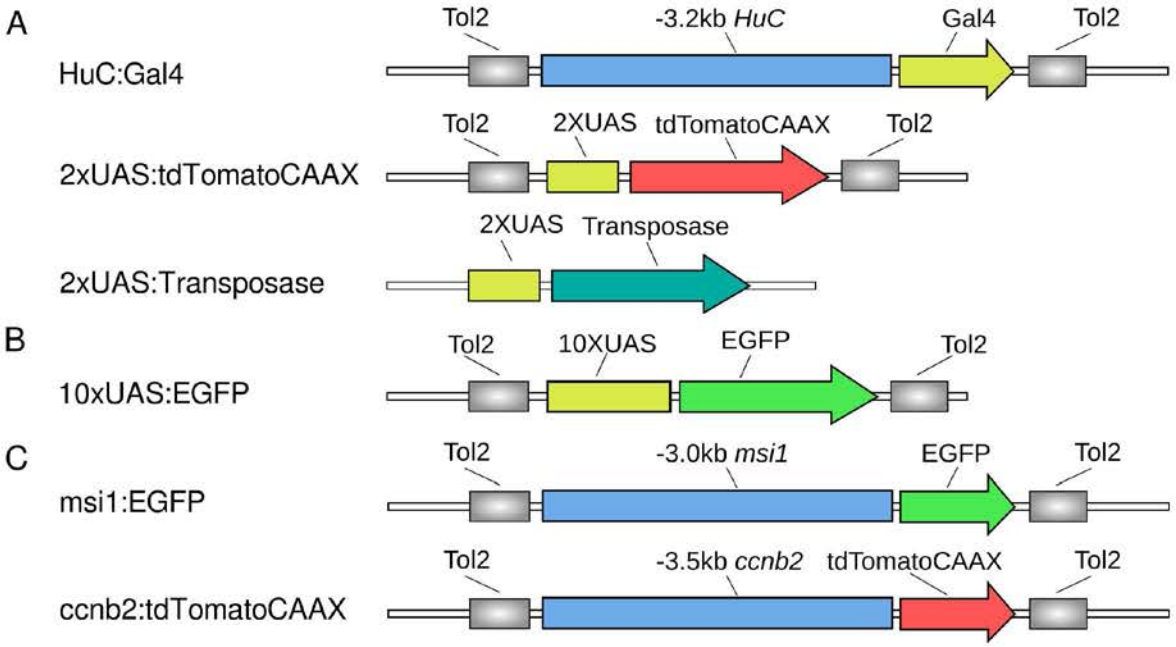

Fig. 2.1 **Vectors used for electroporation.** **(A)** Vector cocktail used for two-photon calcium imaging in *Tg(HuC:GCaMP5G)*. When electroporated into Tg(gad1b:GFP), these vectors were used to determine neuronal neurotransmitter types. **(B)** Vector designed to determine neuronal neurotransmitter types in *Tg(vglut2a:loxP-DsRed-loxP-GFP)* in combination with the HuC:Gal4 construct. **(C)** Two vectors designed to test whether electroporation is promoter dependent.

(Pv 820, World Precision Instrument). Immediately after the injection, one electric square pulse was delivered using a SD9 Stimulator (Grass Technologies, USA): 4ms at 20V. The electric pulse was monitored using an oscilloscope (Tektronic, RDS 2022C, USA). The electric pulse was harmless to the fish. The mortality rate was ~2% (n=59 electroporated larvae) at 6 dpe and comparable to non electroporated controls (~1,5%, n=150). Labeled cells did not show any sign of toxicity, such as membrane blebbing or protein aggregation Shaner et al. (2005) (**Figure 2.3**). Labeled neuronal subtypes displayed simple dendritic arborizations that became more complex along time (**Figure 2.3**).

Fig. 2.2 **The electroporation technique.** Left panel: 4 dpf fish embedded in agarose with the injection capillary located at the surface of the skin overlying the tectum (indicated with an asterisk). Electroporation electrodes nearby are indicated by their polarity. In this configuration neurons in the left tectum were labeled. Right panel: same fish after the pressure injection, filling the tectal ventricle with DNA solution. Note the phenol red color indicating that the solution has been injected.

2.2.3 Specificity of the electroporation technique

To test for electroporation specificity for immature neurons, I first electroporated using higher voltage (30V) while keeping other parameters constant. Increasing the voltage labeled a much larger number of neurons **Figure 2.4A**. Interestingly, the dendritic arborization of the labeled neurons was more developed than using the sparse labeling parameters ie. lower voltage.

Second, to test to what extent the observed labeling was promoter-dependent, I used the *msi1* and *ccnb2* based constructs. Surprisingly, the *msi1* specifically labeled radial

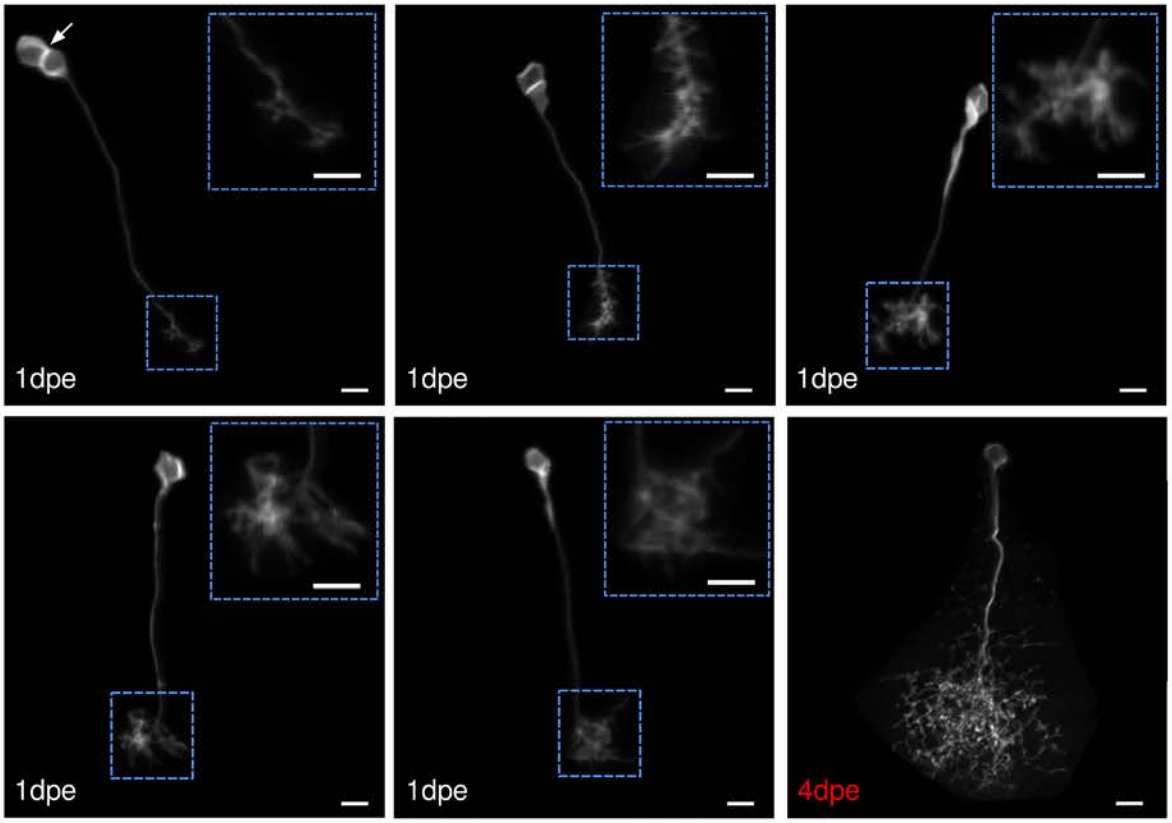

Fig. 2.3 **Examples of sparsely labeled neurons.** Stacks of labeled neurons acquired one day after electroporation. Insets are enlarged views of the immature dendritic arborizations. Note that electroporation sometimes labeled clusters of cells, as in the first panel. A developed labeled neuron imaged at 4 dpe is shown in the bottom right panel as control. Clusters were excluded for morphological reconstructions and quantifications. Pictures were acquired using a two-photon microscope one day after electroporation. Scale bar: 5 μm.

glia while, the *ccnb2* promoter labeled clusters of immature neurons (**Figure 2.4B** and **Figure 2.4C**). *Msi1* has been demonstrated to be expressed in OT neuroepithelial cycling cells in medaka (Alunni et al., 2010). However, *msi1* has not been shown to be a radial glia marker although one study in the zebrafish OT has suggested that RG might serve as dormant progenitors that can be harnessed during regeneration or in response to activity-dependent mechanisms (Ito et al., 2010).

Interestingly, the *ccnb2* promoter labeled mixed clusters of immature neurons and dividing progenitors (data not shown) that were devoid of neurites (as in **Figure 2.4C**). Expression was rapidly lost after 1 dpe suggesting that the *ccnb2* promoter was no longer able to drive transgene expression in more matured neurons.

Pure population of sparse, differentiated immature neurons were consistently labeled using *HuC*-based low-voltage labeling, but not using other voltage/promoters conditions. Because the *ccnb2* promoter also labeled immature neurons the promoter used is not solely responsible for the electroporation cell-type specificity but rather a combination of the voltage and the promoter used. Therefore sparse labeling using the *HuC* promoter is well suited to consistently label immature neurons and perform chronic imaging.

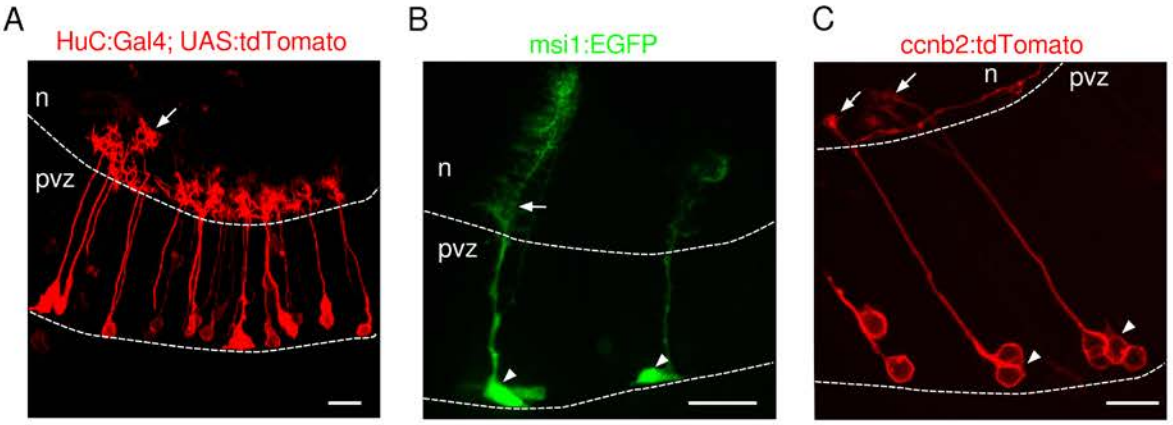

Fig. 2.4 **Electroporation parameters and constructions used target specifically newborn neurons.** (A) Labeled neurons using a 30V pulse using the same constructs described previously. Note the density of the labeling, the overlapping and enlarged arborizations (arrow) precluding easy chronic imaging of single developing neurons. (B) Labeled radial glia using the *msi1* promoter. Note the triangular shapes of the somas (arrowheads) and the characteristic lateral branches forming a dense tube like arbor in mature cell types (arrow). (C) Labeled clusters of immature neurons using the *ccnb2* promoter. Note the immature dendritic arborizations (arrows) and the clusters of neurons (arrowheads) with certain neurons being devoid of neurite. Scale bar: 10 μm. Pictures were acquired as stacks using a two-photon microscope one day after electroporation.

2.2.4 Displacement of newborn neurons in the optic tectum

Dividing cells incorporate the thymidine analogue BrdU (5-bromo-2'-deoxyuridine) that can be labeled using immuno-chemistry. To monitor the displacement of tectal newborn neurons, I performed a typical pulse-chase experiment: BrdU was diluted in E3 at 10mM to label only a subset of dividing cells and dissolved in 15% DMSO to ensure penetration through the skin. 4 dpf larvae were placed in the solution for 20 minutes at 4°C degrees. The solution was quickly removed and washed with E3 medium. Fish were placed back in the incubator for 30 minutes and fixed at the following stages : 0h, 24h, 48 and 72h in 4% PFA for 24h at 4°C. Larvae were then soaked in 15% sucrose at 4°C overnight and embedded in gelatin containing 15% sucrose. The freezing procedure was performed in the following way: gelatin/sucrose blocks were frozen for 30s in isopentane previously cold down with liquid nitrogen. Blocks where then kept at -20°C for subsequent sectioning. 20 μm-thick sections were cut using a cryostat (Cryocut1800; Leica) and stuck on Superfrost-plus glass slides.

For brain sections, each slide was washed several times in PBT and then blocked in blocking buffer (PBT complemented with 10% goat serum and 0.5 Triton X-100) for 1 h at room temperature before application of the primary antibody. For primary antibodies, we used rat anti-BrdU (1:500; Abcam, UK), mouse anti-PCNA (1:1000; Sigma, USA), chicken anti-GFP (1:100; Santa Cruz, USA). For secondary antibodies, we used Alexa Fluor 488-, 546- and 647-conjugated subclass-specific antibodies (1:500; Invitrogen, USA). Sections were embedded in fluorescence mounting medium (Dako, USA). For immunodetection of BrdU, the samples were incubated in 2 M HCl for 30 min at 37°C before blocking. For nuclear staining, the samples were incubated in DAPI (4',6'-diamidino-2-phénylindole) (1:10000; Invitrogen, USA) for several minutes after immunohistochemistry was performed. Immunostainings were imaged with a LSM700 confocal microscope (Carl Zeiss Microscopy, Germany) using a 20X oil-immersion objective.

2.3 Two-photon calcium imaging

2.3.1 Experimental setup

Recording chamber

Larvae were embedded in 1.8% low-melting agarose (Invitrogen, USA) in E3 embryo medium on an elevated stage within a custom-made cylindrical chamber filled with E3

embryo medium. The elevated stage enables the larva to have an unobstructed view of the entire field of view of the projected stimuli (**Figure 2.5**).

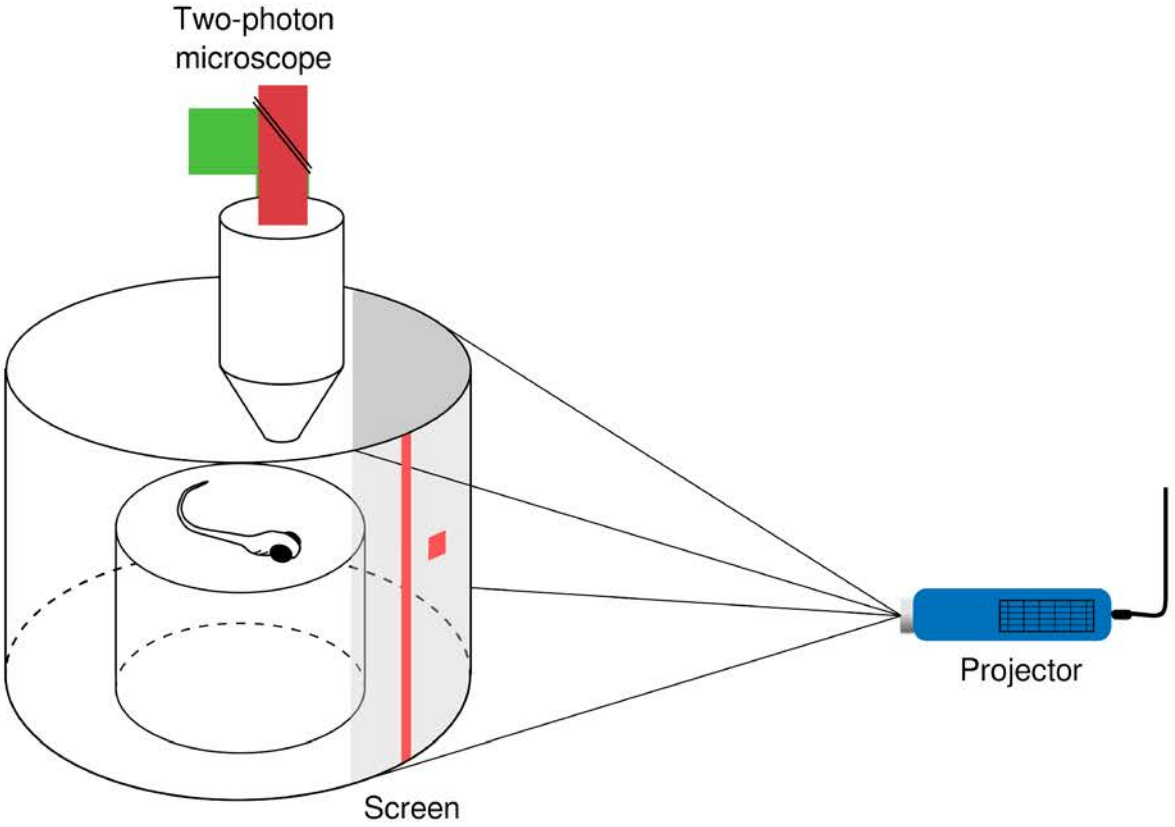

Fig. 2.5 **Recording chamber.** Stimuli are presented on a screen wrapped around the chamber. Example of square and bar stimuli are shown. The two-photon microscope objective is located above the head of the animal.

Visual stimulation

Visual stimuli were projected on a screen (#216 White Diffusion, Rosco Cinegel, UK) around the recording chamber, using a pico-projector (refresh rate: 60 Hz, P4X, AAXA, USA), covering a field of view of 90° x 40° (horizontal x vertical). The opposite side of the recording chamber was covered with low-reflection black tape (T137-2,0, ThorLabs, USA) to prevent the reflection of the stimulus. To avoid interference with the GCaMP5G emission signal (peaking at 547 nm and filtered using a 520/50 band-pass filter), only the projector's red LED was used and a long-pass filter (BLP01-561, Semrock, USA) was placed in the front of the projector, thus the stimulus consisted in red light.

Larvae were carefully aligned to the projector with the help of a custom-made program that mapped azimuth angles on the chamber's projection screen. In order to minimize projection distortions due to the cylindrical chamber, we calibrated the projection to compensate as best as possible for the chamber's curvature.

To study the receptive fields, DS and spontaneous dynamics of newborn and mature neurons we used the following stimulation paradigm: 5° light spots were presented at 36 different positions of the field of view (90° horizontal x 40° vertical), lasting 1s and centered orthogonally to the larva's midline. The light spots were repeated 20 times at each of the different positions (20 trials). Then, 4° wide x 90° long moving bars were presented in the four cardinal directions moving at 45°/s covering 90° x 90° of the field of view (4 trials per direction). In all cases the order of the stimuli positions and directions were randomized, and the inter-stimulus interval was 5s (from onset to onset). Overall, a total of 16 moving bars (4 per cardinal direction) and 720 light spots (20 per position) were presented per experiment. We discarded imaged videos without visual responses in either block. In chronic recordings, visual stimulations were divided in two blocks of 5 trials separated by 30 minutes while spontaneous activity was monitored (in the absence of any sensory stimulation, darkness) (**Figure 2.6**).

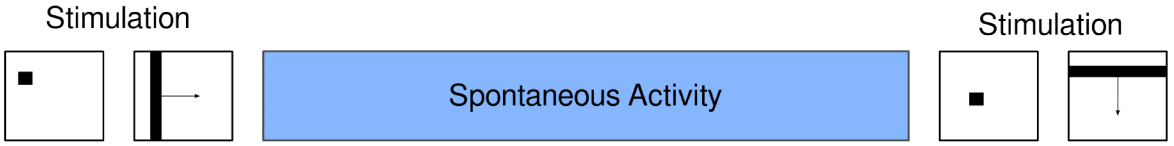

Fig. 2.6 **Stimulation paradigm used for chronic recordings.** Random 5° squares precede bars moving in the four cardinal directions, then spontaneous activity is recorded while sensory stimulation is abolished. Another block of stimuli is presented afterwards.

All visual stimuli protocols were programmed using the Psychtoolbox Brainard (1997) for Matlab (Matlab, The MathWorks, Inc) and synchronized with the two-photon calcium imaging acquisition software ScanImage 3.8 (Pologruto et al., 2003) using an TTL delivered by a Matlab-controlled I/0 board (ActiveWire Inc, USA) or an Arduino Uno (Arduino, Italy).

Recording neuronal activity and morphology using two-photon scanning fluorescence microscopy

In contrast to epifluorescence wide-field imaging, single-photon and two-photon scanning microscopy (Denk et al., 1990) enables monitoring neuronal activity exclusively from the objective focal plane and resolve their activity with single-cell resolution. Theoretically,

in two-photon excitation each of the photons carries out half of the energy necessary to excite the fluorophore (double of the wavelength). Since at least two photons have to hit the fluorophore within a very short time window (attoseconds) to send an electron to a high-energy state, the probability of this process to occur is extremely low. To increase this probability, a pulsed infrared laser is necessary to provide large photon densities required to generate significant two-photon excitation. Since the photon density necessary to induce two-photon excitation is only achieved at the focal plane, confocality emerges directly from this non-linearity and also limits photo damage to the plane being scanned. Finally, since excitation light is infrared it is invisible to the zebrafish larva, avoiding the direct excitation of the retina by the excitation laser, an important issue when studying the visual system (Ahrens and Engert, 2015; Niell and Smith, 2005; Ramdya and Engert, 2008; Sumbre et al., 2008).

Tg(HuC:GCaMP5G) was used to study the neuronal network dynamics in the OT. The OT region was imaged at a retinotopically organized plane at $\sim$60 μm below the skin surface using the cerebellar commissure as anatomical and visual responses as a functional references. Planes showing no retinotopicity were discarded. Due to the Ca^{2+} affinity of GCaMP5G ($\sim$460$\pm$11 nM) (Akerboom et al., 2012), significant calcium transients (see 2.3.2, **Inference of calcium events**), most probably involved several action potentials (Yaksi and Friedrich, 2006).

i. The two-photon scanning fluorescence microscope The imaging set-up was based on a MOM system (Sutter, USA) with a 25x NA1.05 Olympus objective and a Mai Tai DeepSee Ti:sapphire laser tuned at 920 nm. The output power at the focal plane was less than 3 mW. The green GCaMP5G and the red dTomato emitted photons were collected by the objective and deflected towards a photo-multiplier (PMT) via a 670dcrx (Chroma, USA) dichroic (objective dichroic). Infra-red light was filtered from the emission path by a FF01-680 short-path filter (IR Blocker, Semrock, USA). The wavelength of the emitted fluorescence was separated into two channels (green and red) by a FF01 520/70 band-pass filter (Semrock, USA). Band-pass filters FF01-520/70 (green) and FF01-607/70 were placed before the PMTs (H1070, GaAsP from Hamamatsu, Japan). The emission signal was pre-amplified with a SR-570 (Stanford Research Systems, USA) and acquired using ScanImage (Pologruto et al., 2003) at 3.91 Hz, with 256 x 256 pixels resolution (see **Figure 2.7** for a schematic of the optical excitation and emission paths).

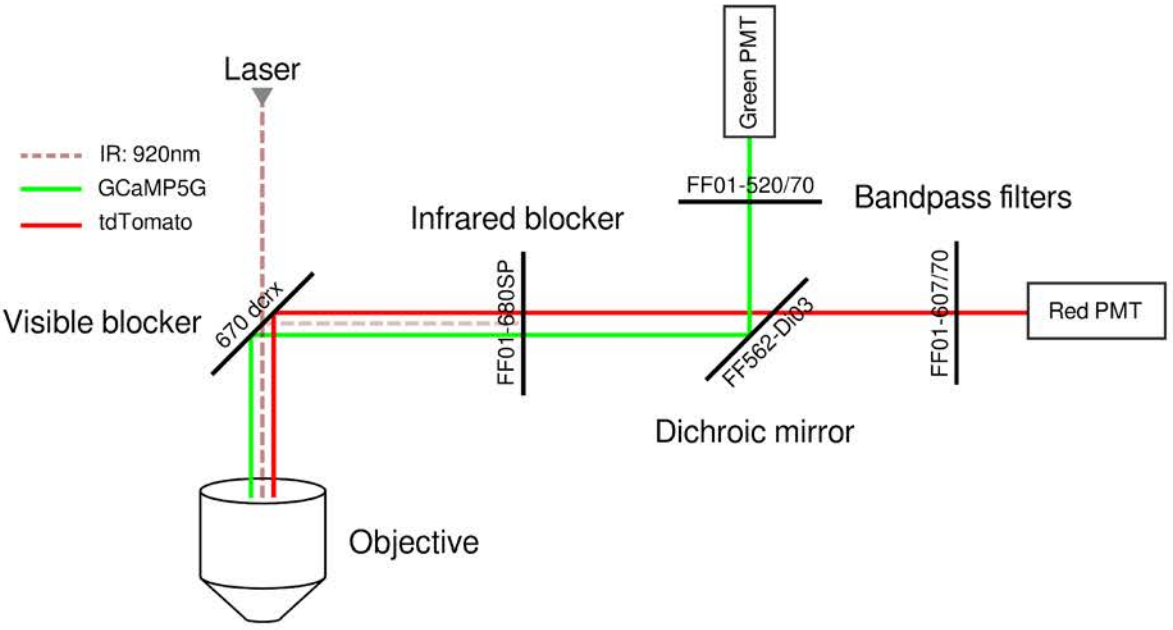

Fig. 2.7 **Two-photon excitation and emission paths.** To separate excitation and emission photons a first dichroic mirror (670 dcrx, Chroma, USA) selects photons with wavelength >670 nm. The laser beam then enters the objective and is focused on the preparation expressing both GCaMP5G and tdTomato. Emitted green and red photons are collected by the objective and deviated towards the PMTs via the 670 dichroic mirror. To prevent IR photons to reach the PMTs, an infrared blocker (FF01-680SP, Semrock, USA) was added to the emission path. A second dichroic mirror transmits red photons and deflects green photons (FF562-Di03, Semrock, USA) to each PMT. In addition, bandpass filters were placed before each PMT (FF01-520/70 and FF01-607/70 for green and red photons, respectively, all from Semrock, USA).

ii. Spectral separation Although simultaneous two-photon imaging of fluorophores pairs has already been performed at a single wavelength Kawano et al. (2008); Ohtsuki et al. (2012), recording calcium activity together with detailed neuronal morphology with optimal spectral separation still constitutes a challenge. Indeed, to isolate fluctuating calcium signals from stable morphological labeling, spectral contamination has to be minimized. In our initial preparation, GCaMP5G fluorescence was largely contaminated by tdTomato. Such observation can be explained by different phenomena: either by large difference in fluorophores expression levels or by large difference in two-photon brightness (TPB) σ_2', expressed in Goeppert-Mayer (GM) units ($1GM = 10^{-50} cm^4 s$). TPA brightness $\sigma'_2 = \sigma_2 \phi$ where σ_2 is the two-photon cross section or two-photon absorption and ϕ is the fluorophore quantum yield.

σ_2 characterizes the probability of the simultaneous absorption of two photons whose energies add up to match the molecular transition energies and provides a direct estimate of the detected fluorescence rate per molecule (Drobizhev et al., 2011; Mütze et al., 2012). Upon 920 nm, two-photon excitation EGFP and tdTomato have TPBs of ∼27,5GM and ∼30,0GM respectively (Drobizhev et al., 2011). According to Akerboom et al. (2012), $\phi_{GCaMP5G} = 0,96\phi_{EGFP}$ (in Ca^{2+} saturating conditions) therefore the difference in TPB cannot explain the spectral contamination of GCaMP5G fluorescence by tdTomato.

Most probably, because red fluorescent proteins fluorophores and the calcium indicator were expressed using different means: GCaMP5G by transgenesis and tdTomato by electroporation, a large difference in green and red fluorescence (red>green) intensities was observed. To overcome this issue tdTomato was greatly reduced by decreasing promoter strength and by membrane addressing to ensure topological separation (see 2.2.1, **Plasmids for electroporation**).

To further optimize spectral separation of red photons I used 565dcxr or FF562-Di03 dichroic mirrors (all from Semrock except 565dcxr from Chroma) to deflect emitted red and green photons towards dedicated PMTs (**Figure 2.7**). A FF01-607/70 bandpass filter was placed upstream of the red PMT. Using such filters accurate spectral separation was achieved (**Figure 2.8** and **Results**) and was sufficient to perform both calcium imaging together with detailed study of morphology of sparsely labeled neurons.

iii. Online compensation for drifts in the Z axis Probably due to agarose dilatation during the experiments, drifts in the Z plane are sometimes observed. To compensate for the Z drifts, I used an algorithm which measures the cross correlation

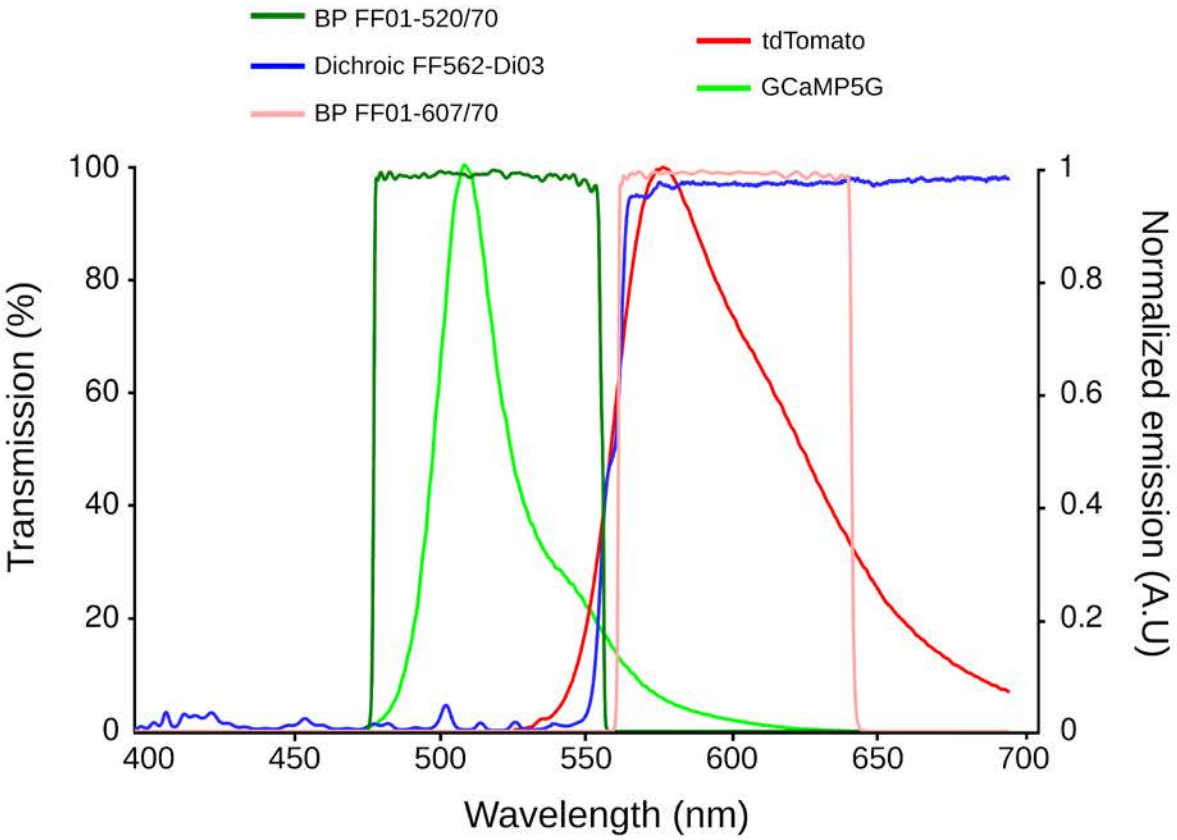

Fig. 2.8 **Emission spectra of combined fluorophores and transmission of the spectra separation filters.** The emission curves for fluorophores are normalized to their maximal fluorescence values. Note that a significant part of the tdTomato emission curve is contained within the range of high transmission of the GCaMP5G dedicated bandpass filter. This can lead to contamination of the green PMT with red photons.

of the images acquired with the images of 3 other images acquired at 3 different focal planes. Every 100 frames an average image was generated and and cross-correlated with the 3 reference images acquired before the onset of the experiment (the recording plane and 2 planes: 2,44 μm below and above the recording plane). If the correlation was higher with the superior or inferior planes an automatic compensation was performed in the opposite direction by displacing the objective by increments of 0,44 μm until the correlation of the running average was maximum with the reference plane (the algorithm was developed by Adrien Jouary, a PhD student in the lab).

iv. Reconstruction of neuronal morphology Neuronal morphology was recorded with the same set-up use for two-photon calcium imaging using ScanImage (Pologruto et al., 2003). Semi-automatic neuronal tracings were performed using Imaris after a Matlab pre-processing step to remove the skin and facilitate the detection process. The total dendritic volume was extracted with Imaris.

2.3.2 Pre-processing of the acquired images

Image registration

The calcium imaging experiments were saved as a series of 16 bits TIFF files. The first step in the analysis of the calcium imaging data was to compensate for possible drifts in the XY plane. For this purpose, we registered the images using the Image J plugin Template Matching (Tseng et al., 2012) in combination with a custom-made algorithm. Furthermore, in non-paralyzed agarose-restrained larvae, eyes or tail movement commands can sometimes generate moving artifacts perturbing the analysis of calcium transients. Movement artifacts were detected according to large deviations in the cross-correlation between successive frames. All frames with large deviations were then manually inspected and removed if necessary. Thanks to the low-melting agarose elasticity, the imaged plane almost invariantly returned to its original position, following a larva's movement, permitting to discard only the frames showing movement artifacts and keeping the rest. If this was not the case, the complete experiment was discarded. Artifact episodes rarely exceeded 10 consecutive frames in length. We did not include frames showing moving artifacts in the subsequent analysis.

Segmentation – neurons identification

Segmentation was achieved using a custom made Matlab program originally written by Sebastian Romano and subsequently optimized by several members of the lab. Regions

of interest (ROIs) corresponding to each of the imaged neurons were semi-automatically detected on a morphological basis by analysis of an averaged picture of the recorded region.

We implemented a series of digital imaging processing techniques (Gonzalez et al., 2004) in a custom-made program that produced putative ROIs layouts that were afterwards manually curated. GCaMP5G is mainly localized in the cytosol with minimal penetration to the cellular nuclei. The algorithm first identified neuronal ROIs that corresponded to individual nuclei by local fluorescence intensity wells. In order to flatten non-relevant intensity fluctuations in these minima, the eroded version of the imaged region was morphologically reconstructed under the mask given by same image. Local minima were detected by applying a user-defined threshold to the extended-minima transform of the resulting image. Finally, to obtain the ROIs perimeters we took advantage of the high density of the tectal stratum periventriculare (SPV) neurons. We calculated the euclidean distance transform of the local-minima image and we performed a watershed segmentation to obtain the boundaries between neurons (Romano et al., 2015).

The obtained ROIs were manually inspected and corrected when needed. ROIs typically included the neuronal nuclei and the thin cytosolic surrounding ring, conservatively excluding the outermost cytosolic perimeter that could potentially be subject of cross-neuron fluorescence contamination due to the high neuronal density (**Figure 2.9**). This procedure gave similar results to fully-manual ROI selection, accelerated the process by ∼5-fold and minimized human subjectivity. Sparsely labeled tdTomato expressing neurons were manually selected and their identity was saved for later analyses. Finally, we computed the changes in calcium associated with the activity of each neuron along time, by averaging the fluorescence of all pixels within the ROIs.

Inference of calcium events

Analyses described in the following section were performed using Matlab programs first designed by Veronica Perez-Schuster and Sebastian Romano and further optimized for the need of the project.

In order to infer the significance of the Ca^{2+}-related fluorescence transients associated with neuronal activity, we used a method that infers the statistical significance of single-neuron calcium dynamics in an adaptive and unsupervised manner. It considers that any event in the fluorescence time series data belongs to either a neuronal activity process, A, or to an underlying noisy baseline, B. In order to discriminate, with a desired degree of confidence, between these two sources, a data-driven model of B

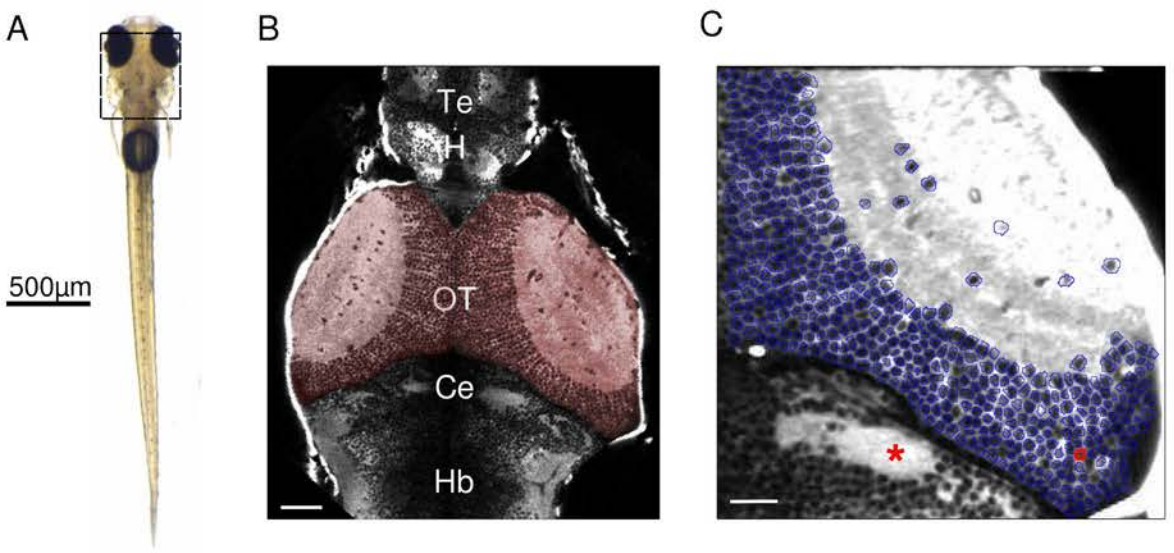

Fig. 2.9 **Neuronal segmentation.** **(A)** Zebrafish larva at 6 dpf, dashed squared region is enlarged in **(B)** Optical section of a larva's brain pan-neuronally expressing GCaMP5G Tg(HuC:GCaMP5G) imaged at ~60um below the skin surface. The OT is highlighted in red. Te, telencephalon, H, habenula; Ce, cerebellum; Hb, hindbrain. Scale bar: 50 μm. **(C)** Typical optical section acquired with the two-photon microscope. The major part of one tectal hemisphere was covered. ROIs corresponding to each single neuron (blue patches) are superimposed with an average image of a ~1h recording. A tdTomato labeled neuron is circled in red. The asterisk denoted the cerebellar commissure used as anatomical reference to minimize inter-recordings variability. Antero-posterior and right-left axes are indicated on the top left corner. Scale bar: 20 μm.

was built, taking into account the biophysical constraints of the fluorescent calcium indicator (GCaMP5G fluorescence decay time constant). Then a Bayesian odds ratio estimation framework was applied. Non-significant portions of the ΔF/F traces were then set equal to 0 in all subsequent analysis.

Raw fluorescence datasets consisted of the fluorescence time series of N neurons sampled at T discrete time points (N x T matrices). In the present work N=∼500 and T=14000. A smooth estimate of the fluorescence baseline for each neuron, the baseline *bfast*, was calculated by computing the 30s long running average of the 8 th percentile of the raw data Dombeck et al. (2007). This estimate reflected fluctuations unrelated to the fast calcium transients evoked by neuronal activity. A second baseline *bslow* was calculated using 100s long running average to remove potential laser power fluctuations. We then subtracted from the raw fluorescence data the sum of previously *b=bfast+bslow* calculated baselines and the result was further divided by the raw fluorescence in order to obtain a rectified estimate of the relative fluorescence change, ΔF/F.

To infer the noise magnitude of process B, the variance of ΔF/F baseline was calculated. A neuron's ΔF/F typically present a positively skewed distribution, an example is showed in **Figure 2.10**. This distribution peaked at a value μ, with a long positive right heavy tail populated by neuronal calcium events. The most frequent value of the time series, μ, represented a constant residual value of ΔF/F ($\mu = 0.23 \pm 0.06$ for a representative dataset) product of an underestimation of B . The ΔF/F time series of each neuron were therefore recalculated after correcting b by the factor (1+μ). Samples represented by the left tail were negative ΔF/F deflections from the baseline produced by B, hence not related to neuronal calcium events. A robust estimate of the standard deviation (s.d.) of B, σ noise , can be obtained if we consider that B is a Gaussian stochastic process, allowing us to fit the left ΔF/F tail with a normal distribution of mean μ and s.d. σ noise . This assumption seemed valid due to the accuracy of the calculated fits (Left tail, Gaussian fit $r_2 = 0.995 \pm 0.002$ for a representative dataset as in **Figure 2.10**).

- Single-neuron ΔF/F time series had diverse amplitude scales and noise levels, as quantified by the distribution of the their s.d., σ , and of σ_{noise} (see **Figure 2.11**). Therefore, in order to unbiasedly compare the dynamics across neurons we needed to adaptively normalize the multivariate dataset to homogenize the variance across the multiple time series. A satisfactory normalization is obtained by dividing each time series by the corresponding σ_{noise}, defining a dimensionless quantity Z n,i that approximates the signal-to-noise ratio of the neuron N at the time sample i. The

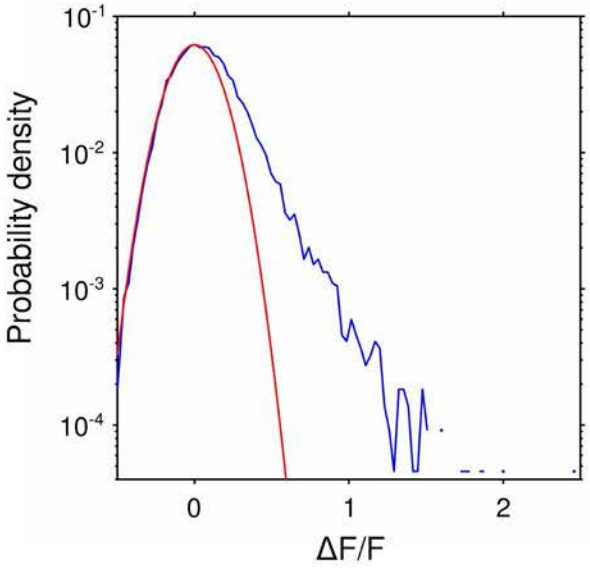

Fig. 2.10 **Probability density of relative fluorescence changes.** Probability density of relative fluorescence changes ($\Delta F/F$) of a typical neuron (blue) and the corresponding Gaussian fit to its negative $\Delta F/F$ values (red), used to estimate the standard deviation (s.d.) of the baseline, B.

$Z_{n,i} \rightarrow Z_{n,i+1}$ transitions between negative values should again be the product of B. Consequently, we used the data belonging to the lower-left quadrant data (see Figure 2.11) to estimate the covariance matrix K of the baseline noise B, and model it as a bivariate Gaussian process with 0 mean and covariance K. The off-diagonal terms of K were negligible (0.03 ± 0.01), suggesting the near-independence of successive realizations of the noise process.

In **Figure 2.11**, the noise model B was compared to the actual data. As expected, a great portion of the $Z_{n,i} \rightarrow Z_{n,i+1}$ transitions between large positive values (upper right quadrant) were not accounted by B, since they corresponded to large positive excursions of the time series that represent the calcium transients of interest. Since any event could only be attributed to A or B, consequently, given a particular $Z_{n,i} \rightarrow Z_{n,i+1}$ transition, the baseline noise posterior probability and the activity posterior probability sum up to one (see Equation 2.1).

$$p(B \mid Z_{n,i}Z_{n,i+1}) + p(A \mid Z_{n,i}Z_{n,i+1}) = 1 \tag{2.1}$$

To assess the source of any $Z_{n,i} \rightarrow Z_{n,i+1}$ transition, we calculated the odds that could belong to B relative to the odds produced by **A**, namely the posterior odds for B against A, which is the ratio between the two terms in Equation 2.1. By forcing a

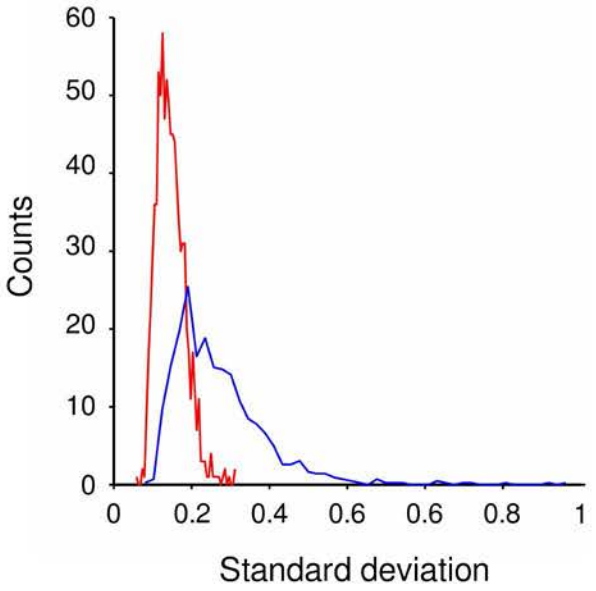

Fig. 2.11 **Fluorescence Noise Model.** Histogram of the ΔF/F s.d. (blue) and the estimated σ noise of one experiment (red).

lower bound to these odds, we could estimate the confidence bound of considering a given $Z_{n,i} \rightarrow Z_{n,i+1}$ transition as a neuronal activity event (see Equation 2.2).

$$\frac{p(B \mid Z_{n,i}Z_{n,i+1})}{p(A \mid Z_{n,i}Z_{n,i+1})} \leqslant \gamma \tag{2.2}$$

Which, using 2.1 reduces to:

$$p(B \mid Z_{n,i}Z_{n,i+1}) \leqslant \frac{1}{1+\gamma^{-1}} \equiv \beta \tag{2.3}$$

In the present work, we chose a β value of 0.05, implying posterior odds of 19:1 against noise ($\gamma^{-1} = 19$) and a confidence of 95% on the classification of the $Z_{n,i} \rightarrow Z_{n,i+1}$ transition as a neuronal activity event. Therefore, we only needed to estimate the leftmost term in equation 2.3, the baseline noise posterior probability. Using Bayes' theorem (equation 2.4), the latter can be decomposed as in Equation 2.5.

$$P(X \mid Y) = \frac{P(X)}{P(Y)} \cdot P(Y \mid X) \tag{2.4}$$

$$p(B \mid Z_{n,i}Z_{n,i+1}) = p(B) \cdot \frac{p(Z_{n,i}Z_{n,i+1} \mid B)}{p(Z_{n,i}Z_{n,i+1})} \tag{2.5}$$

- The first term in right hand side, the prior probability of noise, should be close to one since the calcium transients are relatively rare ($p(B) >> p(A)$). However, its actual numerical value would not change qualitatively the inference procedure since it

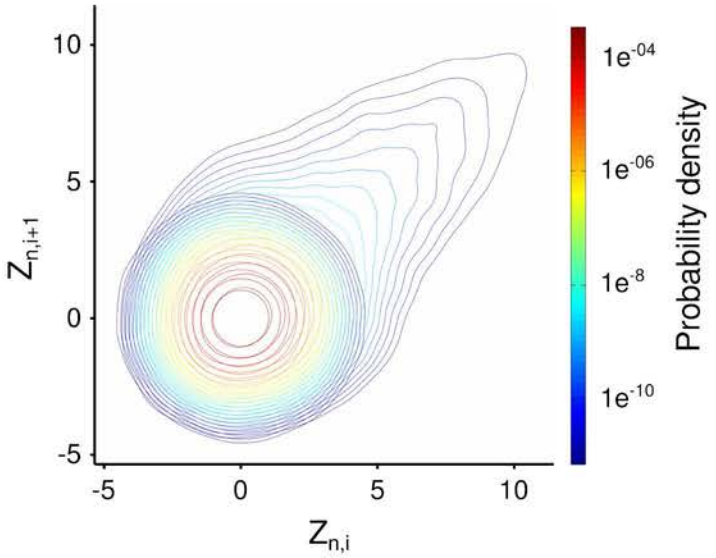

Fig. 2.12 **Probability densities of fluorescence transitions**. The probability densities of the $Z_{n,i} \rightarrow Z_{n,i+1}$ transitions observed in an experiment (positively skewed contour plot) and for the baseline B model (round-shaped contour plot) are overlaid for comparison. The distributions were estimated by a bivariate locally adaptive density estimation procedure. Color-bar: Contour values.

is just an overall scaling factor. The denominator of the second term, the probability density of data transitions, can be estimated directly from the measured dataset. Finally, the numerator of the second term, the probability density of data transitions given the baseline noise process, will be approximated by the already described noise model shown in **Figure 2.12**. The density distributions of the two latter terms were estimated by means of a bivariate locally adaptive density estimation procedure, using the dataset and a realization of the noise model, respectively. With all these variables, we could then infer the posterior odds for B against A for any given $Z_{n,i} \rightarrow Z_{n,i+1}$ transition in the data (see Equation 2.2). In an effort to rule out non-activity- related $Z_{n,i} \rightarrow Z_{n,i+1}$ transitions that cannot be explained by the noise process B (non-gaussian noise most probably arised from the PMTs) we imposed a final biophysical constraint to the inference procedure. This constraint is given by the decay time constant of GCaMP5G (Akerboom et al., 2012), $t_{decay} = 510ms$. The exponential decay of the calcium transients indicated that the relationship between the fluorescence signals of two consecutive imaging frames separated by the inter-frame time interval $\Delta t_{imaging}$ should be bounded by Equation 2.6).

$$e^{\left(\frac{-\Delta t_{imaging}}{\tau_{decay}}\right)}(Z_{n,i} - 1) \leq Z_{n,i+1} + 1 \tag{2.6}$$

- As observed in Equation 2.6, in practice, when setting the threshold we allowed for a noise corruption of value 1 (one σ_{noise}) of each $Z_{n,i}$. These limits impose straight bounds in the amplitudes of $Z_{n,i} \rightarrow Z_{n,i+1}$ transitions. The combination of this time constant bound together with the estimated map of posterior odds results in a range of transitions that both respect the temporal dynamics of GcaMP5G and are inferred to be produced by neuronal activities with at least 95% confidence (see **Figure 2.13**, **Figure 2.14**).

- It is instructive to compare this method of posterior odds thresholding to the popularly used likelihood ratio test, which optimally minimizes an expected loss function of the classification (Neuroscience, 2005). In contrast, the method presented here, essentially puts a limit to the quantity of false positives that we are able to accept (at the expense of possible false negatives). Using the Bayes' theorem (2.4), we expanded posterior odds for **B** against **A**.

$$\frac{p(B \mid Z_{n,i}Z_{n,i+1})}{p(A \mid Z_{n,i}Z_{n,i+1})} = \frac{p(B)}{p(A)} \cdot \frac{p(Z_{n,i}Z_{n,i+1} \mid B)}{p(Z_{n,i}Z_{n,i+1} \mid A)} \tag{2.7}$$

The first term in the right hand side of 2.7 is the *prior odds*, which reflects our *a priori* expectation for the odds without taking into account any particular measurement, and the second is the likelihood *ratio* which modulates the naive prior inference by the ratio of probabilities for a transition given either the A or B process. As mentioned before, the latter term could be used to infer if any given transition is related to neuronal activity by estimating if the corresponding likelihood ratio was below a certain threshold parameter η. However, for this purpose, we should build a model for the A process, which is out of our reach, if possible at all. Anyway, 2.7 indicates that the likelihood ratio and the posterior odds were equal, up to the constant factor prior odds, that does not depend on the measured data. This means that any inference based on the the posterior odds (the current method) is qualitatively similar to the one that could be performed through the likelihood ratio test, albeit an overall scaling factor of the confidence value.

2.3.3 Data Analysis

Pair-wise correlations between neuron's spontaneous activity

Spontaneous correlations were computed by calculating the temporal Pearsons's linear correlation ρ for all neuronal pairs. For a pair of neuron i and j, $\rho_{X,Y}$ was computed using the binarized activity dynamics X and Y as input (0 for non-significative and 1 for significative fluorescence fluctuations). $\rho_{X,Y}$ is the covariance of X and Y divided by

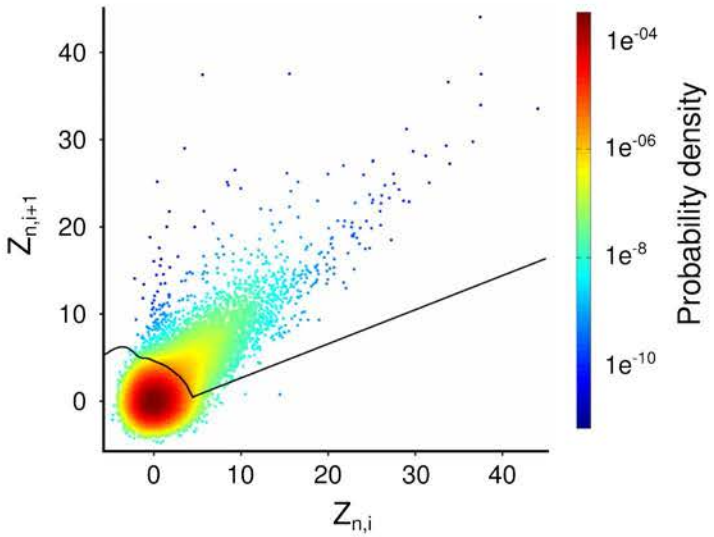

Fig. 2.13 **Scatter plot of fluorescence transitions.** $Z_{n,i} \rightarrow Z_{n,i+1}$ transitions, color-coded according to their probability densities (same experiment as **Figure 2.9**). The range of transitions that were inferred as part of a neuronal calcium transient is outlined by the black curve ($p < 0.05$). This boundary is composed by a straight line that corresponds to the constraint imposed by GCaMP5G decay time constant, and a curved perimeter that is given by the noise model B.

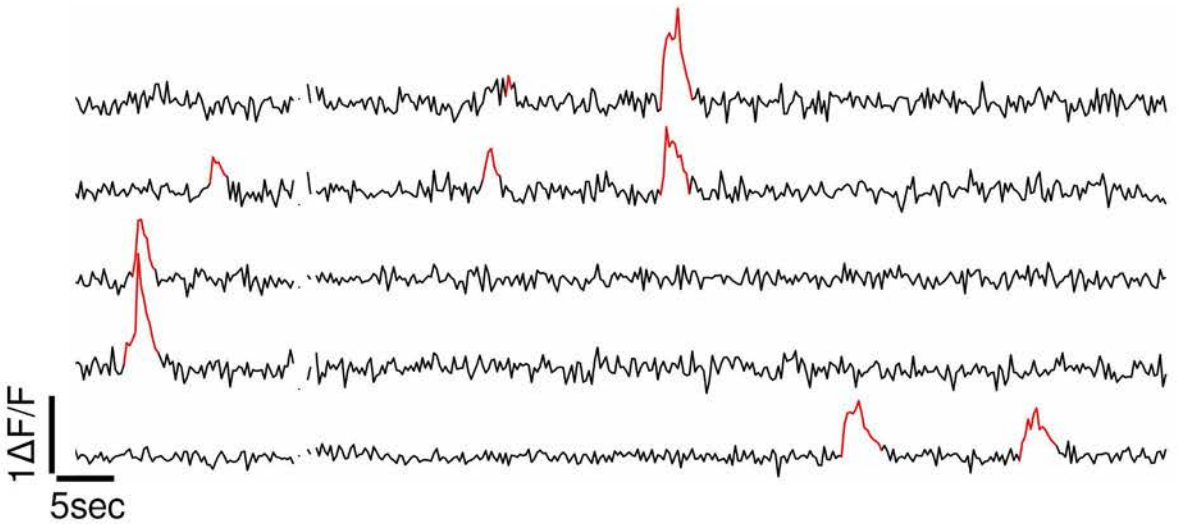

Fig. 2.14 **Neuronal fluorescence traces.** Examples of typical single-neuron $\Delta F/F$ traces (black) with significant fluorescence transients highlighted in red. Breaks in the traces depict discarded frames due to movement artifacts.

the product of their standard deviations. The expression of $\rho_{X,Y}$ is shown in Equation (2.8) where E is the expectation, σ the standard deviation of the neuron's activity along time, X.

$$\rho_{X,Y} = \frac{E[(X - \mu_X)(Y - \mu_Y)]}{\sigma_X \sigma_Y} \tag{2.8}$$

Significant correlations were extracted by thresholding correlation values. The threshold was calculated on a surrogate data set where the spontaneous spike times stamps where shuffled. Correlations between all neuronal pairs were computed using the shuffled surrogate and the *99th* percentile value of the correlations distribution was defined as a threshold. The mean value of the threshold was 0,03±0,01 for n=30 experiments. All correlations greater than the threshold originating from the null model were considered as significant.

To establish the topology of the correlation distribution, the pair-wise cell-to-cell distances from the ROIs' centroids corresponding to each neuron were used (**Figure 2.9**).

To compute the lags during population events. I first extracted significant population events using a threshold based on a null model to discard synchronous events that could be explained by chance. The null model was calculated by shuffling the time stamps of spontaneous calcium events. Population events that contained a number of cells greater than the *95th* percentile value of the distribution arising from the null model were considered as significant. Onsets of spontaneous population events were defined as the times when the number of co-active cells passed the threshold. Offsets of spontaneous population events were defined as the time when the number of co-active cells decreased below the threshold after an onset. The lag for a given cell and for a given event was defined as the duration from onset (**Figure 2.15**).

Clusterization techniques

Hard and *Fuzzy* clustering methods were applied. Matlab built-in functions and a fuzzy clustering toolbox were used (Balasko et al., 2005). To extract mutually exclusive neuronal ensembles from spontaneous activity recording the K-means *hard* clustering algorithm was used. The K-means algorithm aims at partitioning a population of n k_i elements into k clusters in which each element belongs to only one cluster. The aim of this algorithm is to minimize a quantity Θ that quantifies the inner-cluster variability (see Equation 2.9) for the x_i elements classified into the k_i cluster, $\mathfrak{t}_i$ being the mean of elements in cluster k_i.

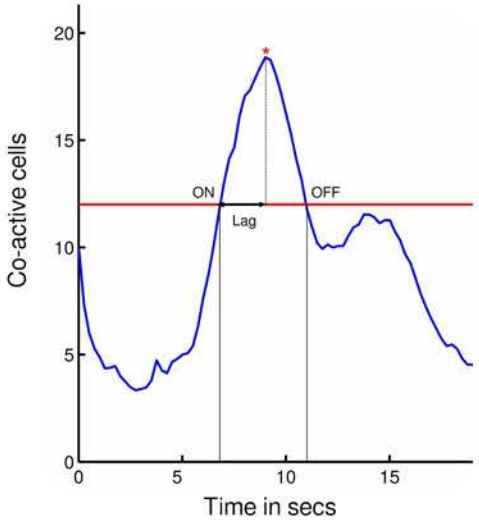

Fig. 2.15 **Spontaneous events onsets, offsets and lag.** Example where the number of co-active cells surpasses the null-model derived threshold (red line). The onset and offsets of the event (ON and OFF, respectively) are defined by the times as which the threshold is crossed. The lag for a cell activated at the time indicated by the asterisk is shown by the black arrow.

$$\Theta = sum_{i=1}^{k} \sum_{\mathbf{x} \in S_i} \|\mathbf{x} - \boldsymbol{\mu}_i\|^2 \tag{2.9}$$

Clusterization was performed with the correlation matrix as an input. The number of clusters was given *a priori* between 2 and 10 and clustering performance was evaluated by computing the silhouette index *s*. The silhouette s_i value for each point i is a measure of how similar a point is to other point in its own cluster, when compared to points in other clusters. The silhouette value for the ith point, s_i, is defined as in Equation 2.10.

$$S(i) = \frac{b(i) - a(i)}{\max\{a(i), b(i)\}} \tag{2.10}$$

S(i) is computed using ai the average distance from the *ith* point to the other points in the same cluster as *i*, and *bi* is the minimum average distance from the *ith* point to point in a different cluster, minimized over clusters. The silhouette value ranges from -1 to 1. A high silhouette value indicates that i is well-matched to its own cluster, and poorly-matched to neighboring clusters. If most points have a high silhouette value, then the clustering solution is appropriate. If many points have a low or negative silhouette value, then the clustering solution may have either too many or too few

clusters. The number of clusters that maximized *Si* values was selected for further analyses.

Conversely, the fuzzy clustering algorithm does not perform a strict partitioning of the data but attributes a membership level for every element of the population to each cluster. Similarly to the K-means algorithm it minimizes a quantity Θ where each element w_{ij} tells the degree to which element x_i belongs to cluster c_j, see Equation 2.11.

$$\Theta = \sum_{i=1}^{n} \sum_{j=1}^{c} w_{ij} \left\| \mathbf{x}_i - \mathbf{c}_j \right\|^2 \tag{2.11}$$

The correlation matrix was transformed into an euclidean distance matrix using non classical 2-dimensional scaling and used as an input for Fuzzy C-means clustering method (**Figure 2.16A-B**). The number of clusters was selected using the Davies-Bouldin index (DBI) to assess clusterization performance by estimating the ratio of within-cluster and between-cluster distances (Balasko et al., 2005). The number of clusters that maximized the DBI was selected further analyses. The distance index from clusters centers was computed as the inverse of the probability of membership of the closest cluster. To exclude inactive neurons or those whose activity was desynchronized with tectal neurons, I using a thresholding method based on the previously described null model used to detect significant pair-wise correlations (see **2.3.3 Pair-wise correlations between neuron's spontaneous activity**). Using a surrogate data set where the spontaneous spike times stamps where shuffled, I computed the number of significantly correlated neurons for each neuron. The *95th* percentile of the distribution was used as a threshold: the mean value of the threshold was 15.6±0.05 neurons for n=30 experiments. Neurons that were significantly correlated with a number of neurons greater than the threshold were considered for further analyses.

Calculation and analysis of the neurons' visual receptive fields

The RF was determined as the region of the field of view within which light-spot stimuli evoked significant calcium responses. The calcium responses were averaged in a 3,75s window from the stimulus onset after subtracting the baseline fluorescence averaged over 1s before stimulation.

RFs were filtered using a correlation based approach to select the most similar trials. Indeed, I observed that 40% of the recorded fish showed habituation to the stimuli, eliciting very few calcium events upon stimulation after 5 trials. To prevent averaging with these poorly informative trials, those that didn't elicit spikes were discarded and

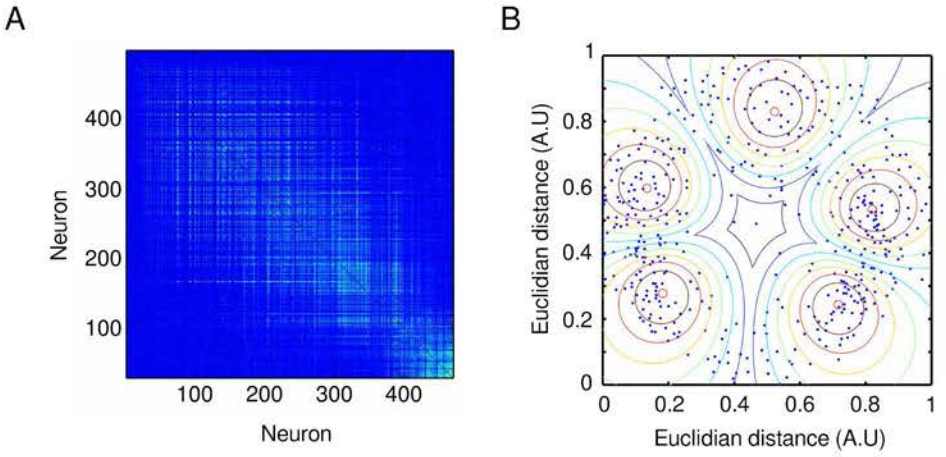

Fig. 2.16 **The fuzzy-clustering method.** **(A)** Example of correlation matrix extracted from spontaneous activity. **(B)** The transformed correlation matrix into euclidean distances in a 2d space. Each blue dot corresponds to a neuron. The curves represent the probability of belonging to each cluster. Red to dark blue curves mark probabilities of cluster membership by 10% decreasing increments.

the pair-wise correlation matrix of all remaining trials was computed. The matrix was summed along one dimension and the 5 trials with the higher value (trials that were the most similar to the others) were kept for further analyzes.

Significantly responsive neurons were selected by extracting the baseline activity during 1s just prior to the stimulus presentation for each stimulus. Distributions medians pre and post-stimuli were compared using a non-parametric Mann-Whitney U-test. Neurons with a p values smaller than 0,01 (that is, those that exhibited consistently increased fluorescence during periods of stimulus presentation compared to the baseline) were considered significantly visually responsive.

To quantify RFs sharpness, mean RFs were fitted with two one-dimensional Gaussian curves by summing mean RFs along the vertical and horizontal axes. The sharpness was calculated as the ratio of the half-maximum amplitude over the geometric mean of the half-widths at half-maximum of the tuning curves along vertical and horizontal dimensions (**Figure 2.17**). Neurons with at least one peak of Gaussian fitted curves that were located outside of the stimulated area were discarded. Also, neurons with $R^2<0.3$ for at least one Gaussian fit were discarded for further analyses. RFs were smoothed by bilinear interpolation.

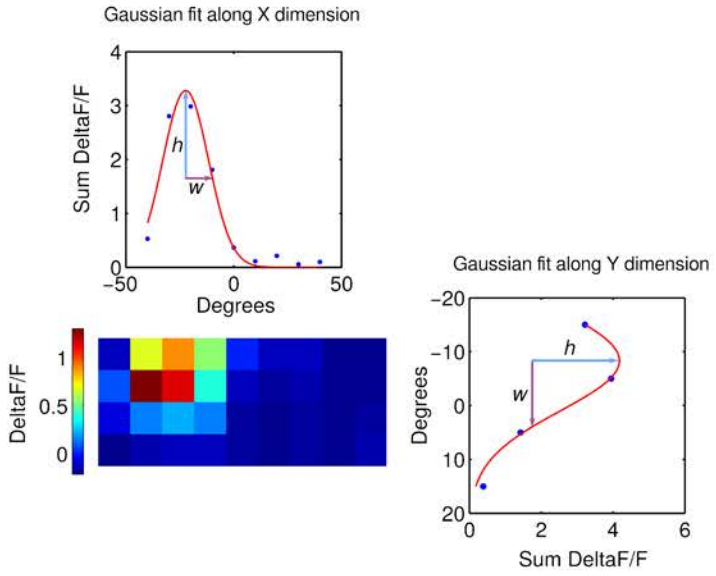

Fig. 2.17 **Gaussian fitting of receptive fields.** Example of one receptive field fitted to two one dimension Gaussian curves along the x and y axis. h and w depict the half-maximum amplitude and the half-width at half-maximum, respectively used for sharpness calculation.

Calculation of direction selectivity

The DS was calculated from the average response to the 4 moving bars presented in the same direction. The calcium responses to each bar were averaged in a 3,75s window from stimulation onset after subtracting the baseline fluorescence averaged over 1s before stimulation. In general, neurons responded to more than one direction. Thus, for each responding neuron, we calculated their left-right and up-down selectivity as the difference of their average neuronal responses to light bars moving in opposite directions, divided by their sum. When this value was bigger/smaller than 0.5/-0.5 the neuron was considered as left/right or up/down DS, respectively (Hunter et al., 2013). The directionality index was computed as the sum of the left/right and up/down DS vectors.

Chapter 3

Results

3.1 Labeling newborn neurons in zebrafish larvae

3.1.1 Low-voltage electroporation labels newborn neurons

To study the morphological and functional neuronal maturation as well as their incorporation into circuits during embryogenesis it is necessary to develop a technique that specifically labels immature neurons during a time window when mature and newborn neurons co-exist. Moreover, this technique has to be minimally invasive, maintaining the integrity of the neuronal circuit in-vivo.

In an attempt to label newborn neurons in the zebrafish OT (**Figure 3.1A-C**), I performed in-vivo electroporation between 4-7 dpf using the following vectors: HuC:Gal4, 2XUAS:tdtomatoCAAX and 2XUAS:transposase. *HuC* is a pan-neuronal promoter that labels neurons very early after differentiation (Kim et al., 1996). I remarked that at low voltage (20V), one short electrical pulse (4ms) labeled a few number of cells (4,1±1,7 cells, n=91 fish) that were located in close vicinity of the caudo-lateral portion of the OT (**Figure 3.1C** and **Figure 3.1D**, asterisk).

Previous studies have shown that this region ensures the teleosts tectal growth from larval stages up to adulthood (Alunni et al., 2010; Recher et al., 2013). Indeed, in the *Tg(HuC:GCaMP5G)* line, a line that expresses GCaMP5G pan-neuronally (**Figure 3.1C**), this region was unlabeled (**Figure 3.1D**, asterisk). In addition, the morphology of the labeled neurons was immature, showing small dendritic arbors compared to the described mature neuronal types at identical stages (see **Figure 3.1D**, **Material and methods** and Nevin et al. (2010)).

To confirm that labeled neurons were located next to proliferation sites in the OT, I crossed *Tg(HuC:GCaMP5G)* with *Tg(EF1α:mAG-zGem)*. The latter expresses a

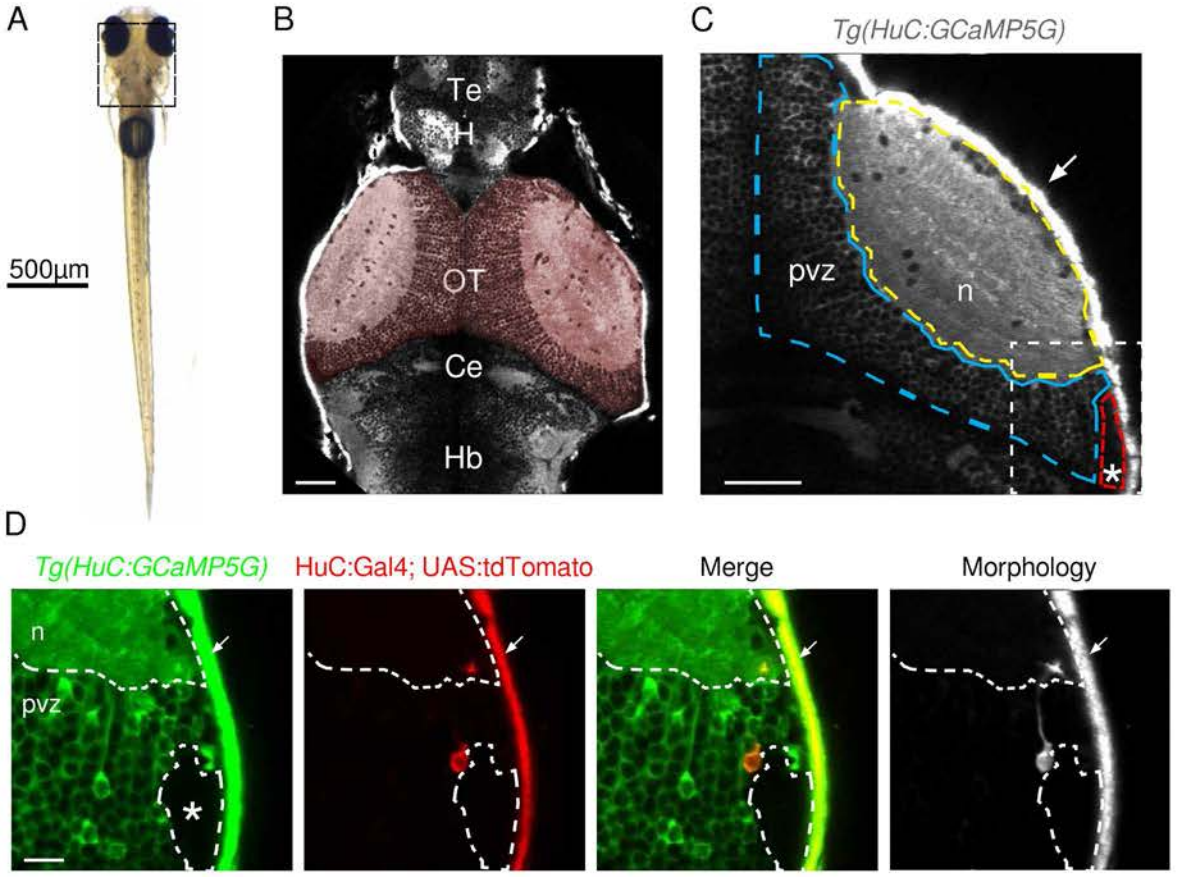

Fig. 3.1 **Position and morphology of electroporated neurons in the optic tectum.** **(A)** Zebrafish larva at 6 dpf, dashed squared region is enlarged in **(B)** Optical section of a larva's brain pan-neuronally expressing GCaMP5G: *Tg(HuC:GCaMP5G)* imaged at ∼60 μm below the skin surface. The OT is highlighted in red. Te, telencephalon, H, habenula; Ce, cerebellum; Hb, hindbrain. Scale bar: 50 μm. **(C)** The right tectal hemisphere of the pan-neuronally expressing GCaMP5G *Tg(HuC:GCaMP5G)*. Ce, cerebellum and imaged at a similar depth. The periventricular zone (pvz) and the neuropil (n) are circled with a blue and yellow dashed lines, respectively. Neurogenesis site is circled with a red dashed line and denoted by an asterisk. Scale bar: 50 μm. The dashed squared region is enlarged in **(D)** tdTomato-labeled periventricular neuron adjacent to the neurogenesis site imaged one day after electroporation. Scale bar: 10 μm Pictures **B-D** were acquired using a two-photon microscope. Arrows denote tectal skin.

green fluorescent protein, Azami green (AG, used because it forms tetramers that are brighter than EGFP) in the nucleus of cells in S/G2/M phases. The cells can be easily differentiated from GCaMP5G expressing cells whose fluorescence is restricted to the cytoplasm. Noticeably, tdTomato-labeled cells using electroporation were adjacent to dividing progenitors one day after electroporation (**Figure 3.2**). These observations suggest that the electroporated-labeled cells are newborn neurons that have recently exited the proliferation zone and differentiated into immature neurons.

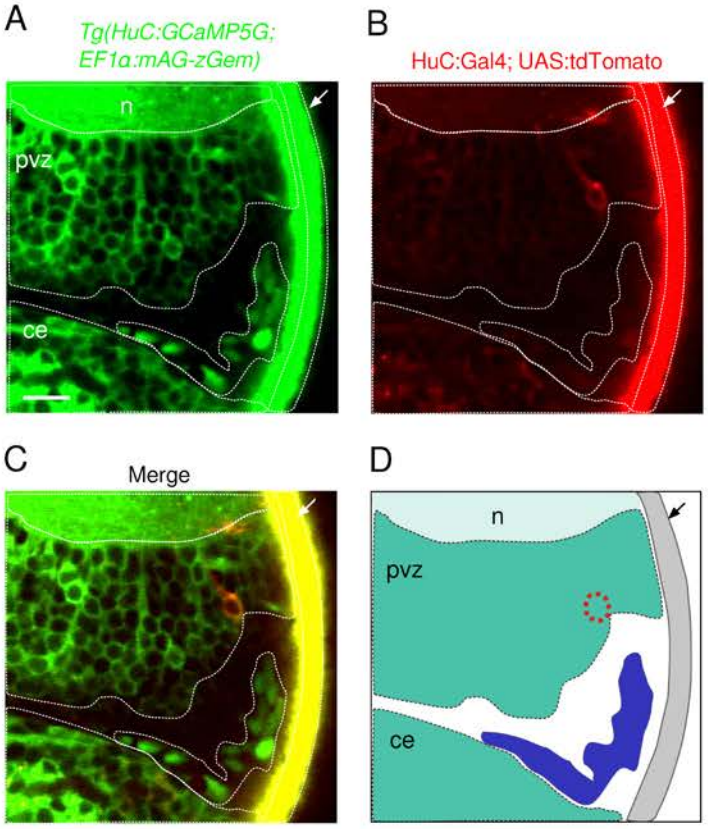

Fig. 3.2 **Labeled neurons neighboring the neurogenic sites in the optic tectum.** Caudo-lateral region of the OT of *Tg(HuC:GCaMP5G; EF1α:mAG-zGem)* electroporated with HuC:Gal4; UAS:tdTomatoCAAX. **(A)** Green channel showing neurons expressing GCaMP5G in the cytoplasm and dividing cells expressing Azami green (AG) in the nucleus. **(B)** Red channel showing a tdTomato labeled cell. **(C)** Merge of the green and red channels. **(D)** Schematic representation of the merged channels: GCaMP5G expressing neurons are represented in cyan and AG expressing cells in blue. Note the gap between the blue and the green tectal area. This area probably comprises cells that are differentiating into neurons, too young to express HuC but too old to express EF1α (after exiting the cell cyle). Scale bar: 10 μm. Skin is indicated by the arrow. Pictures were acquired using a two-photon microscope one day after electroporation. n: neuropil, pvz: periventricular zone, ce: cerebellum.

To study the migration of these newborn neurons, I performed BrdU-pulse-chase experiments followed by immuno-labeling of BrdU-positive cells and PCNA positive proliferation sites of coronal OT sections. I observed that BrdU-positive neurons are found progressively further away from proliferation sites as the delay between the pulse and the fixation increased (**Figure 3.3**). The BrdU-labeled neurons were globally distributed in a front-like manner that advanced radially away from the proliferation site. This observation suggests that newborn neurons are pushed away from the proliferation site by the newly produces neurons, passively colonizing the OT during early larva developmental stages (4-7 dpf). However, few individual cells were found far from the large BrdU population (**Figure 3.3**, t+24h, arrowhead). In contrast to the rest of the population, these cells may displace through active migration or indicate rare radial glia divisions after injury. Taken together, these results suggest that in the OT periventricular zone the majority of newborn neurons are pushed away from proliferation sites and distributed radially through passive displacement. This confirms previous results obtained in the juvenile medaka and in the adult zebrafish OT (Alunni et al., 2010; Zupanc et al., 2005).

To confirm that the labeled cells were newborn neurons, I tested whether they already had a cell identity (exctitatory or inhibitory), one day after the electroporation. In the OT, the large majority of neurons either become glutamatergic or GABAergic (Gabriel et al., 2012; Robles et al., 2011). Therefore, I electroporated the HuC:Gal4 and UAS:tdTomato vectors in transgenic zebrafish expressing GFP under a GABAergic promoter (*Tg(gad1b:GFP)*), and the vectors HuC:Gal4 and UAS:EGFP in transgenic zebrafish expressing DsRed under the control of a glutamatergic promoter (*Tg(vglut2a:loxP-DsRed-loxP-GFP)*). At one day after the electroporation, the labeled newborn neurons were negative for GFP and DsRed respectively (n=6, n=5), indicating that they did not yet acquired their cell identity (**Figure 3.4**).

To conclude, newborn neurons can be sparsely labeled in the zebrafish larva OT, using in vivo electroporation with HuC:Gal4, UAS:tdTomato and UAS:transposase vectors from 4 to 7 dpf. This technique was harmless to the fish and did not impair their survival up to 11 days post fertilization (see **Material and methods**). Moreover, electroporated larvae normally and successfully captured prey. Since they mainly rely on their visual system to hunt (Gahtan et al., 2005), I suggest that the electroporation technique did not perturb the OT functioning and it is therefore well suited to perform morphological and functional imaging of developing tectal newborn neurons.

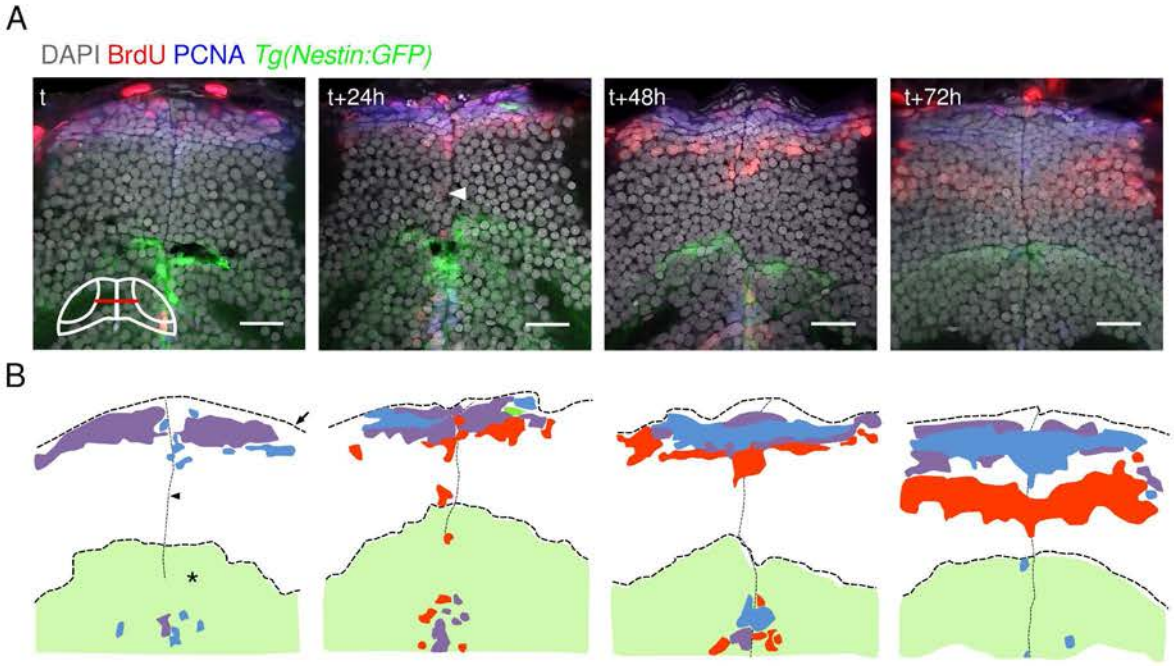

Fig. 3.3 **Newborn cells are pushed away from neurogenic sites.** (A) Representative coronal sections throughout the dorso-medial proliferation zone of the OT from 4 to 7 dpf of *Tg(Nestin:GFP)*. The time between BrdU incubation and subsequent sacrifice is indicated in the left hand corner. Note the global distribution of the BrdU positive cells more and more ventrally in the OT. A few BrdU positive cells were found next to the thalamic surface at t+24h suggesting rapid radial migration (arrowhead). The thalamus is labeled with GFP in *Tg(Nestin:GFP)* and serves as a visual landmark. Images were acquired using a confocal microscope. (B) Schematic representations of the overlying sections. The midline is denoted with an arrowhead, the skin with an arrow and the thalamus with an asterisk. Scale bars: 20 μm.

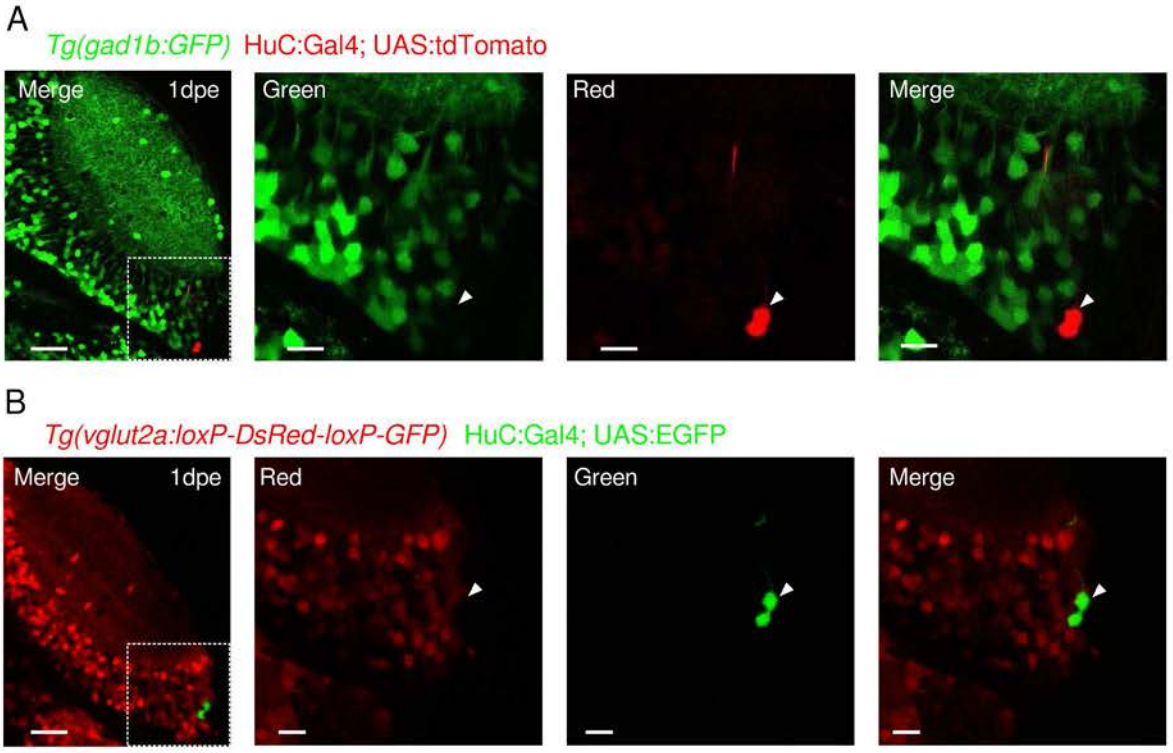

Fig. 3.4 Labeled newborn neurons did not acquire their cell identity. (A) Labeled newborn neurons in *Tg(gad1b:GFP)* using HuC:Gal4 and UAS:tdTomato vectors. Left panel: large view of the tectum, with right panels showing magnified views of the white dashed box area. The labeled neurons positions is indicated with an arrowhead. (B) as in **A**, with labeled newborn neurons in *Tg(vglut2a:loxP-DsRed-loxP-GFP)* using HuC:Gal4 and UAS:EGFP vectors. Scale bar: 20 μm, in insets: 10 μm. Recorded channels are indicated in the pictures. Pictures were acquired using a two-photon microscope one day after electroporation.

3.1.2 Labeled neurons acquire mature neurons' morphology four days after electroporation

Using the electroporation technique at 4 dpf, I could monitor the morphological development of labeled cells from 4 dpe (**Figure 3.5**) and up to 10 dpe (data not shown). Indeed, sparse labeling enabled to chronically monitor the changes in the dendritic arborization. Morphological reconstruction (**Figure 3.6A**) of developing neurons from 1 to 4 dpe showed a *Tg(HuC:GCaMP5G)* ~3 fold increase of the total dendritic growth (total length of 122+/-13 μm to 387+/-80 μm length, n=13 and 10, respectively) (**Figure 3.6B**). Previous studies have estimated the average total dendritic length of mature larval tectal neurons to be ~400 μm (Niell et al., 2004). This suggests that within a period of 4 days of neuronal development, the initially labeled newborn neurons become morphologically indistinguishable from their mature counterparts.

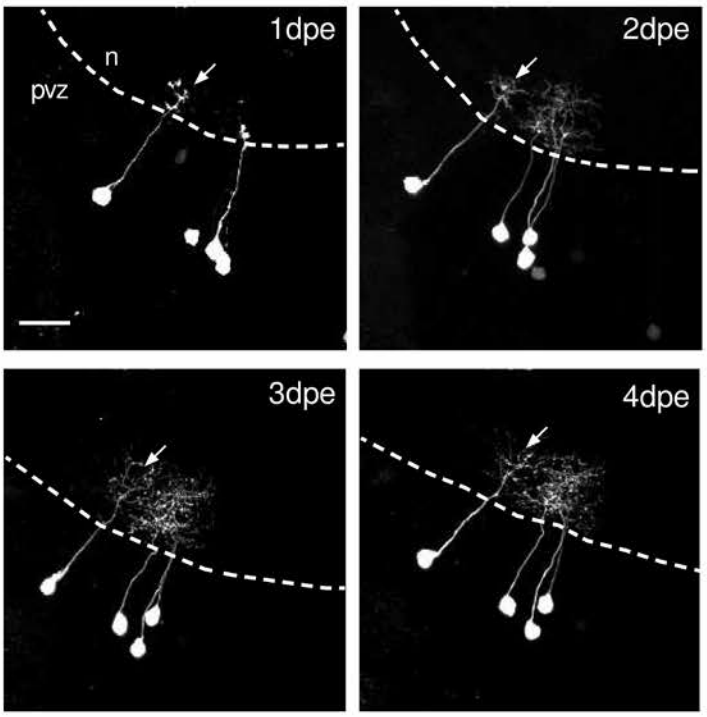

Fig. 3.5 **Morphological development of labeled cells.** Chronic imaging of several newborn neurons after electroporation at 4 dpf. Note that the same neurons can be distinguished from one day to another (example denoted by the arrow). Pvz: peri-ventricular zone, n: neuropil, dpe: days post electroporation. Scale bar: 10 μm. Pictures were acquired as stacks using a two-photon microscope. Note that for morphology reconstruction, I only used labeled neurons without showing overlap with any other labeled one.

At 4 dpe, the labeled neurons could be classified into neuronal subtypes according to their dendritic morphology. Most of the labeled neurons (86%, n=37) became non-stratified periventricular neurons (nsPVIN), while the rest became periventricular projection neurons (PVPN) (**Figure 3.7A** and **Figure 3.5**). At this stage matured neurons laminated in neuropil layers receiving retinal inputs: SGC, between the SAC and the PVZ and in some cases in the SFGS. Matured neurons also arborized in layers comprising tectal recurrent dendro-dentritic connections (SAC and between SGC and SFGS) (**Figure 3.7B**). This observation suggests that mature labeled neurons receive retinal inputs but also are connected to local tectal circuits at 4 dpe.

To conclude, the developed electroporation technique labels a majority of non-stratified periventricular interneurons whose development can be followed up to a morphologically mature state reached at 4 dpe. Using this technique I studied the functional development of these cells by performing recordings of both their spontaneous and visually induced activities.

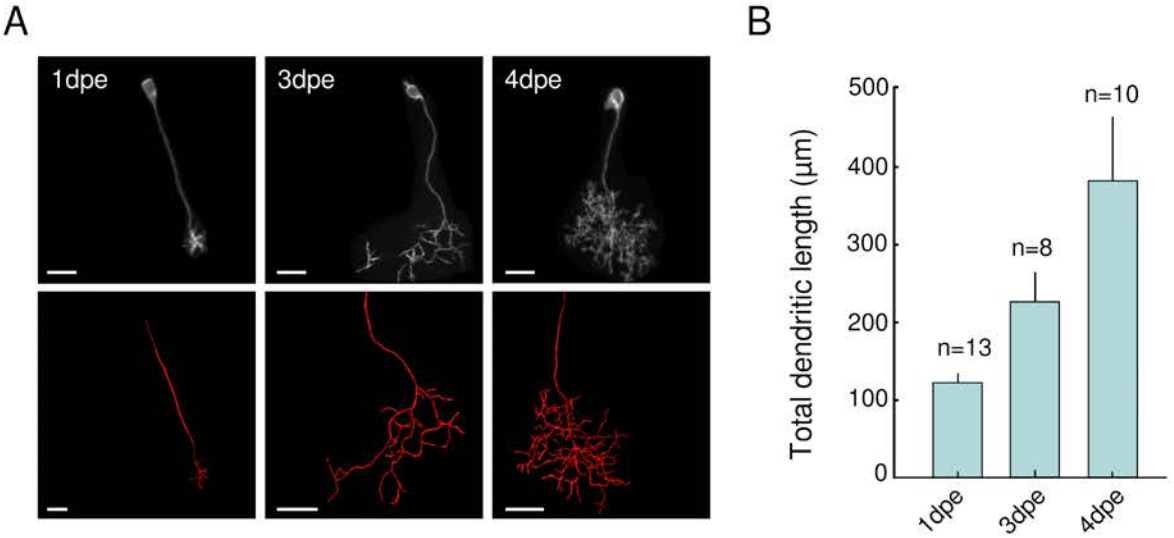

Fig. 3.6 **Evolution of morphological complexity.** **(A)** Example of neuronal reconstructionq at 3 different time points. Scale bar: 10 μm. **(B)** Quantification of the total dendritic length from 1 to 4 dpe.

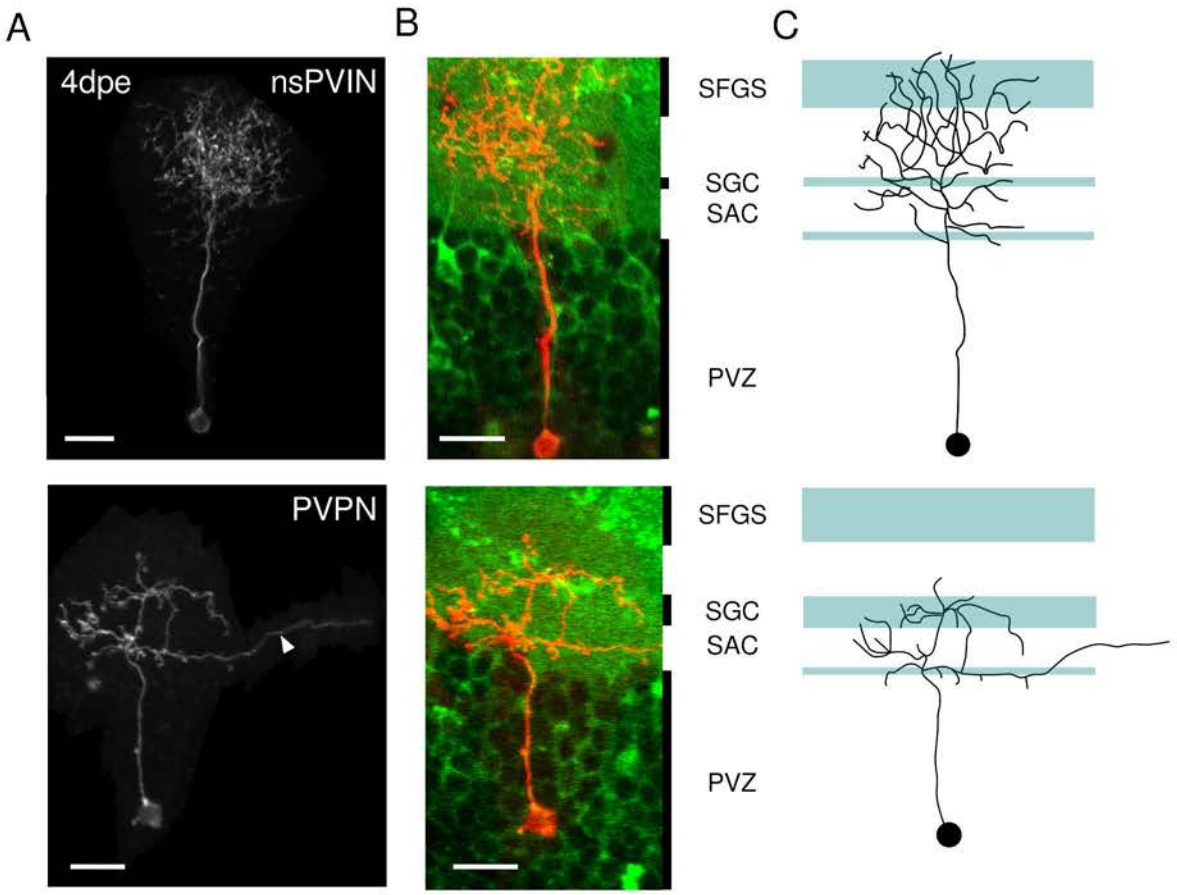

Fig. 3.7 **Electroporation labels a majority of non-stratified periventricular interneurons.** **(A)** Examples of labeled neurons at 4 dpe. Top, the majority of the labeled neurons were nsPVIN. Bottom, In some instances, electroporation also labeled PVPN. Note the long process indicated with an arrowhead. Scale bar 20 μm. Pictures were acquired as stacks using a two-photon microscope. **(B)** Overlay of the morphology of neurons in **A** (red) overlaid on the GCaMP5G expression (green). The latter enables to detect the RGCs laminae denoted on the right (white/black bars). Scale bar: 10 μm **(C)** Schematic representation of a nsPVIN (top) and a PVPN (bottom) neuron . The retinal arborization laminae are indicated in light blue. SFGS: stratum fibrosum et griseum superficiale, SGC: stratum griseum centrale, SAC: stratum album centrale, PVZ: periventricular zone. Note the similarity between the morphology laminar projection of the labeled neurons **B** and the schematic representation of two well-known neuronal subtypes of the OT (See **Introduction** and **Figure 1.16**).

3.2 Functional maturation of labeled newborn neurons

3.2.1 Developing newborn neurons show synchronous activity with local neuronal ensembles

The ongoing spontaneous activity has traditionally been considered as biophysical noise devoid of functional significance (Shadlen and Newsome, 1998). However, recent results have revealed that spontaneous activity is spatiotemporally structured and can revel inter-regional brain connectivity in mice (Mohajerani et al., 2013) and humans (Fox et al., 2005; Raichle et al., 2001). Spontaneous activity seems also to recruit neurons with similar visually induced responses (Miller et al., 2014; Romano et al., 2015) that have been demonstrated to be preferentially synaptically connected (Ko et al., 2013) or electrically coupled (Yu et al., 2012).

In the zebrafish OT, groups of near-by neurons show spontaneous activity correlations (Romano et al., 2015). These ensembles comprise neurons with similar RFs whose synchronous activity represents ∼80% of the significant neuronal pair-wise correlations observed in the tectal population. Furthermore, some of these spontaneous neuronal assemblies features match those observed during prey-capture behaviors, and some of the assemblies are predictive of directional self-generated tail movements. The functional neuronal assemblies showed attractor-like dynamics and emerged even in the absence of their main sensory input (retina), suggesting that they represent the tectum's recurrent connectivity (Akerman and Cline, 2006; Romano et al., 2015). However, how such network properties are acquired during development and how newborn neurons incorporate into these sensory-motor relevant assemblies remains unexplored.

To address this open question, I performed two-photon calcium imaging of HuC:Gal4, UAS:tdTomatoCAAX and UAS:Transposase electroporated *Tg(HuC-GCaMP5G)* larvae at 4 dpf. This method enable me to label newborn neurons (red) and simultaneously monitor their developing spontaneous activity and that of the mature surrounding neurons (∼500 neurons, green), for 4 consecutive days (5, 6, 7 and 8 dpf). Recordings were not chronic but performed in different labeled neurons sampled from 1-4 dpe (**Figure 3.8**).

Previous studies have demonstrated that at 5 dpf, the larva is capable of performing tectum-dependent complex behaviors such as prey capture (Orger et al., 2009). Indeed, from 5 dpf yolk reserves are exhausted and the fish critically needs to feed (**Figure**

3.8). Therefore, although still in development the OT is already matured enough to permit sensory motor transformations underlying visually guided behaviors.

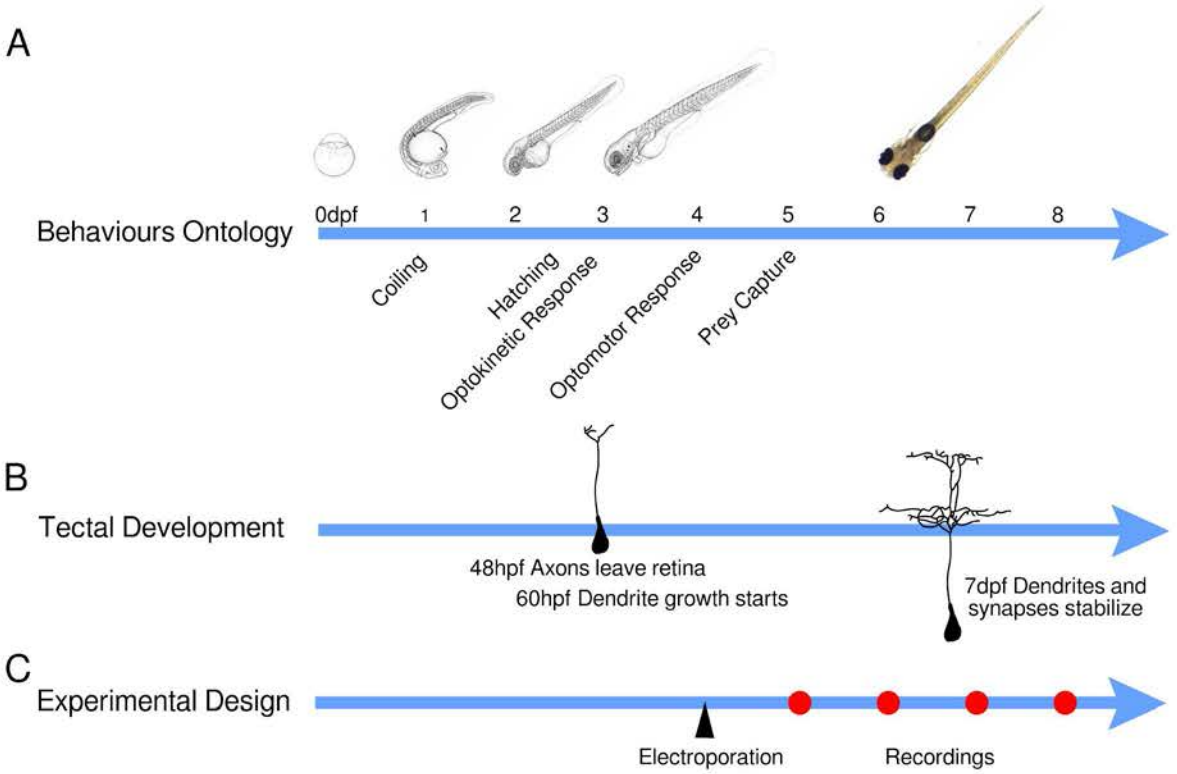

Fig. 3.8 **Timescale of behavior ontology, tectal development and experimental procedure.** **(A)** Early larval development and ontology of classically studied behaviors. Black and white images are reproduced from Kimmel et al. (1995). The first visually induced behaviors emerged at 3 dpf (optokinetic response) although the visual system is not yet fully developed. **(B)** Summary of tectal neurons' morphological development. At 60 hpf, tectal neurons start to develop reaching their final morphology at ~7 dpf although stable matured morphology is not required for generating complex visually induced behaviors. **(C)** To explore the functional maturation of newborn neurons, I performed electroporations of 4 dpf larva and monitored the activity of newborn and mature neurons from 5 to 8 dpf.

I first studied the dynamics of the spontaneous activity in the mature OT as a template to which I could then compare the spontaneous dynamics of newborn neurons. For this purpose, I analyzed the activity of mature neuronal populations for periods of 1h , in the absence of sensory stimulation, at 5 dpf (n=6 fish, p=2336 cells recorded in total). Neuronal populations showed sparse low-frequency basal activity (0.011±0.005Hz, at 5 dpf, see **Figure 3.9A** and **Figure 3.10C**).

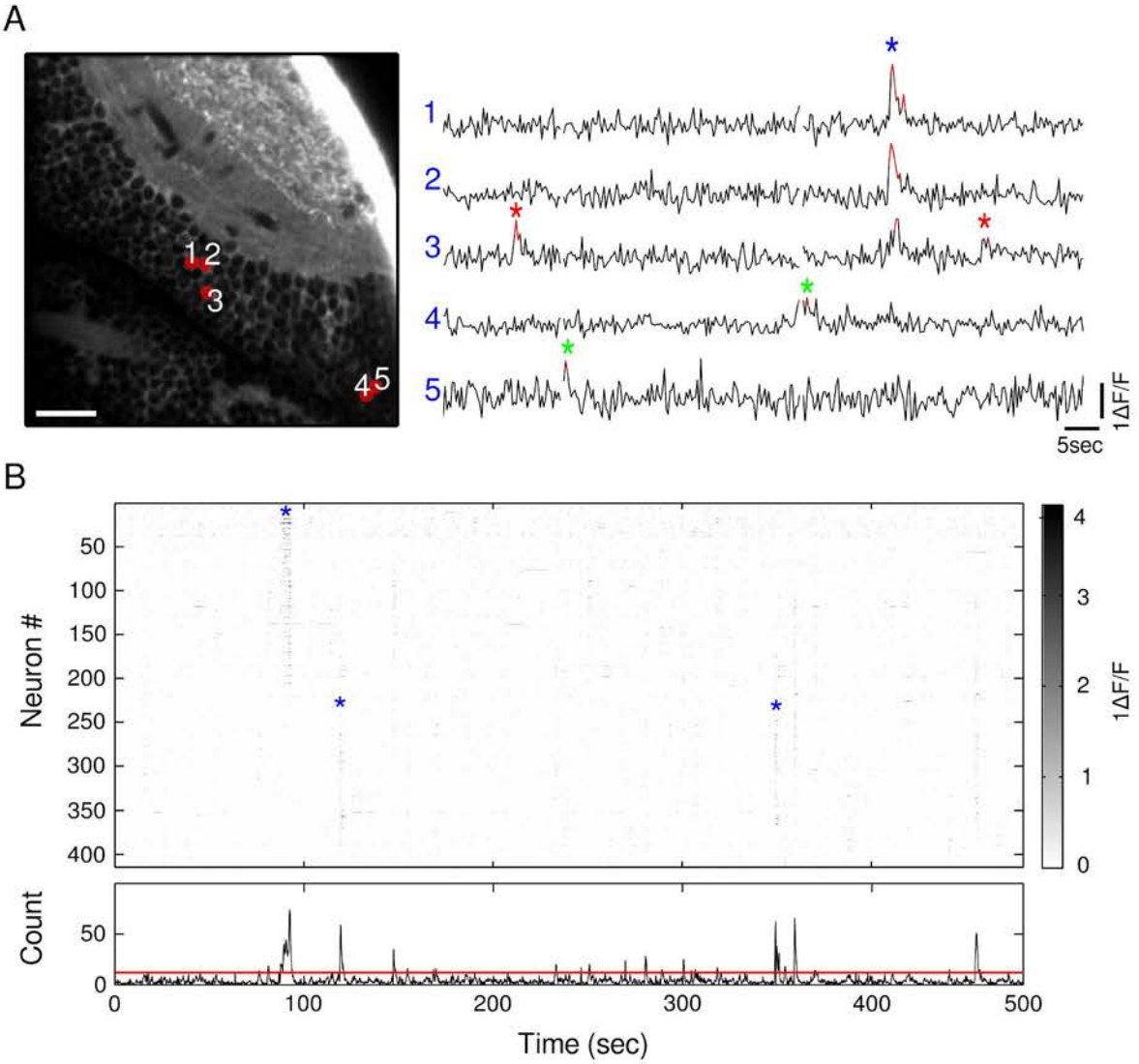

Fig. 3.9 **Spontaneous dynamics of the optic tectum at 5 dpf. (A)** Examples of spontaneously active tectal cells. Left panel: position of the cells in the OT. Scale bar: 20 μm. Right panel: corresponding traces of the fluorescence changes, during a representative recording sample of 1.5 min. Overlaid red traces indicate significant calcium events. Blue asterisks represent synchronous events observed among neighboring cells (neurons 1-3). Note that neuron 3 was not always co-activated with neurons 1-2: red asterisks. Note the poor synchronization of cells located next to neurogenic sites (neurons 4-5): green asterisks. **(B)** Typical raster plot of spontaneous Ca^{2+} transients, revealing episodes of synchronous activations, examples are denoted with asterisks. Grayscale: $\Delta F/F$ amplitude. Bottom: histogram of the Ca^{2+} transients. The red line marks the threshold for significant population events.

Synchronous activity events comprising neighboring neurons were observed (**Figure 3.9A**, see neurons 1, 2, 3, blue asterisk). Episodes of synchronous activations across neurons involved 2%–15% of the total population (**Figure 3.9B**, asterisks). Similar results were obtained for older larvae (6-8 dpf) (data not shown).

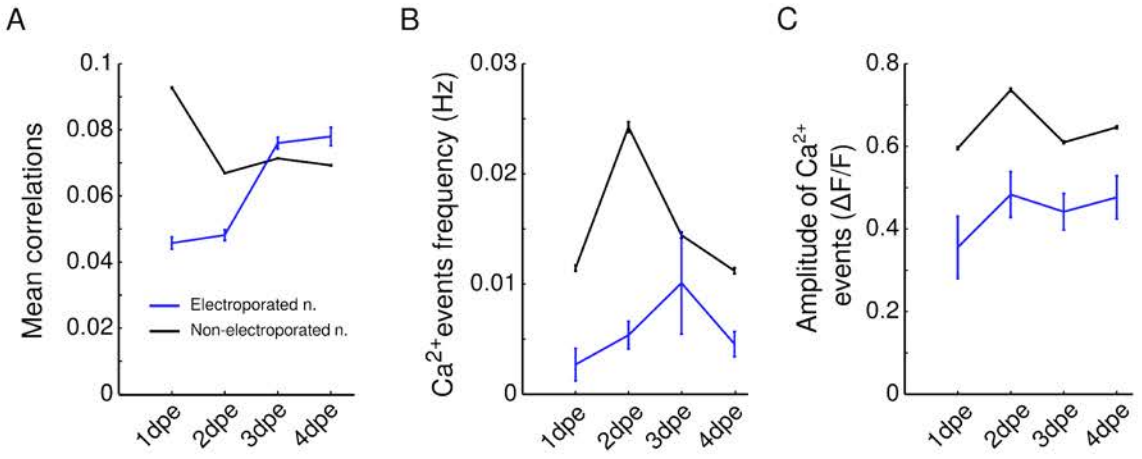

Fig. 3.10 **Spontaneous correlations between newborn neurons and the mature tectal population. (A)** Evolution of mean temporal correlation for unlabeled (UN, black line) and labeled neurons (LN, blue line). **(B)** Evolution of the frequency of Ca^{2+} events. **(C)** Evolution of the amplitude of Ca^{2+} events. Error bars: SEM.

Neurons located next to neurogenic sites (**Figure 3.9A**, see neurons 4 and 5) showed spontaneous calcium events (0.0027±0.0015Hz at 1 dpe: 9.7±5.4 events/1h recording). However, they displayed poor synchrony with their mature surrounding neighbors. To test whether this property was a representative feature of newborn neurons I quantified the average correlations of the labeled neurons with the rest of the tectal population from 1 to 4 dpe (n=6, 5, 12 and 6 labeled neurons, respectively). Average correlations were significantly lower in 1 dpe and 2 dpe labeled-newborn neurons compared to the mature population recorded in the same fish (p=4.8∗10^{-4} and p=2.5∗10^{-30}, respectively, Mann-Whitney U-test). However, at 3 dpe, newborn neurons displayed more similar levels of correlations compared to the mature tectal cells (**Figure 3.10A**) (p=0.023 Mann-Whitney U-test) and became more correlated at 4 dpe (p=3.9∗10^{-5}, Mann-Whitney U-test).

Between 1 and 4 dpe the frequency of the Ca^{2+} events remained non-statistically different for labeled neurons (p=0.19, Kruskal-Wallis test) (**Figure 3.10B**). These results suggest that intrinsic neuronal activity emerges very early in the development of newborn neurons while their functional connectivity and integration into the mature tectal network matures progressively.

Interestingly, the frequency of events and their amplitude was consistently lower in developing cells ($p<0.05$, labeled vs. unlabeled at all stages, Mann-Whitney U-test). This result might be explained by the fact that tdTomato expression impeded the detection of low-magnitude Ca^{2+} events (due to quenching and/or cross talk between channels). This could be also explained by the observed electroporation bias towards only two neuronal subtypes (**Figure 3.7**, nsPVIN and PVPN spontaneous activity events could have lower frequencies and smaller amplitudes in comparison to the average tectal neuron).

To gain further insights on the development of the spontaneous activity of newborn neurons, I explored the spatial structure of the spontaneous correlations between the newborn and the surrounding mature neurons. For that purpose, I first extracted the physical distances between the neurons to compute the distance to correlation relationship at all recorded time-points (1, 2, 3 and 4 dpe). Second, I extracted significant correlations using a null-model based threshold. The threshold was calculated on a surrogate data set where the spontaneous spike times stamps where shuffled. Correlations between all neuronal pairs were computed using the shuffled surrogate and the *99th* percentile value of the correlations distribution was defined as a threshold (threshold for significance values was 0,03±0,01). Non-significant correlations were discarded for further analyses.

At 1 dpe, newborn neurons showed almost no significant correlations with their tectal mature counterparts (9.6 significantly correlated neurons per labeled neuron at 1 dpe and 38.8, 156 and 66 at 2, 3 and 4 dpe, respectively). At 1 dpe, these few and weak correlations (0.0433±0.0021, **Figure 3.10A**) were distributed homogeneously along all distances. At 2 to 3 dpe, significant correlations were found from 0 to 80 μm although strong correlations were mostly clustered at short distances. At 4 dpe, the tendency was accentuated such that significant correlations were found almost exclusively at short distances (**Figure 3.11A** and **Figure 3.11B**).

To compare the distance/correlation relationship between different time points and between the mature and the newborn developing neurons, I computed the proportion of significant correlations for the different physical distances between neurons (within distance bins of 10 μm). As suggested by previous results, at 1 dpe, only 1.6% of all pair-wise correlations were significant, suggesting that at this stage, newborn neurons are not yet connected to the local circuitry (**Figure 3.12**). From 2 to 3 dpe, the proportion of significant correlations increased from 10.7% to 20.3% with the majority of the correlations being found within 30 μm distance from the developing newborn neurons (66,2% at 2 dpe and 72,2% at 3 dpe). At 4 dpe 14.2% of all pairwise correlations

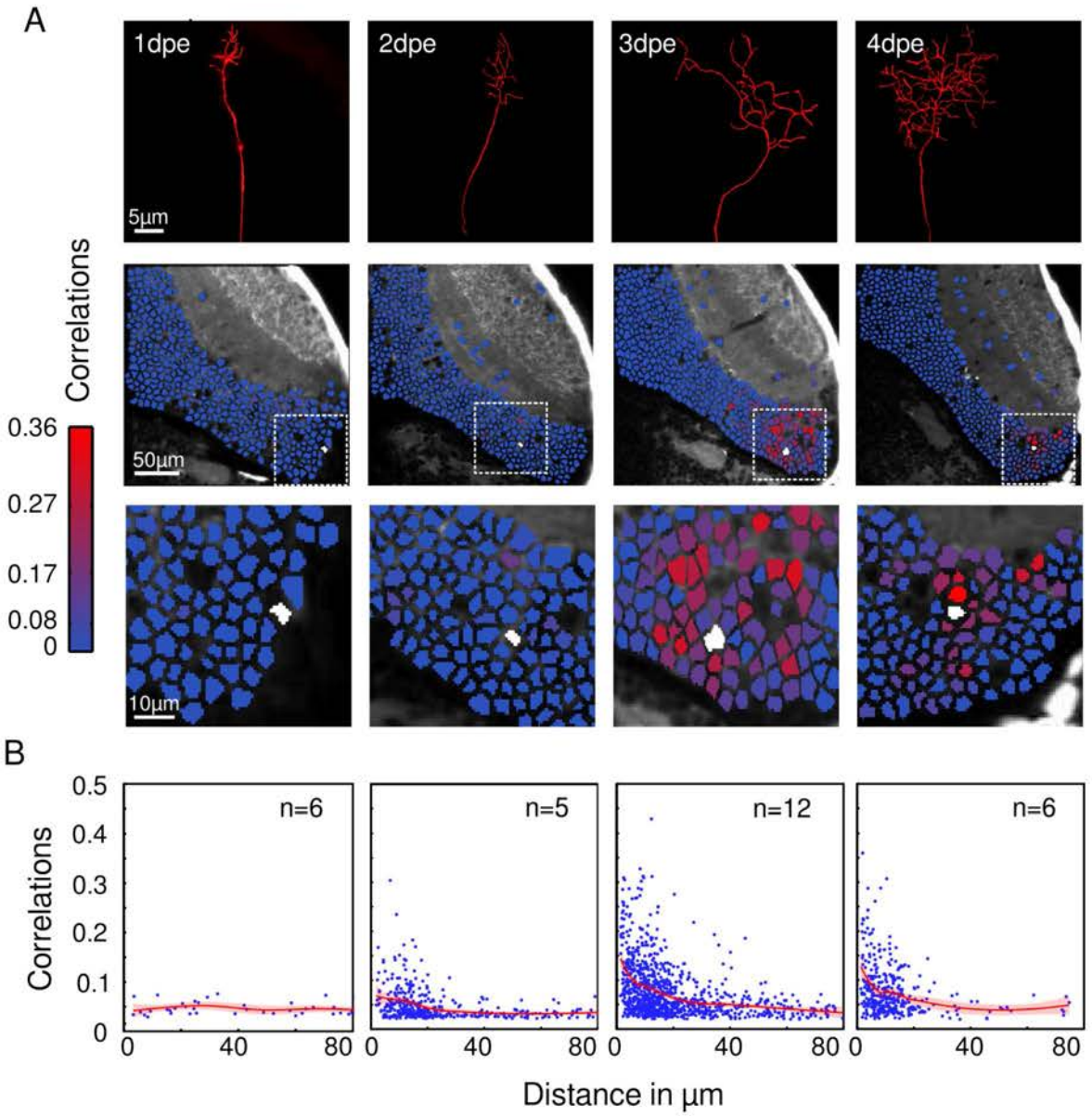

Fig. 3.11 **Development of the spontaneous spatial structure of the newborn neurons.** **(A)** Representative examples of the development of labeled newborn neurons spontaneous activity spatial from 1 to 4 dpe. Top panels: reconstructed morphology of different developing labeled neurons whose correlations with other tectal neurons are shown below (middle panel). Middle panels: Optical plane of the imaged neurons. Neurons are color-coded according to their pair-wise correlation values with the labeled neuron. Color scale: correlation values. The electroporated neuron is labeled in white. Bottom panels: Zoomed image of the white dashed area in middle panels. **(B)** The relationship between the physical distance between the labeled and the mature neurons, and their correlations, for each developing stage (1-4 dpe). Red line: local regression of the correlation values against the corresponding distance. Red patch: interpolation confidence interval. n indicates the number of experiments pooled for each day.

were significant and 88.7% of these significant correlations were concentrated within 30 μm from the newborn-cell soma. In the OT of the larva, the average size of a neuron is ~4,6 μm (Li et al., 2012a), therefore during development nsPVIN and PVPN become correlated with neighboring cells that are mostly found at ~6 somas distance. This suggest that at 4 dpe, matured newborn neurons form local sub-circuits with their mature counterparts.

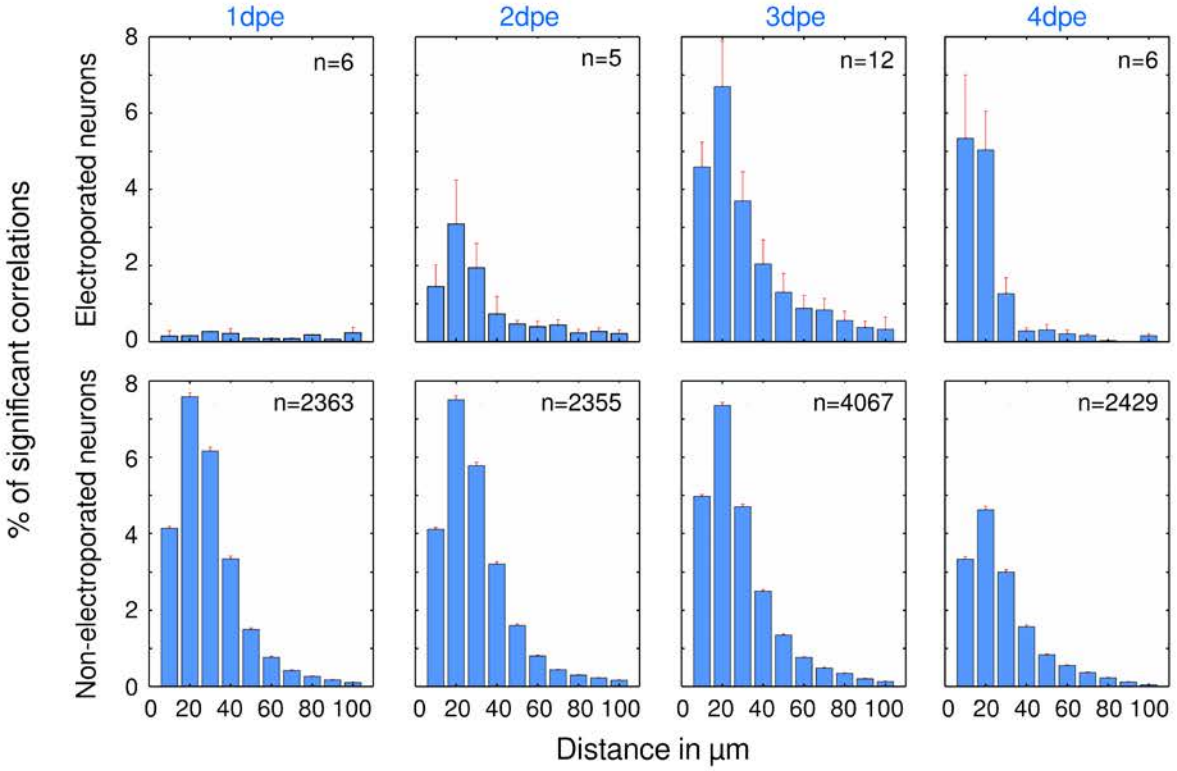

Fig. 3.12 **Distribution of significant correlations along the physical distance between neurons.** Upper panels: Evolution of the distributions of the significant correlations between the labeled neurons with the rest of the tectal network, along the different distances between them. Lower panels: for the mature neurons only. The distributions were calculated for 1,2, 3 and 4 dpe. Error bars represent SEM. The number of cells used to compute the distributions are indicated in right hand corners (n). Note how the distributions of the newborn neurons (top panels) progressively resemble those of mature neurons (bottom panels).

In contrast to the distributions for the newborn neurons, the distribution of distances for significant correlations for mature tectal neurons remained similar from 1 to 3 dpe (see **Table 3.1** for skewness at each stage). However, at 4 dpe we observed a significant decrease of the significant correlations (from 20.2% at 3 dpe to 14.2% at 4 dpe). Yet,

Table 3.1 **Skewness of distances distribution for significant correlations**. Distributions from **Figure 3.12** were used, both for labeled and unlabeled neurons.

	1 dpe	2 dpe	3 dpe	4 dpe
Labeled neurons	0.32	1.32	1.13	1.42
Unlabeled neurons	0.77	0.84	0.93	0.86

Table 3.2 ***p*-values obtained by comparison of distances distribution for significant correlations between labeled and unlabeled neurons**, Mann-Whitney U-test.

	1 dpe	2 dpe	3 dpe	4 dpe
Labeled neurons vs. unlabeled neurons	$9.29*10^{-8}$	0.0026	0.52	$8.84*10^{-25}$

the distributions' skewness remained similar (0.93 at 3 dpe and 0.86 at 4 dpe, see **Table 3.1**).

Interestingly, the correlation to distance distribution of the newborn cells was non-significantly different to the simultaneously recorded mature population at 3 dpe (Mann-Whitney U-test, p=0.51, and see **Table 3.2**). This indicates that at this stage, the spontaneous activity spatial structure of the newborn neurons is similar to that of the mature tectal population.

To further explore the activity temporal dynamics of developing neurons I measured the lag between spontaneous events of each tectal neuron with respect to significant spontaneous population events. The latter were defined as containing a number of co-active cells that could not be explained by chance (null models, see **Material and methods**).

I observed that neurons located nearby neurogenesis sites (**Figure 3.1** and **Figure 3.2**) displayed longer lags to population onsets than those situated away from the neurogenesis sites (**Figure 3.13A**). Then, I calculated the lag between the spontaneous activation of newborn neurons with respect to the peak of the significant spontaneous population events (see Material and methods), at the different developmental stages (1-4 dpe). At 1 dpe, the lag could not be computed since newborn neurons were not synchronized with neighboring neurons (**Figure 3.9-3.11**) and thus not co-activated with significantly large neuronal groups (groups whose co-activation could not be explained by chance) (**Figure 3.13B**).

At 2 dpe their lag showed larger values than the mean population (1.4±0.32s in electroporated neurons and 1.21±0.02s in non-electroporated neurons, **Figure 3.13**).

By 3 dpe, the lag significantly decreased becoming closer to the one of the population (1.12 and 1.25±0.12s for unlabeled and labeled neurons, respectively, p-value=0.14, Man-Whitney U-test)) (**Figure 3.13B**). At 4 dpe, the lag further decreased, becoming smaller than that of the population (1.09±0.01 and 0.77±0.19s for unlabeled and labeled neurons, respectively, Man-Whitney U-test, p-value=0.04).

These results suggest that during the development of newborn neurons, this first act as followers of the mature neurons within the sub-circuit they incorporated to. Upon further maturation, newborn neurons are active synchronously with the population and even acquire the capability to trigger population events, becoming leaders.

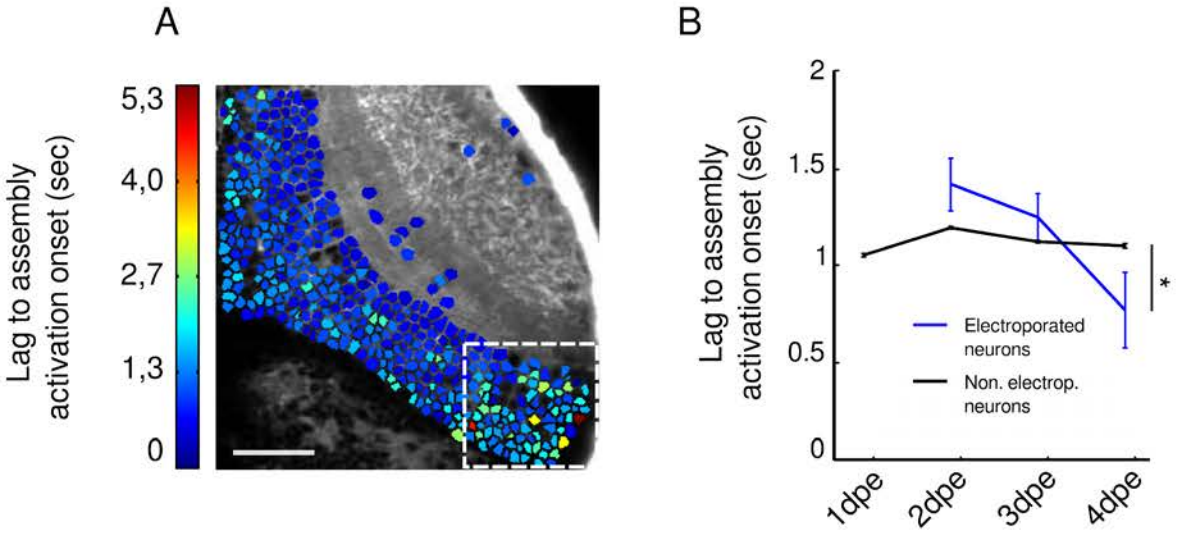

Fig. 3.13 **Newborn neurons' development is associated with a reduction of their lag to spontaneous population events.** **(A)** Optical section of the imaged OT. The neurons are color-coded according to the average lag to spontaneous population events. Note the increased density of neurons with high lag in the white dashed square neighboring the neurogenesis region. Scale bar: 50 μm. Colorbar: lags values in secs. **(B)** The developmental dynamics of the average lag for developing newborn neurons (blue) and their mature counterparts (black). * indicate p<0.05. Error bar represents SEM.

3.2.2 Newborn developing neurons incorporate into mature neuronal assemblies

To study whether newborn neurons incorporate into already established neuronal assemblies I used the K-means algorithm to clusterize the pair-wise correlation matrices of the mature tectal neurons. The hard-clustering K-means algorithm was implemented after determining the ideal number of clusters minimizing intra-cluster variance and

maximizing inter-clusters variance (see **Material and methods**, silhouette index). The algorithm enabled partitioning of the correlation matrix by isolating mutually exclusive co-varying neuronal populations (**Figure 3.14A**). Clusters intra-correlations were tested for statistical significance using shuffled surrogate clusters of identical sizes (null models, see **Material and methods**).

The topographic representation of the different clusters showed covarying neurons locally organized (neuronal assemblies, Romano et al. (2015)). Moreover, these spontaneous assemblies were organized in a retinotopic-like manner as previously observed by Romano et al. (2015) (**Figure 3.14B**).

Then, I asked whether and when newborn neurons incorporate into such spontaneous neuronal assemblies. For this purpose, I quantified the proportion of neurons belonging to spontaneous mature assemblies and observed a rise from 0-11% at 1-2 dpe to 60-86% at 3-4 dpe (see examples in **Figure 3.14B** and population analysis in **Table 3.3**). Therefore, newborn neurons were mainly excluded from neuronal assemblies during their early development (1-2 dpe) but incorporated later to already established ones at 3-4 dpe.

The K-means hard-clustering algorithm is not compatible with situations in which certain elements could belong to several clusters (as overlaping neuronal assemblies, (Romano et al., 2015), thus this technique excluded some neurons from significant clusters and could not represent the overlap between the neuronal assemblies. To solve this issue, I applied a fuzzy clusterization technique to attribute to each neuron a probability of membership to each cluster. As for K-means, the number of clusters was optimized using simultaneous analysis of intra-clusters and inter-clusters variance (See **Material and methods** for the Davies-Bouldin index). To represent the topographic distribution of the fuzzy clusters, I randomly attributed a color to each cluster and color coded each cell by weighting the clusters' colors according to their membership probabilities.

Using this clustering method I obtained a similar retinotopic-like organization as observed for the K-means clusterization (**Figure 3.15A**). Moreover, the fuzzy-clustering technique enables visualizing the overlap between neuronal assemblies at their frontiers (neurons situated in an area close to two assemblies have similar probabilities to belong to one or the other assembly: see **Figure 3.15A**). Interestingly, neurons located next to the tectal neurogenesis niche showed probabilities of belonging to several clusters rather to a given local one (note the mixed colors among neighboring neurons, **Figure 3.15A**, white dashed square and **Figure 3.15A**, right panel). To quantify the development of the organization of neurons within assemblies. I calculated a distance

index (Arbitrary units, AU), which reflects the similarity to the center of each cluster for electroporated and non-electroporated neurons. Inactive or low-correlated neurons during the recorded period were discarded (see **Material and Methods**).

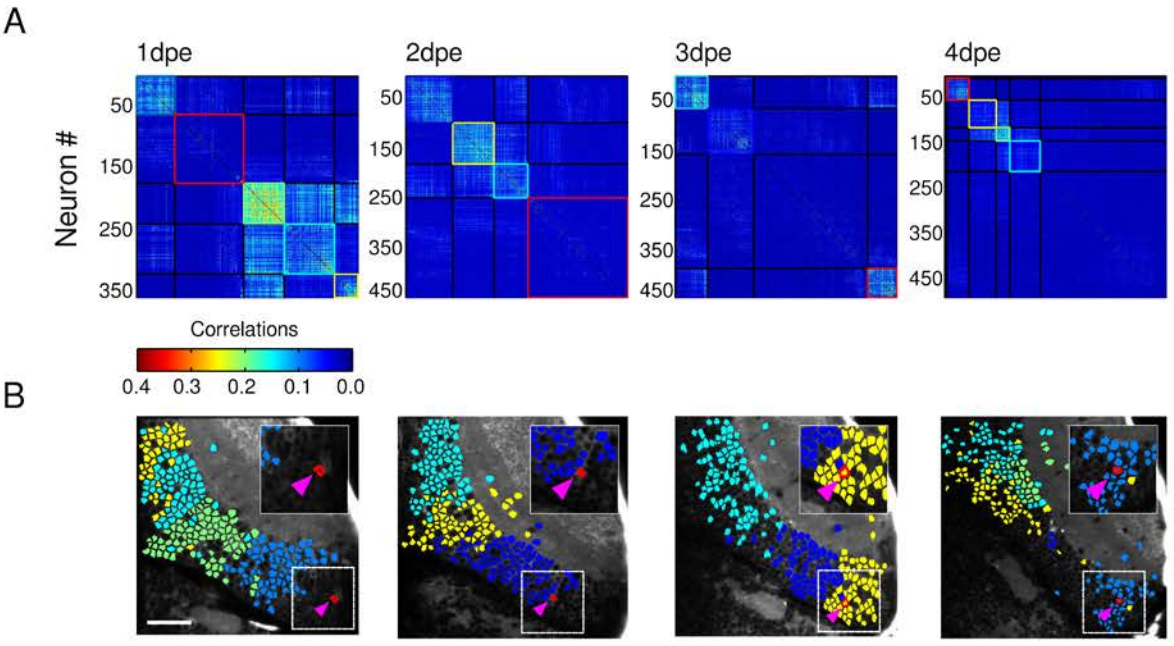

Fig. 3.14 K-means clusterization reveals the incorporation of newborn neurons into existent neuronal assemblies. **(A)** A representative example of the spontaneous activity correlation matrix between mature neurons, at the four developmental stages (1 to 4 dpe). The matrices are organized according to the K-means clustering algorithm. The clusters are framed in black except clusters containing the labeled developing newborn neurons that were framed in red. Note the increase of intra-cluster correlations at 3-4 dpe together with a reduction of clusters sizes, for the cluster containing the labeled newborn neuron. The recordings used are those from the example in **Figure 3.11A**. **(B)** Topographic representation of the significant clusters. The neurons are color-coded according to the clusters in **A** except the clusters containing the labeled cells that are colors in red. Insets are zoomed regions containing the newborn labeled cell (dashed square), denoted by magenta arrowheads and circled in red. Note the incorporation into significant spontaneous assemblies at 3-4 dpe. Scale bar 50 μm.

Table 3.3 **Proportion of newborn neurons incorporated into significant assemblies**, from 1 to 4 dpe.

	1 dpe	2 dpe	3 dpe	4 dpe
% of labeled neurons in significant clusters	0	11%	57%	86%
Number of neurons analyzed	5	9	14	7

At 1 dpe, labeled neurons were not significantly correlated with other neurons and therefore their distance index could not be computed (**see Figure 3.11**). At 2 and 3 dpe, the distance index was non-statistically different between electroporated and non-electroporated neurons (p=0.21 and p=0.38, respectively). However, I observed a significant decrease of the distance index between 3 and 4 dpe for non-electroporated neurons (0.16±0.02 to 0.08±0.01 AU, p-values=0.022, Mann-Whitney U-test) (**Figure 3.15B**). At 4 dpe, the distance index was significantly smaller than that of the non-electroporated population (0.08±0.01 AU for labeled and 0.14 AU for unlabeled neurons, p-value=0.023, Mann-Whitney U-test). Taken together, these results suggest that the labeled neurons first belong to several assemblies and progressively become members of just a unique neuronal assembly.

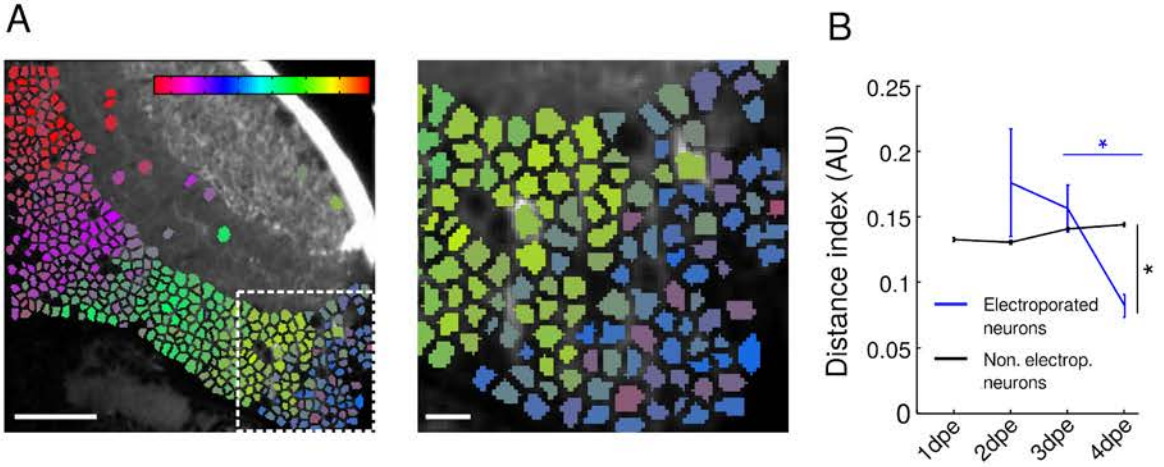

Fig. 3.15 **Fuzzy clustering reveals the intra-cluster dynamics of developing newborn neurons. (A)** Optical plane of the OT showing a representative example where neurons were color-coded according to their probability of belonging to a given cluster. Scale bar: 50 μm. The dashed squared region is enlarged in the right panel and shows the mixture of colors among newborn neurons. Scale bar: 10 μm. **(B)** Development of the distance index from 1 to 4 dpe for newborn (blue) and mature neurons (black), * indicates p<0.05. Error bars represent SEM.

Interestingly, the spontaneous activity structure of the OT remains almost unchanged if deprived of its main sensory input, the retina Romano et al. (2015). The dense tectal reciprocal connectivity (Akerman and Cline, 2006) has been suggested to explain such synchronous population events. My results suggest that the emergence of intratectal connectivity emerges at ∼3 dpe when newborn neurons begin to incorporate into functional neuronal assemblies (**Table 3.3**). Furthermore, by 4 dpe, newborn neurons acquire the ability to trigger population events (**Figure 3.13B**) via

dendro-dendritic excitatory synapses or electrical coupling through gap junctions with neighboring neurons located within ∼6 somatas distance (**Figure 3.11**).

3.3 Maturation of visually induced responses of newborn developing neurons

To gain more insights into the functional connectivity development of newborn neurons in the OT, I studied the developmental dynamics of their visually induced responses. More specifically, I presented visual stimuli to characterize the newborn neurons spatial RFs and their DS. The stimuli consisted of light spots presented at different regions of the visual field (90° x 40°: horizontal x vertical) and bars moving in the four cardinal directions (see **Material and methods**).

3.3.1 Emergence of direction selectivity in newborn neurons

In the zebrafish OT, DS cells can be observed from 72h, ie. 6h after the first visually induced responses (Niell and Smith, 2005). Selectivity to certain directions is inherited by retinal inputs (caudo-rostral, upwards and downwards motions) while an additional direction is computed exclusively in the OT (rostro-caudal motion) (Hunter et al., 2013). However, the temporal dynamics characterizing the emergence of DS in tectal newborn neurons, is still unknown.

To study the emergence of general visual responsiveness of newborn neurons, I compared the fluorescence levels before and after the presentation of visual stimuli (720 light spots and 16 bars, presented during 1h recordings). Neurons that displayed a significant increase in fluorescence after stimulation (light spots and bars pooled, $p<0.01$, Mann-Whitney U-test, see **Material and methods**) were considered to be visually responsive. Surprisingly, the majority of the newborn neurons (∼65%) were already visually responsive at 1 dpe, indicating that they already received either direct or indirect retinal inputs very early in their developmental process (**Figure 3.16A**).

Next, I studied the emergence of DS in newborn neurons. Interestingly at 1 dpe, 78±5.1% of all non-electroporated imaged tectal neurons were DS (**Figure 3.16B**, $n=5$ recordings, $k=1998$ neurons, DS index, $|DSI|>0.5$, either left vs. right of up vs down, see **Material and Methods**). This proportion remained stable up to 4 dpe (**Figure 3.16B**). As previously observed (Hunter et al., 2013), there was an over representation of DS neurons towards the right (rosto-caudal motion), while neurons

selective to either to upwards or downwards motion were equally represented at all stages (**Figure 3.16B**).

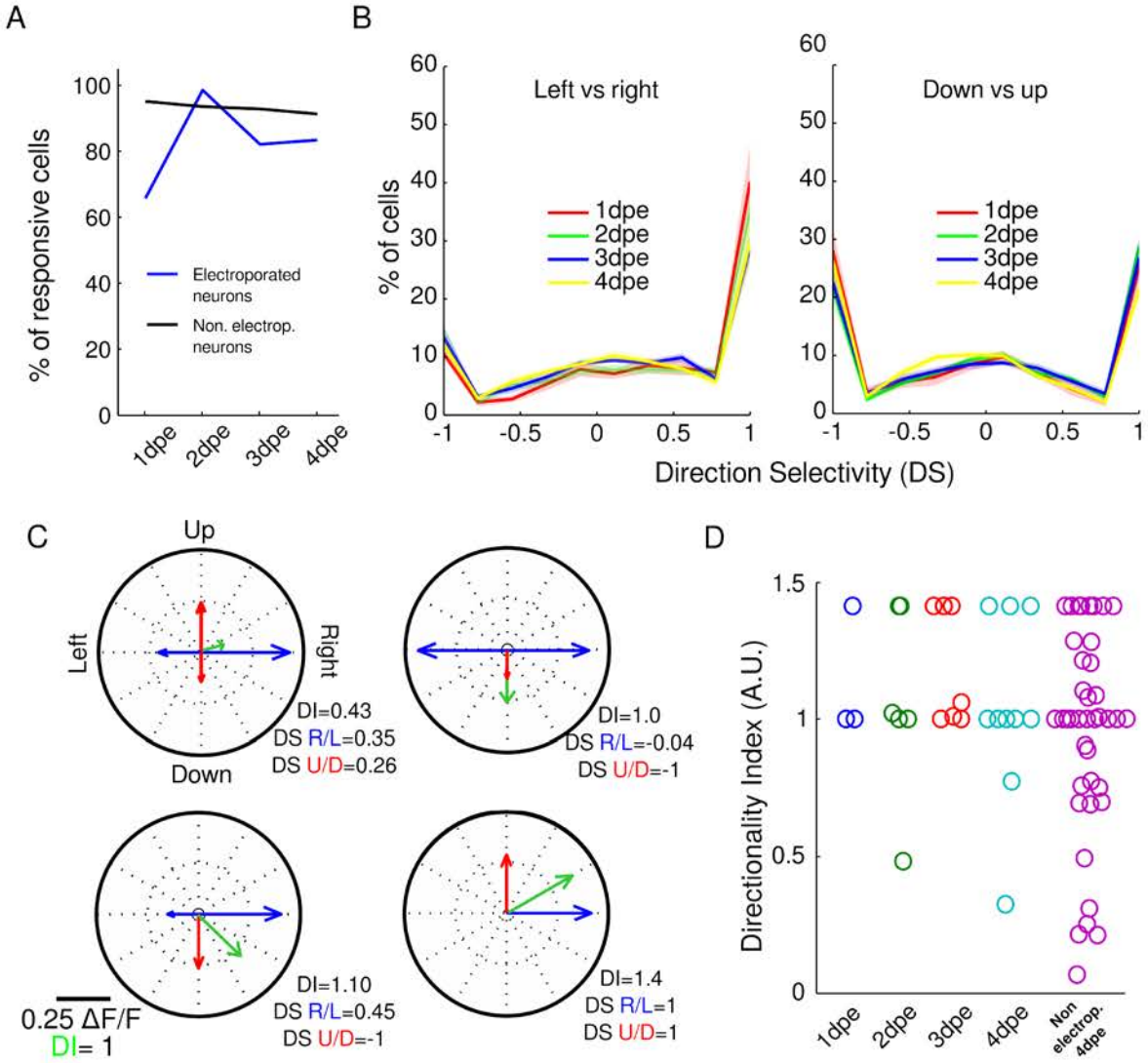

Fig. 3.16 **Newborn neurons rapidly become visually responsive and display tuned responses.** **(A)** Percentage of visually responsive cells both for electroporated and non-electroporated tectal neurons (blue and black curves, respectively). **(B)** Percentage of DS cells. left panel: left vs. right. right panel: up vs. down. The confidence intervals (shaded areas) represent the SEM. Bin size: 0.25. **(C)** Examples of polar plots showing average relative fluorescence changes ($\Delta F/F$) for all directions. Left vs. right in blue and up vs. down in red. Directionality index (DI) vectors (norm) are displayed in purple. Scalebar: 0.25 $\Delta F/F$ and 1 DI. Amplitude of responses and directionality indexes are indicated on the right bottom corners of each plot. **(D)** Developmental dynamics of the directionality index for the newborn neurons. A representative random sample of non electroporated neurons at 4 dpe is displayed in magenta.

Surprisingly, at 1 dpe all electroporated newborn neurons that were responsive to moving bars (50%, n=6) were already DS to at least one motion direction (either left vs. right of up vs down) (**Table 3.4**). The proportion of electroporated neurons that responded to moving bars increased with time (62% at 2 dpe to 85% at 4 dpe) and almost all were DS to at least one motion direction (27/28 neurons, all days pooled)

To analyze the global DS of newborn neurons, I devised a directionality index (DI) expressed as the norm of the resulting vector of the left vs. right and up vs. down DSI individual vectors (DI was higher than 1 when the neuron was completely DS for one direction and equal to $\sqrt{2}$ when it was equally DS for both directions and thus OS) (**Figure 3.16C**). The DI index was non-statistically different at all monitored days (**Figure 3.16D**, p-values>0.05, Mann-Whitney U-test, for all combinations of developmental stages considered, labeled and unlabeled neurons).

Overall, these results show that newborn neurons become DS as soon as they begin to respond to motion without exhibiting any further refinement, despite the large functional and morphological changes.

Table 3.4 **Proportion of direction selective neurons**, from 1 to 4 dpe. Neurons that were DS for at least one direction of motion (|DS|>0.5) were considered DS. The proportion of neurons responsive to bars and the number of neurons analyzed is indicated below.

	1 dpe	2 dpe	3 dpe	4 dpe
% of direction selective neurons	50%	62%	67%	85%
% of bars responsive neurons	50%	77%	67%	85%
Number of neurons analyzed	6	8	12	13

3.3.2 Emergence and developmental dynamics of newborn neurons' receptive fields

Using the previously described stimulation paradigm (see **Material and Methods**), I studied the development of newborn neurons RFs between 1 and 4 dpe (for the number of studied electroporated neurons see **Table 3.4**). For this purpose, I presented to the larva 5° light sport at the contralateral visual hemifield with respect to the recorded tectal hemisphere of the larva. The light spots covered an area of 90° x 40° (horizontal x vertical), resulting in a total of 36 different stimulated positions. Each position was stimulated 20 times. Due to the large variability of the responses and neuronal habituation I used for the computation of the average RFs only the 5 most correlated

trials among the 20 presented (see **Material and Methods**). Representative RF examples at each developmental stage after electroporation are shown in **Figure 3.17A**.

To assess the functional development of newborn neurons added to the OT, I computed their RF size from 1 to 4 dpe (5 to 8 dpf). At 1 dpe, RFs were significantly smaller than that of mature neurons (87.5±37.5 deg^2 and 415.0±6.0 deg^2 for electroporated and non-electroporated neurons, respectively, p-value=0.004) (**Figure 3.17B**). From 1 to 3 dpe newborn neurons RF sizes increased gradually (258.3±62.5 deg^2 at 2 dpe and 540.0±86.2 deg^2 at 3 dpe, p-values=0.038 between 1 and 2 dpe and 0.048 between 2 and 3 dpe, Mann-Whitney U-test) to match the sizes of those of mature neurons (**Figure 3.17Bii**). Indeed, at 3 and 4 dpe, the electroporated neurons RF sizes were non-statistically different than the non-electroporated neurons (p-values=0.89 and 0.36, Mann-Whitney U-test between electroporated and non electroporated neurons at 3 and 4 dpe, respectively). Therefore, newborn neurons acquire mature RFs sizes within 3 days of development (**Figure 3.17Bii**).

To gain more insights into the development of newborn neurons RFs I computed the amplitude of the peak of the neurons' receptive fields, at each stage. Peak responses within average RFs were defined as the first decile of induced responses with the highest amplitude. This enabled me to capture the maturation of the most significant RFs positions while excluding low amplitude responses. In electroporated neurons, peak responses were consistently smaller than in mature neurons (p-value<0.05 at all stages when comparing electroporated and non-electroporated neurons, **Figure 3.17C**).

However, newborn neurons peak responses increased sharply from 1-2 dpe to 3 dpe (0.25±0.03 $\Delta F/F$ at 2 dpe and 0.57±0.08 $\Delta F/F$ at 3 dpe, p-value=0.005, Mann-Whitney U-test) and remained stable thereafter (0.59±0.09 $\Delta F/F$ at 4 dpe, p-value=0.87, between 3 and 4 dpe, Mann-Whitney U-test, **Figure 3.17A** and **Figure 3.17C**).

Taken together, these results indicate that newborn neurons development is characterized by an increase of their RF sizes and the amplitude of their peaks at ∼3 dpe. Additionally, the sampled population suggests that RFs do not undergo further refinements after 3 dpe.

Moreover, the relationship between the amplitude of the visual response with respect to the distance away from the peak showed similar dynamics between 1 and 2 dpe, from peaks up to 90° distance (p-value>0.05 for distance bins of 10° from 0° to 90°, Mann-Whitney U-test) (**Figure 3.17D**). Between 2 and 3 dpe I observed a significant increase of the global response amplitude from peak to 80° distance (p-values<0.001

for all distance bins, except between 50 and 60°: p-value<0.05). From 3 to 4 dpe, the response amplitude distribution remained stable (p-value>0.14, at all distance bins from 0° to 90°, Mann-Whitney U-test).

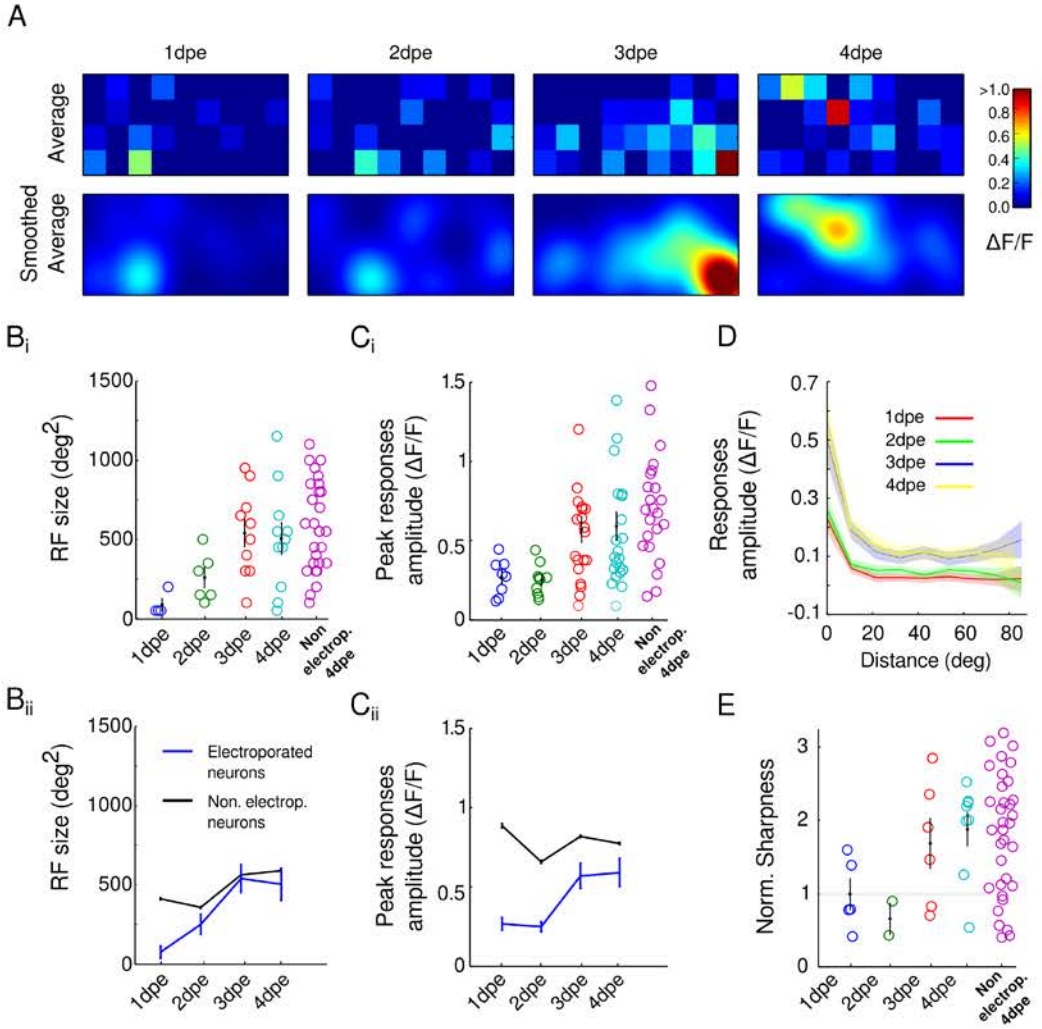

Fig. 3.17 **The RFs of newborn neurons become sharper as neurons develop.** **(A)** Representative examples of developing newborn neurons RFs from 1 to 4 dpe. Top: recorded RFs, bottom: smoothed RFs. **(Bi)** Evolution of the RF size of electroporated neurons. The mean and SEM are indicated in black dots and bars. A representative random sample of non-electroporated neurons at 4 dpe, extracted at 4 dpe is displayed in magenta. **(Bii)** Evolution of RF size for electroporated and non-electroporated neurons. **(Ci)** Evolution of peak responses' amplitude of electroporated neurons. Same conventions as in **Bi**. **(Cii)** Evolution of peak responses' amplitude for electroporated and non-electroporated neurons. Legends as in **Bii**. **(D)** Evolution of the response amplitude as a function of spatial distance in angular degrees from peaks. Bin sizes: 10°. The confidence intervals (shaded areas) represent the SEM. **(E)** Evolution of normalized sharpness for labeled neurons. Same conventions as in **Bi**.

In the OT RFs become progressively sharper during development (Dong and Aizenman, 2012; Zhang et al., 2011) probably shaped by emerging lateral inhibition (Sillito, 1975), thus providing spatial accuracy to the visual responses. To assess the evolution of sharpness of newborn neurons responses, Gaussian functions were fitted to the RFs. The sharpness was computed from the ratio of the half-maximum amplitude of the tuning curves over the half-band bandwidth at half maximum (see **Material and Methods**, **Figure 2.17**). Newborn neurons' sharpness increased from 1-2 dpe to 3 dpe (18.2±4.0 AU at 1 dpe and 30.9±6.4 AU at 3 dpe, p-value=0.043, Mann-Whitney U-test) and was non-significantly different at 3 and 4 dpe (30.9±6.4 AU at 3 dpe and 34.5±2.3 AU at 4 dpe, p-value=0.75, Mann-Whitney U-test). This result suggests that receptive fields become sharper as the newborn neurons develop, either by a selective synaptic strengthening or addition of connections corresponding to the emerging center of the maturing RFs between 1 and 3 dpe.

Moreover, at 3 and 4 dpe, the electroporated neurons sharpness was non-statistically different than the non-electroporated neurons (p-values=0.41 and 0.18, Mann-Whitney U-test between electroporated and non electroporated neurons at 3 and 4 dpe, respectively). Therefore, newborn neurons acquire mature sharpness within 3 days of development (**Figure 3.17Cii**).

Interestingly, one report has suggested that calcium indicators such as Oregon Green BAPTA-1 might distort neuronal tuning curves (Nauhaus et al., 2012) due to large Ca^{2+} affinity (Kd=170nM) leading to fluorescence saturation at high spiking rate (Yamada and Mikoshiba, 2012). However, GECI such as GCaMP5G (Akerboom et al., 2012) do not show such non-linear fluorescence dynamics. Therefore, our measurements are not distorted by the non-linearity of the used calcium indicator and reflect functional development of newborn neurons.

3.4 Chronic imaging of the spontaneous and induced activity during the circuit incorporation process – preliminary results

To get further insights on the functional principles underlying the incorporation of newborn neurons into mature tectal circuits, I monitored the developmental dynamics of the morphology, spontaneous and visually induced activity of the same newborn neuron for three consecutive days post electroporation (1-3 dpe). For this purpose, I took advantage of the Tol2 system that enables genomic integration of electroporated vectors

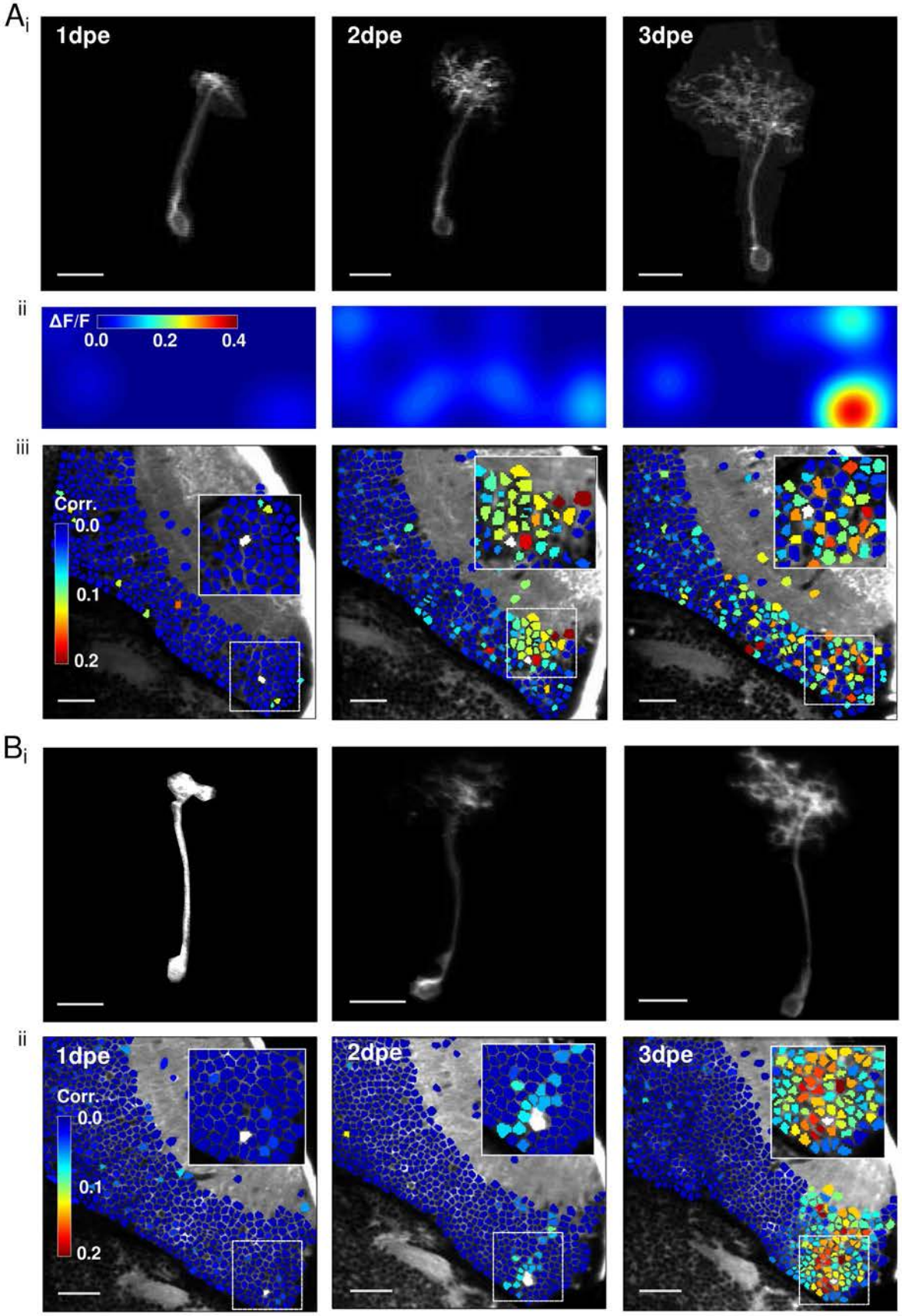

Fig. 3.18 **Developmental dynamics of two nsPVIN neurons imaged a 1, 2 and 3 dpe**, legend next page

Fig. 3.18 (Previous page.) **(A)** Developmental dynamics of a nsPVIN neuron imaged a 1, 2 and 3 dpe. **Ai**: Neuronal morphology. Scale bar: 10 µm. **Aii**: Averaged smoothed RFs. **Aiii**: Optical plane of the tectal imaged neurons. Neurons are color-coded according to their pair-wise correlation values (color scalebar) with the labeled neuron (white). Scale bar: 20 µm. The insets are a zoomed image of the white dashed squares. Note the distribution of correlated neurons: dense at 2 dpe and sparser at 3 dpe. **(B)** Developmental dynamics of the spontaneous activity of a different nsPVIN neuron imaged at 1, 2 and 3 dpe. **Bi**: Neuronal morphology. Scale bar: 10 µm. **Bii**: Optical plane of the tectal imaged neurons. Neurons are color-coded according to their pair-wise correlation values with the labeled neuron. Scale bar: 20 µm. The insets are a zoomed image of the white dashed squares. Note the distribution of correlated neurons: dense at 2 dpe, forming a thin radial column along the periventricular layer and a dense patch at 3 dpe.

(Sato et al., 2007a). This method enables monitoring electroporated neurons for several days. Then, using two-photon calcium imaging of HuC:Gal4, UAS:tdTomatoCAAX and UAS:Transposase electroporated *Tg(HuC:GCaMP5G)* larvae at 4 dpf, I recorded both visually induced and spontaneous activity of the tectal circuit and the same newborn electroporated neuron, for 3 consecutive days (n=2, See **Material and Methods**, **Figure 2.6**).

As suggested by previous experiments, the developing nsPVIN depicted in **Figure 3.18Ai** was visually responsive from 1 dpe, although the amplitude of the responses was weak (0.08 $\Delta F/F$ at peak response, **Figure 3.18Aii**). At this stage, the neuron was weakly correlated with sparse mature tectal neurons, with no discernible spatial structure (**Figure 3.18Aiii** and **Figure 3.11B**). At 2 dpe, the morphology matured and stronger visually induced responses could be observed (0.17 $\Delta F/F$ at peak response, **Figure 3.18Aii**). Simultaneously, higher spontaneous correlations with neighboring tectal neurons emerged (**Figure 3.18Aiii**). At 3 dpe, its RF became more robust and sharper as the amplitude of the RFs peak response increased while other positions that were eliciting neuronal responses were lost (compare 2 and 3 dpe, **Figure 3.18Aiii**). At 3 dpe, the labeled neuron was correlated with sparser and more distant neurons.

As suggested by previous recordings of developing spontaneous activity (**Figures 3.11-12**), this scattered spatial distribution of spontaneously correlated neurons represents a transitory stage. This process may indicate a developmental mechanism enabling the selection of mature neurons sharing similar functional properties as the newborn ones, a hypothesis that still needs to be tested (**Figure 3.11B**).

In a second example (**Figure 3.18B**), I observed the gradual emergence of the local spatial structure of the spontaneous correlation between the newborn neuron (also a

nsPVIN) and the mature network. Remarkably, at 2 and 3 dpe the correlated neurons were never sparsely distributed but rather located in the close vicinity of the developing neuron. It is possible that the transitory incorporation into sparser networks happens only in a fraction of developing newborn neurons or that functional maturation occurs with different dynamics.

Chapter 4

Conclusions and Perspectives

4.1 Summary

During my PhD project I have examined the functional incorporation of newborn neurons into mature neuronal circuits in the zebrafish larva's OT, its most complex layered structure and highest visual center. The use of the zebrafish larva as the experimental model enabled me to perform experiments in an intact, non-anesthetized and non-paralyzed vertebrate.

The experiments have been performed between 5 and 8 days, a period in which the OT is behaviorally functional (the larva displays tectum-dependent behaviors such as prey capture, Gahtan et al. (2005)). During this period the OT is still in constant growth. This growth is achieved by the addition of new neurons generated in the OT neurogenic zone spanning its entire length along the tectal ventricle: from the dorso-medial axis to its caudo-lateral margins (**Figure 1.18** and Recher et al. (2013)).

To study the functional development of newborn neurons, I developed a tool to label newborn neurons using in-vivo electroporation, a harmless technique that does not perturb the tectal circuit and enables monitoring their functional and morphological development. Using this technique, I recorded both spontaneous and visually induced activity of the labeled newborn and the surrounding mature tectal neurons.

I observed that newborn neurons were already spontaneously active at 1 dpe but weakly correlated with other tectal neurons. Starting at 2 dpe, correlations between their spontaneous activity and that of the mature tectal neurons began to emerge. By 3 dpe, the newborn-labeled neurons showed correlations with nearby neurons whose spatial distribution was similar to the correlations among mature neurons.

Most of the developing neurons (65%) were responsive to visual stimulation from 1 dpe indicating that they rapidly receive retinal inputs. Remarkably, as soon as they

responded to motion the newborn neurons were already DS, a property which remained stable thereafter. At this stage (1 dpe), responsive newborn neurons had small-size RFs. At 3 dpe, their sizes and sharpness increased and matched those of non-electroporated neurons (the mature ones).

Finally, I pioneered a technique to monitor the developmental dynamics of the same newborn neuron over several days. Overall, these results suggest a developmental sequence during which newborn neurons capable of generating intrinsic activity first connect to their pre-synaptic sensory organ (the retina). At a second stage, newborn neurons gradually incorporate into the tectal mature circuit by, showing first weak and sparse correlations with a few mature neurons and with a larger but still sparse population thereafter. The spatial distribution of the correlated mature neurons was later refined and became local and dense suggesting that the newborn neurons first connect to a large population of sparse mature neurons and subsequently distant connections are pruned, permitting the newborn-labeled neuron to acquire a stable and robust functional signature (e.g. a sharp receptive field).

Here, I discuss the obtained results, summarized in **Figure 4.1** and present further research paths to strengthen my conclusions and gain more insights into the formation of neuronal networks.

4.2 Discussion

4.2.1 Electroporation of newborn neurons

The first part of my thesis was dedicated to the development of a genetic method to label newborn neurons. This technique was adapted from previous reports by reducing the voltage to achieve sparse labeling and unexpectedly labeled specifically newborn neurons (**Figure 2.2** and Cerda et al. (2006); Hoegler and Horne (2010); Kera et al. (2010); Tawk et al. (2009)). Moreover, when combined with the Tol2/transposase genetic system it enabled long-term labeling (Kwan et al. (2007), **Material and Methods**, **Figure 2.1**). Overall, the technique was rapid (∼40 fish/hour for a trained experimentalist), non-toxic for cells and harmless to fish (98% survival, comparable to non- electroporated controls, See **Material and Methods**) and labeled newborn tectal neurons from 4 to 7 dpf, and at least for up to 10 days in the OT (**Figure 2.3** and **Figures 3.1-2**).

Electroporation could be combined with several types of fluorescence-proteins-expressing vectors: mKate2, tdTomato, EGFP, TagBFP2 and EBFP2 (**Figure 2.4**,

Figure 3.4 and data not shown). However, for all red-fluorescence proteins tested, only tdTomato and mKate2 were not toxic. Others, killed the expressing neurons within ∼2 days (mCherry, mRFP, mFusionRed, tdKatushka, TagRFP-T).

Besides the bias of the electroporation technique to label newborn neurons, the labeling was also biased towards one type of tectal interneuron (86% of nsPVIN, **Figure 3.7**). The bias towards newborn neurons could be explained by their position on the walls of the tectum. The bias towards nsPVIN can be explained by either an over-representation of these cells in the OT, or an over-production of these cells during the studied period. The use of other neuronal subtype-specific promoters (such as orthopadia targeting DS bsPVIN, Gabriel et al. (2012) or brn3a targeting neurons projecting to the hindbrain, Sato et al. (2007a)) could reveal whether the described developmental principles underlying the functional incorporation of newborn neurons into mature circuits can be generalized.

Overall, the electroporation technique described here is an easy tool to study the physiology of newborn neurons whose main advantage is to be quick to set-up, contrary to Cre/lox genetic tools requiring the establishment of transgenic lines (see Knopf et al. (2011) and Cheng et al. (2011)).

4.2.2 Development of spontaneous activity

Using spontaneous activity to determine functional connectivity between neurons, I shed light on a sequence of events leading to the acquisition of nsPVINs mature properties. I found that all newborn neurons were spontaneously active and the majority responded to visual stimuli already at 1 dpe (**Figure 3.10** and **Figure 3.16**). Previous work using BrdU pulse-chase experiments has demonstrated that at 4 dpf, dividing cells in the OT become neurons in less than 24h (Boulanger-Weill et al., unpublished results). Moreover, electroporated neurons were already differentiated at 1 dpe (expressing GCaMP5G in *Tg(HuC:GCaMP5G)* and were found just adjacent to the OT neurogenesis niche (**Figures 3.1-2**). Thus, dividing tectal progenitors (probably fast amplifying progenitors, Recher et al. (2013)) differentiate into neurons, become spontaneously active and visually responsive in less that 2 days.

Furthermore, I showed that within ∼3 days, electroporated neurons incorporated into neuronal assemblies organized in a retinotopic fashion (**Figure 3.14**). Using a fuzzy-clustering method I also observed that newborn neurons strengthened their connectivity to progressively become members of just a unique cluster (**Figure 3.15**). By studying the spatial distribution of significant correlations between newborn neurons and their mature counterparts, I observed the formation of dense neuronal assemblies

at 4 dpe (∼6 somata radius, **Figures 3.11-12**). At this stage the electroplated-labeled neurons became leaders: first neurons to be active during synchronous population events (**Figure 3.13**).

Since newborn neurons were responsive to visual stimulation before they displayed synchronous activity with their mature counterparts, direct retinal connectivity is probably established before the recurrent tectal connectivity. In the future, this hypothesis could be strengthened by expressing a ChR2 construct such as UAS:Chr2-tdTomato in newborn neurons to test whether neurons are first activated by RGCs (direct retinal inputs, by presenting visual stimulation) and then can trigger calcium events in their tectal neighbors by optogenetic stimulation.

Previous reports (Romano et al., 2015) have suggested that spontaneously active assemblies probably mirror the recurrent tectal connectivity mediated by GABAergic interneurons (see **Introduction**, **Figure 1.8** and Akerman and Cline (2006)). In the hippocampus, synchronous activity in newborn and mature granule cells is triggered by interneurons contacting both population (Markwardt et al., 2009). One possible mechanism is that GABAergic interneurons rapidly contact tectal newborn neurons providing excitatory inputs that are synchronized with mature assemblies, a hypothesis that still needs to be tested.

4.2.3 Maturation of receptive fields size and sharpness

From 1 to 3 dpe developing newborn neurons showed an increase in their RFs sizes and sharpness and at 4 dpe, both parameters were non-statistically different from the non-electroporated neurons (**Figure 3.17**). This observation could be explained by the selective addition or strengthening (by synaptic plasticity) of synapses in the emerging center of the developing RFs. Interestingly, Romano et al. (2015) have found evidence for reciprocal inhibition between visually evoked neuronal groups. Since the sharpness of a receptive field has been described to be shaped by lateral inhibition it is possible that the emergence of recurrent connectivity (i.e. incorporation into tectal assemblies, observed by studying spontaneous activity) plays a role in shaping spatially restricted neuronal responses.

4.2.4 Receptive fields size in non-electroporated neurons

Previous studies have shown that developing zebrafish tectal neurons undergo an increase of their RFs size from 4 to 6 dpf and then their size decreases from 6 to 8 dpf to reach sizes that were similar to 4 dpf (Zhang et al., 2011). In my experiments,

the sampled non-electroporated population did not follow the same developmental dynamics but rather increased in size, stabilizing around 8 dpf (**Figure 3.17Bii**). This difference could arise from the different technical approaches used (Zhang et al. (2011) used whole cells recording in fish with flattened retina measuring only the ON response) and/or the nature of the sampled neuronal population (only a specific type of inhibitory interneuron in my case).

4.2.5 Rapid emergence of direction selectivity

The electroporated newborn neuronal population was already DS as soon as it started to respond to moving visual stimuli (DS>0.5) and did not undergo further refinement thereafter (**Figure 3.16** and **Table 3.4**). Results obtained in the mice visual cortex (V1) have shed light on the mechanisms that might be involved during the functional specification of immature neurons. Indeed, in mice, DS is already present at eye opening and emerges independently of visual experience (Rochefort et al., 2011). One possible conclusion proposed by Rochefort et al. (2011) is that DS is already present in the retina at eye opening and is relayed in the visual cortex. In the zebrafish OT, several reports have demonstrated the existence of pre-synaptic DS inputs into dedicated tectal laminae (Gabriel et al., 2012; Nikolaou et al., 2012). Thus, I suggest that DS acquisition is a feedforward process inherited from the retina early in the development which remains stable thereafter (at least for the developmental period studied), rather than being an experience-dependent process based on inputs refinement and plasticity until the final DS is obtained.

Overall, these results suggest that the synaptic mechanisms shaping DS and RF follow different developmental dynamics and argues for two different mechanisms underlying the development of position and motion computation in nsPVIN.

4.2.6 Chronic recordings as a preliminary approach to study the interplay between spontaneous and induced activity

In the last part of my thesis project, I have pioneered neuronal recordings of the same newborn neuron for several days during its development (**Figure 3.18**). I have confirmed that newborn neurons first show few sparse and weak correlations with other tectal neurons, and progressively the correlations become stronger and spatially more organized (among neighboring neurons) forming dense local clusters. Because of the functional similarity of neurons that form tectal assemblies (Romano et al., 2015), transitory sparse correlation patterns may emerge to allow an activity-dependent

connectivity selection based on the match between their functional properties (such as DS and/or RF). A detailed study of the functional properties of transiently correlated neurons might be critical to understand how the final properties of newborn neurons are shaped during development.

Overall, this study provides new insights on the basic functional principles underlying the formation of neuronal circuits during development by shedding light on the functional dialogue between the newborn neuron and the matured neuronal network during the incorporation process. These results may open the door for the improvement of new stem-cell treatments for brain reparation in neurodegenerative diseases (e.g. Parkinson's disease) or brain trauma, by increasing the precision and the rate of incorporation while decreasing the risk of tumor formation.

4.3 Graphical summary

Fig. 4.1 **Graphical summary**, next page. Evolution of morphology, spontaneous activity and induced activity from 1 to 4 dpe (after performing electroporation at 4 dpf). Left panel: representative pictures of nsPVIN at 1, 2-3 and 4 dpe. Middle panel: representative stages of the evolution of spontaneous activity. At 1 dpe, newborn nsPVIN were not yet synchronized with their tectal counterparts, see fluorescence traces and pair-wise correlation values represented over the imaged tectal plane. The insets are zoomed images of the white dashed squares. At this stage, few correlations were significant (see bar charts) indicating that neurons were not yet connected to the tectal network. At 2-3 dpe, nsPVIN displayed correlated activity with their neighbors as indicated by the fluorescence traces and pair-wise correlations. These correlations were significant and in average scattered over the tectum (see bar charts). Later at 4 dpe, a refinement occurred and significantly correlated neurons were only found in the close vicinity of electroporated neurons (see tectal image and bar chart) suggesting connections pruning. Right panel: representative stages of the evolution of induced activity. At 1 dpe, neurons were already visually responsive indicating that they rapidly receive retinal inputs (see RF at 1 dpe). Once electroporated neurons started to respond to moving bars, they showed direction selectivity, responding only to one direction of motion as shown by the fluorescence traces (the direction of the presented stimuli are indicated in top). From 2-4 dpe, RFs matured: increasing in size and sharpness (see RFs at 2-3 and 4 dpe) to ultimately become similar to the non-electroporated neurons. My result suggest that newborn neurons acquire a stable and robust functional signature thanks to the pruning of transitory distant connections.

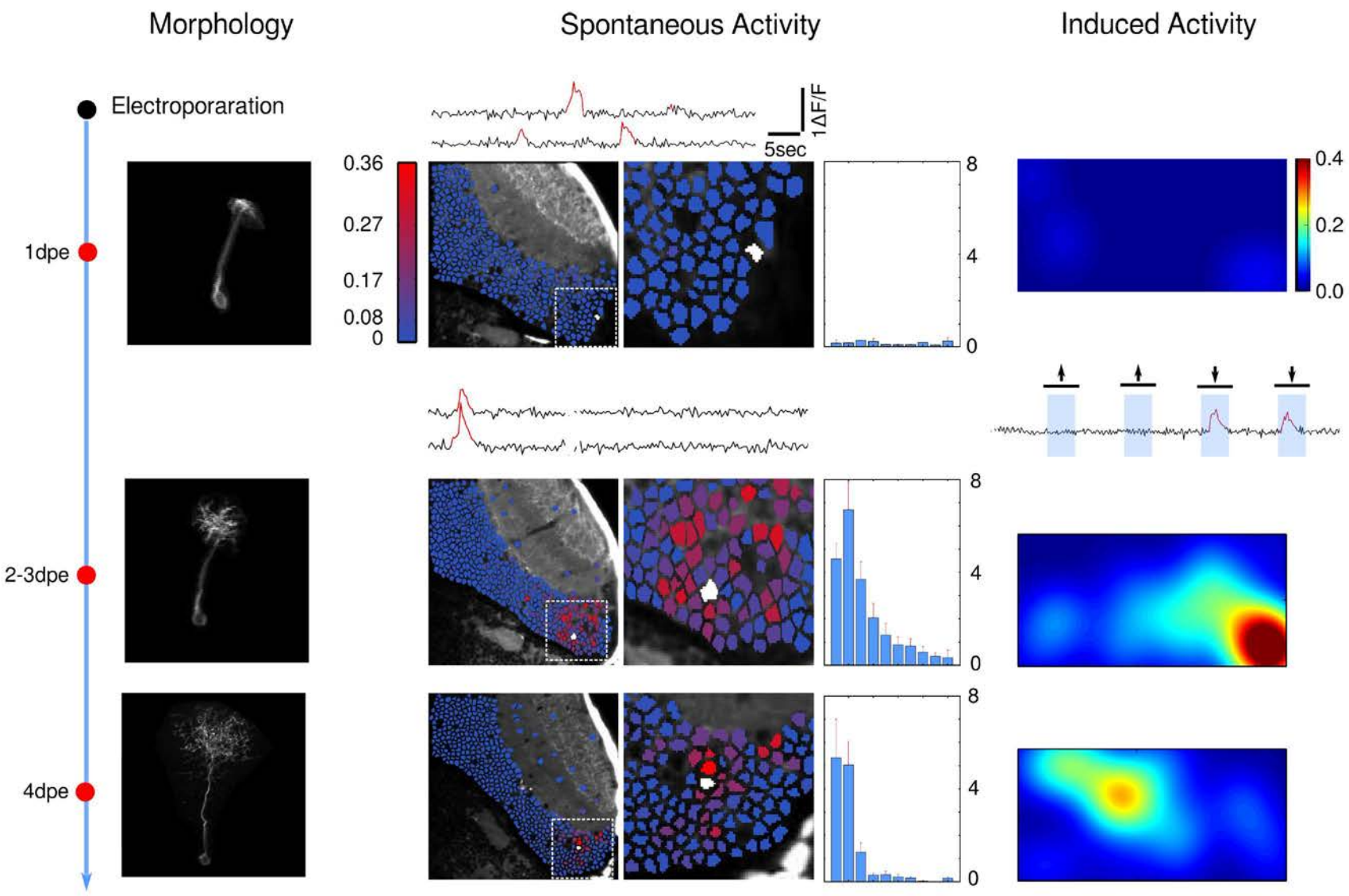

Fig. 4.1 **Graphical summary**, legend previous page

References

Ackman, J. B., Burbridge, T. J., and Crair, M. C. (2012). Retinal waves coordinate patterned activity throughout the developing visual system. *Nature*, 490(7419):219–225.

Ahrens, M. B. and Engert, F. (2015). ScienceDirect Large-scale imaging in small brains. *Current Opinion in Neurobiology*, pages 78–86.

Akerboom, J., Chen, T.-W., Wardill, T. J., Tian, L., Marvin, J. S., Mutlu, S., Calderon, N. C., Esposti, F., Borghuis, B. G., Sun, X. R., Gordus, a., Orger, M. B., Portugues, R., Engert, F., Macklin, J. J., Filosa, a., Aggarwal, a., Kerr, R. a., Takagi, R., Kracun, S., Shigetomi, E., Khakh, B. S., Baier, H., Lagnado, L., Wang, S. S.-H., Bargmann, C. I., Kimmel, B. E., Jayaraman, V., Svoboda, K., Kim, D. S., Schreiter, E. R., and Looger, L. L. (2012). Optimization of a GCaMP Calcium Indicator for Neural Activity Imaging. *Journal of Neuroscience*, 32(40):13819–13840.

Akerman, C. J. and Cline, H. T. (2006). Depolarizing GABAergic conductances regulate the balance of excitation to inhibition in the developing retinotectal circuit in vivo. *The Journal of neuroscience : the official journal of the Society for Neuroscience*, 26(19):5117–5130.

Albright, T. D., Jessell, T. M., Kandel, E. R., and Posner, M. I. (2000). Neural science: a century of progress and the mysteries that remain. *Neuron*, 25 Suppl:S1–S55.

Alonso, M., Lepousez, G., Wagner, S., Bardy, C., Gabellec, M.-M., Torquet, N., and Lledo, P.-M. (2012). Activation of adult-born neurons facilitates learning and memory. *Nature Neuroscience*, 15(6):897–904.

Altman, J. and Das, G. D. (1965). Autoradiographic and histological evidence of postnatal hippocampal neurogenesis in rats. *The Journal of comparative neurology*, 124(3):319–335.

Alunni, A., Hermel, J.-M., Heuzé, A., Bourrat, F., Jamen, F., and Joly, J.-S. (2010). Evidence for neural stem cells in the medaka optic tectum proliferation zones. *Developmental neurobiology*, 70(10):693–713.

Amariglio, N., Hirshberg, A., Scheithauer, B. W., Cohen, Y., Loewenthal, R., Trakhtenbrot, L., Paz, N., Koren-Michowitz, M., Waldman, D., Leider-Trejo, L., Toren, A., Constantini, S., and Rechavi, G. (2009). Donor-derived brain tumor following neural stem cell transplantation in an ataxia telangiectasia patient. *PLoS Medicine*, 6(2):0221–0231.

Arrenberg, A. B., Stainier, D. Y. R., Baier, H., and Huisken, J. (2010). Optogenetic control of cardiac function. *Science (New York, N.Y.)*, 330(6006):971–974.

Baier, H. (2013). Synaptic laminae in the visual system: molecular mechanisms forming layers of perception. *Annual review of cell and developmental biology*, 29:385–416.

Balasko, B., Abonyi, J., and Feil, B. (2005). Fuzzy clustering and data analysis toolbox. *Department of Process Engineering, University of Veszprem, Veszprem*.

Balciunas, D., Wangensteen, K. J., Wilber, A., Bell, J., Geurts, A., Sivasubbu, S., Wang, X., Hackett, P. B., Largaespada, D. a., McIvor, R. S., and Ekker, S. C. (2006). Harnessing a high cargo-capacity transposon for genetic applications in vertebrates. *PLoS Genetics*, 2(11):1715–1724.

Bardy, C., Alonso, M., Bouthour, W., and Lledo, P.-M. (2010). How, when, and where new inhibitory neurons release neurotransmitters in the adult olfactory bulb. *The Journal of neuroscience : the official journal of the Society for Neuroscience*, 30(50):17023–17034.

Ben Fredj, N., Hammond, S., Otsuna, H., Chien, C.-B., Burrone, J., and Meyer, M. P. (2010). Synaptic activity and activity-dependent competition regulates axon arbor maturation, growth arrest, and territory in the retinotectal projection. *The Journal of neuroscience : the official journal of the Society for Neuroscience*, 30(32):10939–10951.

Bergmann, O., Liebl, J., Bernard, S., Alkass, K., Yeung, M. S. Y., Steier, P., Kutschera, W., Johnson, L., Landén, M., Druid, H., Spalding, K. L., and Frisén, J. (2012). The Age of Olfactory Bulb Neurons in Humans. *Neuron*, 74(4):634–639.

Blankenship, A. G., Blankenship, A. G., Feller, M. B., and Feller, M. B. (2009). Mechanisms underlying spontaneous patterned activity in developing neural circuits. *Nature Reviews Neuroscience*, 11(1):18–29.

Bock, D. D., Lee, W.-C. A., Kerlin, A. M., Andermann, M. L., Hood, G., Wetzel, A. W., Yurgenson, S., Soucy, E. R., Kim, H. S., and Reid, R. C. (2011). Network anatomy and in vivo physiology of visual cortical neurons. *Nature*, 471(7337):177–182.

Braak, H. and Del Tredici, K. (2008). Assessing fetal nerve cell grafts in Parkinson's disease. *Nature medicine*, 14(5):483–485.

Brainard, D. H. (1997). The psychophysics toolbox. *Spatial vision*, 10:433–436.

Burbridge, T. J., Xu, H.-p., Ackman, J. B., Ge, X., Zhang, Y., Ye, M.-j., Zhou, Z. J., Xu, J., Contractor, A., and Crair, M. C. (2014). Visual circuit development requires patterned activity mediated by retinal acetylcholine receptors. *Neuron*, 84(5):1049–1064.

Burrill, J. D. and Easter, S. S. (1994). Development of the retinofugal projections in the embryonic and larval zebrafish (brachydanio rerio). *Journal of Comparative Neurology*, 346(4):583–600.

Cang, J. and Feldheim, D. a. (2013). Developmental mechanisms of topographic map formation and alignment. *Annual review of neuroscience*, 36(April 2013):51–77.

Cang, J., Wang, L., Stryker, M. P., and Feldheim, D. a. (2008). Roles of ephrin-as and structured activity in the development of functional maps in the superior colliculus. *The Journal of neuroscience : the official journal of the Society for Neuroscience*, 28(43):11015–11023.

Carleton, A., Petreanu, L. T., Lansford, R., Alvarez-Buylla, A., and Lledo, P.-M. (2003). Becoming a new neuron in the adult olfactory bulb. *Nature neuroscience*, 6(5):507–518.

Cerda, G. a., Thomas, J. E., Allende, M. L., Karlstrom, R. O., and Palma, V. (2006). Electroporation of DNA, RNA, and morpholinos into zebrafish embryos. *Methods*, 39(3):207–211.

Chandrasekaran, A. R., Plas, D. T., Gonzalez, E., and Crair, M. C. (2005). Evidence for an instructive role of retinal activity in retinotopic map refinement in the superior colliculus of the mouse. *The Journal of neuroscience : the official journal of the Society for Neuroscience*, 25(29):6929–6938.

Chapouton, P. and Bally-Cuif, L. (2004). Neurogenesis. *Methods in cell biology*, 76:163–206.

Chapouton, P., Jagasia, R., and Bally-Cuif, L. (2007). Adult neurogenesis in non-mammalian vertebrates. *BioEssays*, 29(8):745–757.

Chen, B. L., Hall, D. H., and Chklovskii, D. B. (2006). Wiring optimization can relate neuronal structure and function. *Proceedings of the National Academy of Sciences of the United States of America*, 103(12):4723–4728.

Chen, J. L. and Nedivi, E. (2010). Neuronal structural remodeling: Is it all about access? *Current Opinion in Neurobiology*, 20(5):557–562.

Cheng, X., Li, Y., Huang, Y., Feng, X., Feng, G., and Xiong, Z.-Q. (2011). Pulse labeling and long-term tracing of newborn neurons in the adult subgranular zone. *Cell research*, 21(2):338–349.

Deeg, K. E. and Aizenman, C. D. (2011). Sensory modality-specific homeostatic plasticity in the developing optic tectum. *Nature neuroscience*, 14(5):548–550.

Del Bene, F., Wyart, C., Robles, E., Tran, A., Looger, L., Scott, E. K., Isacoff, E. Y., and Baier, H. (2010). Filtering of visual information in the tectum by an identified neural circuit. *Science (New York, N.Y.)*, 330(6004):669–673.

Demas, J. a., Payne, H., and Cline, H. T. (2012). Vision drives correlated activity without patterned spontaneous activity in developing Xenopus retina. *Developmental Neurobiology*, 72(4):537–546.

Denk, W., Strickler, J. H., and Webb, W. W. (1990). Two-photon laser scanning fluorescence microscopy. *Science*, 248(4951):73–76.

Dombeck, D. A., Khabbaz, A. N., Collman, F., Adelman, T. L., and Tank, D. W. (2007). Imaging large-scale neural activity with cellular resolution in awake, mobile mice. *Neuron*, 56(1):43–57.

Dong, W. and Aizenman, C. D. (2012). A Competition-Based Mechanism Mediates Developmental Refinement of Tectal Neuron Receptive Fields. *Journal of Neuroscience*, 32(47):16872–16879.

Dotti, G., Sullivan, a., Biology, C., College, A. M., and York, N. (1988). The Establishment of Polarity by Hippocampal. (April).

Douglas, R. J. and Martin, K. a. C. (2004). Neuronal circuits of the neocortex. *Annual review of neuroscience*, 27:419–451.

Douglass, A. D., Kraves, S., Deisseroth, K., Schier, A. F., and Engert, F. (2008). Escape Behavior Elicited by Single, Channelrhodopsin-2-Evoked Spikes in Zebrafish Somatosensory Neurons. *Current Biology*, 18(15):1133–1137.

Drobizhev, M., Makarov, N. S., Tillo, S. E., Hughes, T. E., and Rebane, A. (2011). Two-photon absorption properties of fluorescent proteins. *Nature methods*, 8(5):393–399.

D'Souza, J., Hendricks, M., Le Guyader, S., Subburaju, S., Grunewald, B., Scholich, K., and Jesuthasan, S. (2005). Formation of the retinotectal projection requires esrom, an ortholog of pam (protein associated with myc). *Development*, 132(2):247–256.

Duffy, K. T., McAleer, M. F., Davidson, W. R., Kari, L., Kari, C., Liu, C. G., Farber, S. a., Cheng, K. C., Mest, J. R., Wickstrom, E., Dicker, A. P., and Rodeck, U. (2005). Coordinate control of cell cycle regulatory genes in zebrafish development tested by cyclin D1 knockdown with morpholino phosphorodiamidates and hydroxyprolyl-phosphono peptide nucleic acids. *Nucleic Acids Research*, 33(15):4914–4921.

Endeman, D., Klaassen, L. J., and Kamermans, M. (2013). Action Spectra of Zebrafish Cone Photoreceptors. *PLoS ONE*, 8(7).

Eriksson, P. S., Perfilieva, E., Björk-Eriksson, T., Alborn, a. M., Nordborg, C., Peterson, D. a., and Gage, F. H. (1998). Neurogenesis in the adult human hippocampus. *Nature medicine*, 4(11):1313–1317.

Ernst, A., Alkass, K., Bernard, S., Salehpour, M., Perl, S., Tisdale, J., Possnert, G., Druid, H., and Frisén, J. (2014). Neurogenesis in the striatum of the adult human brain. *Cell*, 156(5):1072–1083.

Ernst, A. and Frisén, J. (2015). Adult Neurogenesis in Humans- Common and Unique Traits in Mammals. pages 1–12.

Espósito, M. S., Piatti, V. C., Laplagne, D. a., Morgenstern, N. a., Ferrari, C. C., Pitossi, F. J., and Schinder, A. F. (2005). Neuronal differentiation in the adult hippocampus recapitulates embryonic development. *The Journal of neuroscience : the official journal of the Society for Neuroscience*, 25(44):10074–10086.

Evans, J. R., Mason, S. L., and Barker, R. a. (2012). *Current status of clinical trials of neural transplantation in Parkinson's disease*, volume 200. Elsevier B.V., 1 edition.

Feldt, S., Bonifazi, P., and Cossart, R. (2011). Dissecting functional connectivity of neuronal microcircuits: Experimental and theoretical insights. *Trends in Neurosciences*, 34(5):225–236.

Feliciano, D. M. and Bordey, A. (2013). Newborn cortical neurons: Only for neonates? *Trends in Neurosciences*, 36(1):51–61.

Fetcho, J. R. (2012). Neuroscience: Crystal–clear brains. *Nature*, 485(7399):453–455.

Flanagan, J. G. and Vanderhaeghen, P. (1998). The ephrins and eph receptors in neural development. *Annual review of neuroscience*, 21(1):309–345.

Fosque, B. F., Dana, H., Yang, C.-t., Ohyama, T., Tadross, M. R., Patel, R., Zlatic, M., Kim, D. S., Ahrens, M. B., Jayaraman, V., and Looger, L. L. (2015). Labeling of active neural circuits in vivo with designed calcium integrators. 347(6223).

Fox, M. D., Snyder, A. Z., Vincent, J. L., Corbetta, M., Van Essen, D. C., and Raichle, M. E. (2005). The human brain is intrinsically organized into dynamic, anticorrelated functional networks. *Proceedings of the National Academy of Sciences of the United States of America*, 102(27):9673–9678.

Friedrich, R. W., Jacobson, G. a., and Zhu, P. (2010). Circuit Neuroscience in Zebrafish. *Current Biology*, 20(8):R371–R381.

Gabriel, J. P., Trivedi, C. a., Maurer, C. M., Ryu, S., and Bollmann, J. H. (2012). Layer-Specific Targeting of Direction-Selective Neurons in the Zebrafish Optic Tectum. *Neuron*, 76(6):1147–1160.

Gahtan, E., Tanger, P., and Baier, H. (2005). Visual prey capture in larval zebrafish is controlled by identified reticulospinal neurons downstream of the tectum. *The Journal of neuroscience : the official journal of the Society for Neuroscience*, 25(40):9294–9303.

Ge, S., Goh, E. L. K., Sailor, K. a., Kitabatake, Y., Ming, G.-l., and Song, H. (2006). GABA regulates synaptic integration of newly generated neurons in the adult brain. *Nature*, 439(7076):589–593.

Georgopoulos, A. P., Schwartz, A. B., and Kettner, R. E. (1986). Neuronal population coding of movement direction. *Science*, 233(4771):1416–1419.

Gont, L. K., Steinbeisser, H., Blumberg, B., and de Robertis, E. M. (1993). Tail formation as a continuation of gastrulation: the multiple cell populations of the Xenopus tailbud derive from the late blastopore lip. *Development (Cambridge, England)*, 119(4):991–1004.

Gonzalez, R. C., Woods, R. E., and Eddins, S. L. (2004). *Digital image processing using MATLAB*. Pearson Education India.

Grama, A. and Engert, F. (2012). Direction selectivity in the larval zebrafish tectum is mediated by asymmetric inhibition. *Frontiers in Neural Circuits*, 6(September):1–9.

Grandel, H. and Brand, M. (2013). Comparative aspects of adult neural stem cell activity in vertebrates. *Development Genes and Evolution*, 223(1-2):131–147.

Grienberger, C., Rochefort, N. L., Adelsberger, H., Henning, H. a., Hill, D. N., Reichwald, J., Staufenbiel, M., and Konnerth, A. (2012). Staged decline of neuronal function in vivo in an animal model of Alzheimer's disease. *Nature Communications*, 3:774.

Hagell, P. and Cenci, M. A. (2005). Dyskinesias and dopamine cell replacement in Parkinson's disease: A clinical perspective. *Brain Research Bulletin*, 68(1-2):4–15.

Harris, K. D. (2005). Neural signatures of cell assembly organization. *Nature reviews. Neuroscience*, 6(5):399–407.

Hoegler, K. J. and Horne, J. H. (2010). Targeting the zebrafish optic tectum using in vivo electroporation. *Cold Spring Harbor Protocols*, 5(7).

Holtmaat, A., Bonhoeffer, T., Chow, D. K., Chuckowree, J., De Paola, V., Hofer, S. B., Hübener, M., Keck, T., Knott, G., Lee, W.-C. a., Mostany, R., Mrsic-Flogel, T. D., Nedivi, E., Portera-Cailliau, C., Svoboda, K., Trachtenberg, J. T., and Wilbrecht, L. (2009). Long-term, high-resolution imaging in the mouse neocortex through a chronic cranial window. *Nature protocols*, 4(8):1128–1144.

Homem, C. C. F. and Knoblich, J. a. (2012). Drosophila neuroblasts: a model for stem cell biology. *Development (Cambridge, England)*, 139(23):4297–310.

Howe, K., Clark, M. D., Torroja, C. F., Torrance, J., Berthelot, C., Muffato, M., Collins, J. E., Humphray, S., McLaren, K., Matthews, L., McLaren, S., Sealy, I., Caccamo, M., Churcher, C., Scott, C., Barrett, J. C., Koch, R., Rauch, G.-J., White, S., Chow, W., Kilian, B., Quintais, L. T., Guerra-Assunção, J. a., Zhou, Y., Gu, Y., Yen, J., Vogel, J.-H., Eyre, T., Redmond, S., Banerjee, R., Chi, J., Fu, B., Langley, E., Maguire, S. F., Laird, G. K., Lloyd, D., Kenyon, E., Donaldson, S., Sehra, H., Almeida-King, J., Loveland, J., Trevanion, S., Jones, M., Quail, M., Willey, D., Hunt, A., Burton, J., Sims, S., McLay, K., Plumb, B., Davis, J., Clee, C., Oliver, K., Clark, R., Riddle, C., Elliot, D., Eliott, D., Threadgold, G., Harden, G., Ware, D., Begum, S., Mortimore, B., Mortimer, B., Kerry, G., Heath, P., Phillimore, B., Tracey, A., Corby, N., Dunn, M., Johnson, C., Wood, J., Clark, S., Pelan, S., Griffiths, G., Smith, M., Glithero, R., Howden, P., Barker, N., Lloyd, C., Stevens, C., Harley, J., Holt, K., Panagiotidis, G., Lovell, J., Beasley, H., Henderson, C., Gordon, D., Auger, K., Wright, D., Collins, J., Raisen, C., Dyer, L., Leung, K., Robertson, L., Ambridge, K., Leongamornlert, D., McGuire, S., Gilderthorp, R., Griffiths, C., Manthravadi, D., Nichol, S., Barker, G., Whitehead, S., Kay, M., Brown, J., Murnane, C., Gray, E., Humphries, M., Sycamore, N., Barker, D., Saunders, D., Wallis, J., Babbage, A., Hammond, S., Mashreghi-Mohammadi, M., Barr, L., Martin, S., Wray, P., Ellington, A., Matthews, N., Ellwood, M., Woodmansey, R., Clark, G., Cooper, J. D., Cooper, J., Tromans, A., Grafham, D., Skuce, C., Pandian, R., Andrews, R., Harrison, E., Kimberley, A., Garnett, J., Fosker, N., Hall, R., Garner, P., Kelly, D., Bird,

C., Palmer, S., Gehring, I., Berger, A., Dooley, C. M., Ersan-Ürün, Z., Eser, C., Geiger, H., Geisler, M., Karotki, L., Kirn, A., Konantz, J., Konantz, M., Oberländer, M., Rudolph-Geiger, S., Teucke, M., Lanz, C., Raddatz, G., Osoegawa, K., Zhu, B., Rapp, A., Widaa, S., Langford, C., Yang, F., Schuster, S. C., Carter, N. P., Harrow, J., Ning, Z., Herrero, J., Searle, S. M. J., Enright, A., Geisler, R., Plasterk, R. H. a., Lee, C., Westerfield, M., de Jong, P. J., Zon, L. I., Postlethwait, J. H., Nüsslein-Volhard, C., Hubbard, T. J. P., Roest Crollius, H., Rogers, J., and Stemple, D. L. (2013). The zebrafish reference genome sequence and its relationship to the human genome. *Nature*, 496(7446):498–503.

Hua, J. Y., Smear, M. C., Baier, H., and Smith, S. J. (2005). Regulation of axon growth in vivo by activity-based competition. *Nature*, 434(7036):1022–1026.

Huberman, A. D., Feller, M. B., and Chapman, B. (2008a). Mechanisms underlying development of visual maps and receptive fields. *Annual review of neuroscience*, 31:479–509.

Huberman, A. D., Manu, M., Koch, S. M., Susman, M. W., Lutz, A. B., Ullian, E. M., Baccus, S. a., and Barres, B. a. (2008b). Architecture and Activity-Mediated Refinement of Axonal Projections from a Mosaic of Genetically Identified Retinal Ganglion Cells. *Neuron*, 59(3):425–438.

Hunter, P. R., Lowe, A. S., Thompson, I. D., and Meyer, M. P. (2013). Emergent properties of the optic tectum revealed by population analysis of direction and orientation selectivity. *The Journal of neuroscience : the official journal of the Society for Neuroscience*, 33(35):13940–5.

Huttner, H. B., Bergmann, O., Salehpour, M., Rácz, A., Tatarishvili, J., Lindgren, E., Csonka, T., Csiba, L., Hortobágyi, T., Méhes, G., Englund, E., Solnestam, B. W., Zdunek, S., Scharenberg, C., Ström, L., Stå hl, P., Sigurgeirsson, B., Dahl, A., Schwab, S., Possnert, G., Bernard, S., Kokaia, Z., Lindvall, O., Lundeberg, J., and Frisén, J. (2014). The age and genomic integrity of neurons after cortical stroke in humans. *Nature neuroscience*, 17(6):801–3.

Imaizumi, K., Shih, J. Y., and Farris, H. E. (2013). Global hyper-synchronous spontaneous activity in the developing optic tectum. *Scientific reports*, 3:1552.

Ito, Y., Tanaka, H., Okamoto, H., and Ohshima, T. (2010). Characterization of neural stem cells and their progeny in the adult zebrafish optic tectum. *Developmental Biology*, 342(1):26–38.

Kaplan, M. S., McNelly, N. a., and Hinds, J. W. (1985). Population dynamics of adult-formed granule neurons of the rat olfactory bulb. *The Journal of comparative neurology*, 239(1):117–125.

Kaslin, J., Ganz, J., and Brand, M. (2008). Proliferation, neurogenesis and regeneration in the non-mammalian vertebrate brain. *Philosophical transactions of the Royal Society of London. Series B, Biological sciences*, 363(1489):101–122.

Kawano, H., Kogure, T., Abe, Y., Mizuno, H., and Miyawaki, A. (2008). Two-photon dual-color imaging using fluorescent proteins. *Nature methods*, 5(5):373–374.

Kelsch, W., Lin, C.-W., Mosley, C. P., and Lois, C. (2009). A critical period for activity-dependent synaptic development during olfactory bulb adult neurogenesis. *The Journal of neuroscience : the official journal of the Society for Neuroscience*, 29(38):11852–11858.

Kera, S. a., Agerwala, S. M., and Horne, J. H. (2010). The temporal resolution of in vivo electroporation in zebrafish: a method for time-resolved loss of function. *Zebrafish*, 7(1):97–108.

Kerschensteiner, D., Morgan, J. L., Parker, E. D., Lewis, R. M., and Wong, R. O. L. (2009). Neurotransmission selectively regulates synapse formation in parallel circuits in vivo. *Nature*, 460(7258):1016–1020.

Kim, C.-H., Ueshima, E., Muraoka, O., Tanaka, H., Yeo, S.-Y., Huh, T.-L., and Miki, N. (1996). Zebrafish elav/huc homologue as a very early neuronal marker. *Neuroscience letters*, 216(2):109–112.

Kimmel, C. B., Ballard, W. W., Kimmel, S. R., Ullmann, B., Schilling, T. F., et al. (1995). Stages of embryonic development of the zebrafish. *Developmental dynamics*, 203(3):253–310.

Kimura, Y., Okamura, Y., and Higashijima, S.-i. (2006). alx, a zebrafish homolog of Chx10, marks ipsilateral descending excitatory interneurons that participate in the regulation of spinal locomotor circuits. *The Journal of neuroscience : the official journal of the Society for Neuroscience*, 26(21):5684–5697.

Kirkby, L. a., Sack, G. S., Firl, A., and Feller, M. B. (2013). A role for correlated spontaneous activity in the assembly of neural circuits. *Neuron*, 80(5):1129–1144.

Kirkeby, A., Grealish, S., Wolf, D. a., Nelander, J., Wood, J., Lundblad, M., Lindvall, O., and Parmar, M. (2012). Generation of Regionally Specified Neural Progenitors and Functional Neurons from Human Embryonic Stem Cells under Defined Conditions. *Cell Reports*, 1(6):703–714.

Knopf, F., Hammond, C., Chekuru, A., Kurth, T., Hans, S., Weber, C. W., Mahatma, G., Fisher, S., Brand, M., Schulte-Merker, S., and Weidinger, G. (2011). Bone regenerates via dedifferentiation of osteoblasts in the zebrafish fin. *Developmental Cell*, 20(5):713–724.

Ko, H., Cossell, L., Baragli, C., Antolik, J., Clopath, C., Hofer, S. B., and Mrsic-Flogel, T. D. (2013). The emergence of functional microcircuits in visual cortex. *Nature*, 496(7443):96–100.

Ko, H., Hofer, S. B., Pichler, B., Buchanan, K. a., Sjöström, P. J., and Mrsic-Flogel, T. D. (2011). Functional specificity of local synaptic connections in neocortical networks. *Nature*, 473(7345):87–91.

Ko, H., Mrsic-Flogel, T. D., and Hofer, S. B. (2014). Emergence of Feature-Specific Connectivity in Cortical Microcircuits in the Absence of Visual Experience. *Journal of Neuroscience*, 34(29):9812–9816.

Kriks, S., Shim, J.-W., Piao, J., Ganat, Y. M., Wakeman, D. R., Xie, Z., Carrillo-Reid, L., Auyeung, G., Antonacci, C., Buch, A., Yang, L., Beal, M. F., Surmeier, D. J., Kordower, J. H., Tabar, V., and Studer, L. (2011). Dopamine neurons derived from human ES cells efficiently engraft in animal models of Parkinson's disease. *Nature*, 480(7378):547–551.

Kubo, F., Hablitzel, B., DalMaschio, M., Driever, W., Baier, H., and Arrenberg, A. B. (2014). Functional architecture of an optic flow-responsive area that drives horizontal eye movements in zebrafish. *Neuron*, 81(6):1344–1359.

Kwan, K. M., Fujimoto, E., Grabher, C., Mangum, B. D., Hardy, M. E., Campbell, D. S., Parant, J. M., Yost, H. J., Kanki, J. P., and Chien, C. B. (2007). The Tol2kit: A multisite gateway-based construction Kit for Tol2 transposon transgenesis constructs. *Developmental Dynamics*, 236(11):3088–3099.

Le Magueresse, C. and Monyer, H. (2013). GABAergic Interneurons Shape the Functional Maturation of the Cortex. *Neuron*, 77(3):388–405.

Lee, C., Lee, C., Rohrer, W. H., Rohrer, W. H., Sparks, D. L., and Sparks, D. L. (1988). Population coding of saccadic eye movements by neurons in the superior colliculus.

Lepousez, G. and Lledo, P. M. (2013). Odor Discrimination Requires Proper Olfactory Fast Oscillations in Awake Mice. *Neuron*, 80(4):1010–1024.

Lepousez, G., Nissant, A., and Lledo, P.-M. (2015). Adult Neurogenesis and the Future of the Rejuvenating Brain Circuits. *Neuron*, 86(2):387–401.

Lettvin, J. Y. and Maturana, H. R. (1959). What the frog's eye tells the frog's brain. *Proceedings of the ...*, pages 233–258.

Li, Y., Du, X.-f., Liu, C.-s., Wen, Z.-l., and Du, J.-l. (2012a). Reciprocal regulation between resting microglial dynamics and neuronal activity in vivo. *Developmental cell*, 23(6):1189–1202.

Li, Y., Fitzpatrick, D., and White, L. E. (2006). The development of direction selectivity in ferret visual cortex requires early visual experience. *Nature neuroscience*, 9(5):676–681.

Li, Y., Lu, H., Cheng, P.-l., Ge, S., Xu, H., Shi, S.-H., and Dan, Y. (2012b). Clonally related visual cortical neurons show similar stimulus feature selectivity. *Nature*.

Lister, J. A., Robertson, C. P., Lepage, T., Johnson, S. L., and Raible, D. W. (1999). Nacre encodes a zebrafish microphthalmia-related protein that regulates neural-crest-derived pigment cell fate. *Development*, 126(17):3757–3767.

Liu, X., Wang, Q., Haydar, T. F., and Bordey, A. (2005). Nonsynaptic GABA signaling in postnatal subventricular zone controls proliferation of GFAP-expressing progenitors. *Nature neuroscience*, 8(9):1179–1187.

Livneh, Y., Adam, Y., and Mizrahi, A. (2014). Odor processing by adult-born neurons. *Neuron*, 81(5):1097–1110.

Lledo, P.-M., Alonso, M., and Grubb, M. S. (2006). Adult neurogenesis and functional plasticity in neuronal circuits. *Nature reviews. Neuroscience*, 7(3):179–193.

Lledo, P.-M., Saghatelyan, A., and Lemasson, M. (2004). Inhibitory interneurons in the olfactory bulb: from development to function. *The Neuroscientist : a review journal bringing neurobiology, neurology and psychiatry*, 10(4):292–303.

Markwardt, S. J., Wadiche, J. I., and Overstreet-Wadiche, L. S. (2009). Input-specific gabaergic signaling to newborn neurons in adult dentate gyrus. *The Journal of Neuroscience*, 29(48):15063–15072.

McLaughlin, T., Hindges, R., and O'Leary, D. D. M. (2003). Regulation of axial patterning of the retina and its topographic mapping in the brain. *Current Opinion in Neurobiology*, 13(1):57–69.

Menini, A. (2009). *The neurobiology of olfaction*. CRC Press.

Meyer, M. P. and Smith, S. J. (2006). Evidence from in vivo imaging that synaptogenesis guides the growth and branching of axonal arbors by two distinct mechanisms. *The Journal of neuroscience : the official journal of the Society for Neuroscience*, 26(13):3604–3614.

Miller, J.-e. K., Ayzenshtat, I., Carrillo-Reid, L., and Yuste, R. (2014). Visual stimuli recruit intrinsically generated cortical ensembles. *Proceedings of the National Academy of Sciences*, 2014:1–9.

Ming, G. L. and Song, H. (2011). Adult Neurogenesis in the Mammalian Brain: Significant Answers and Significant Questions. *Neuron*, 70(4):687–702.

Miyasaka, N., Morimoto, K., Tsubokawa, T., Higashijima, S.-i., Okamoto, H., and Yoshihara, Y. (2009). From the olfactory bulb to higher brain centers: genetic visualization of secondary olfactory pathways in zebrafish. *The Journal of neuroscience : the official journal of the Society for Neuroscience*, 29(15):4756–4767.

Mohajerani, M. H., Chan, A. W., Mohsenvand, M., LeDue, J., Liu, R., McVea, D. a., Boyd, J. D., Wang, Y. T., Reimers, M., and Murphy, T. H. (2013). Spontaneous cortical activity alternates between motifs defined by regional axonal projections. *Nature neuroscience*, 16(10):1426–35.

Moore, G. P., Segundo, J. P., Perkel, D. H., and Levitan, H. (1970). Statistical signs of synaptic interaction in neurons. *Biophysical Journal*, 10(9):876.

Mouret, A., Gheusi, G., Gabellec, M.-M., de Chaumont, F., Olivo-Marin, J.-C., and Lledo, P.-M. (2008). Learning and survival of newly generated neurons: when time matters. *The Journal of neuroscience : the official journal of the Society for Neuroscience*, 28(45):11511–11516.

Mrsic-Flogel, T. D., Hofer, S. B., Creutzfeldt, C., Cloëz-Tayarani, I., Changeux, J.-P., Bonhoeffer, T., and Hübener, M. (2005). Altered map of visual space in the superior colliculus of mice lacking early retinal waves. *The Journal of neuroscience : the official journal of the Society for Neuroscience*, 25(29):6921–6928.

Muldal, A., Lillicrap, T., Richards, B., and Akerman, C. (2014). Clonal Relationships Impact Neuronal Tuning within a Phylogenetically Ancient Vertebrate Brain Structure. *Current Biology*, 24(16):1929–1933.

Mundell, N. a., Beier, K. T., Pan, Y. A., Lapan, S. W., Göz Aytürk, D., Berezovskii, V. K., Wark, A. R., Drokhlyansky, E., Bielecki, J., Born, R. T., Schier, A. F., and Cepko, C. L. (2015). Vesicular stomatitis virus enables gene transfer and transsynaptic tracing in a wide range of organisms. *Journal of Comparative Neurology*, 1663:n/a–n/a.

Munz, M., Gobert, D., Schohl, A., Poquérusse, J., Podgorski, K., Spratt, P., and Ruthazer, E. S. (2014). Rapid Hebbian axonal remodeling mediated by visual stimulation. *Science (New York, N.Y.)*, 344(6186):904–9.

Mütze, J., Iyer, V., Macklin, J. J., Colonell, J., Karsh, B., Petrášek, Z., Schwille, P., Looger, L. L., Lavis, L. D., and Harris, T. D. (2012). Excitation spectra and brightness optimization of two-photon excited probes. *Biophysical journal*, 102(4):934–944.

Nakamura, H. and O'Leary, D. D. (1989). Inaccuracies in initial growth and arborization of chick retinotectal axons followed by course corrections and axon remodeling to develop topographic order. *The Journal of neuroscience : the official journal of the Society for Neuroscience*, 9(11):3776–3795.

Neuroscience, T. (2005). Computational & mathematical modelling of neural systems. peter dayan and larry abbott. *This book addresses neural coding issues with several different types of models (Dayan and Abbott 2001).*

Nevin, L. M., Robles, E., Baier, H., and Scott, E. K. (2010). Focusing on optic tectum circuitry through the lens of genetics. *BMC biology*, 8:126.

Nevin, L. M., Taylor, M. R., and Baier, H. (2008). Hardwiring of fine synaptic layers in the zebrafish visual pathway. *Neural Dev*, 3(1):36.

Niell, C. M., Meyer, M. P., and Smith, S. J. (2004). In vivo imaging of synapse formation on a growing dendritic arbor. *Nature neuroscience*, 7(3):254–260.

Niell, C. M. and Smith, S. J. (2005). Functional imaging reveals rapid development of visual response properties in the zebrafish tectum. *Neuron*, 45(6):941–951.

Nievelstein, R. a., Hartwig, N. G., Vermeij-Keers, C., and Valk, J. (1994). Embryonic development of the mammalian caudal neural tube. *Teratology*, 49(6):445.

Nikolaou, N., Lowe, A. S., Walker, A. S., Abbas, F., Hunter, P. R., Thompson, I. D., and Meyer, M. P. (2012). Parametric Functional Maps of Visual Inputs to the Tectum. *Neuron*, 76(2):317–324.

Nissant, A. and Pallotto, M. (2011). Integration and maturation of newborn neurons in the adult olfactory bulb - from synapses to function. *European Journal of Neuroscience*, 33(6):1069–1077.

Noctor, S. C., Flint, A. C., Weissman, T. A., Dammerman, R. S., and Kriegstein, A. R. (2001). Neurons derived from radial glial cells establish radial units in neocortex. *Nature*, 409(6821):714–720.

Ohki, K., Chung, S., Ch'ng, Y. H., Kara, P., and Reid, R. C. (2005). Functional imaging with cellular resolution reveals precise micro-architecture in visual cortex. *Nature*, 433(7026):597–603.

Ohtsuki, G., Nishiyama, M., Yoshida, T., Murakami, T., Histed, M., Lois, C., and Ohki, K. (2012). Similarity of visual selectivity among clonally related neurons in visual cortex. *Neuron*, 75(1):65–72.

Orger, M. B., Gahtan, E., Muto, A., Page-McCaw, P., Smear, M. C., and Baier, H. (2009). Behavioral screening assays in zebrafish. *Essential Zebrafish Methods: Genetics and Genomics: Genetics and Genomics*, page 113.

Panzanelli, P., Bardy, C., Nissant, A., Pallotto, M., Sassoè-Pognetto, M., Lledo, P.-M., and Fritschy, J.-M. (2009). Early synapse formation in developing interneurons of the adult olfactory bulb. *The Journal of neuroscience : the official journal of the Society for Neuroscience*, 29(48):15039–15052.

Paquet, D., Bhat, R., Sydow, A., Mandelkow, E.-m., Berg, S., Hellberg, S., Fälting, J., Distel, M., Köster, R. W., Schmid, B., and Haass, C. (2009). Technical advance A zebrafish model of tauopathy allows in vivo imaging of neuronal cell death and drug evaluation. *The Journal of Clinical Investigation*, 119(5):1382–1395.

Parichy, D. M. (2015). Advancing biology through a deeper understanding of zebrafish ecology and evolution. *eLife*, 4:1–11.

Park, H. C., Kim, C. H., Bae, Y. K., Yeo, S. Y., Kim, S. H., Hong, S. K., Shin, J., Yoo, K. W., Hibi, M., Hirano, T., Miki, N., Chitnis, a. B., and Huh, T. L. (2000). Analysis of upstream elements in the HuC promoter leads to the establishment of transgenic zebrafish with fluorescent neurons. *Developmental biology*, 227(2):279–293.

Paton, J. A. and Nottebohm, F. N. (1984). Neurons generated in the adult brain are recruited into functional circuits. *Science*, 225(4666):1046–1048.

Petreanu, L. and Alvarez-Buylla, A. (2002). Maturation and death of adult-born olfactory bulb granule neurons: role of olfaction. *The Journal of neuroscience : the official journal of the Society for Neuroscience*, 22(14):6106–6113.

Pietri, T., Roman, A.-C., Guyon, N., Romano, S. a., Washbourne, P., Moens, C. B., de Polavieja, G. G., and Sumbre, G. (2013). The first mecp2-null zebrafish model shows altered motor behaviors. *Frontiers in neural circuits*, 7(July):118.

Platel, J. C., Dave, K. a., Gordon, V., Lacar, B., Rubio, M. E., and Bordey, A. (2010). NMDA Receptors Activated by Subventricular Zone Astrocytic Glutamate Are Critical for Neuroblast Survival Prior to Entering a Synaptic Network. *Neuron*, 65(6):859–872.

Platel, J. C., Dupuis, A., Boisseau, S., Villaz, M., Albrieux, M., and Brocard, J. (2007). Synchrony of spontaneous calcium activity in mouse neocortex before synaptogenesis. *European Journal of Neuroscience*, 25(4):920–928.

Platel, J.-C., Heintz, T., Young, S., Gordon, V., and Bordey, A. (2008). Tonic activation of GLUK5 kainate receptors decreases neuroblast migration in whole-mounts of the subventricular zone. *The Journal of physiology*, 586(16):3783–3793.

Politis, M. and Lindvall, O. (2012). Clinical application of stem cell therapy in Parkinson's disease. *BMC Medicine*, 10(1):1.

Pologruto, T. A., Sabatini, B. L., and Svoboda, K. (2003). Scanimage: flexible software for operating laser scanning microscopes. *Biomed. Eng. Online*, 2(1):13.

Portugues, R. and Engert, F. (2009). The neural basis of visual behaviors in the larval zebrafish. *Current Opinion in Neurobiology*, 19(6):644–647.

Pouille, F. and Scanziani, M. (2001). Enforcement of temporal fidelity in pyramidal cells by somatic feed-forward inhibition. *Science (New York, N.Y.)*, 293(5532):1159–1163.

Preuss, S., Trivedi, C., vomBerg Maurer, C., Ryu, S., and Bollmann, J. (2014). Classification of Object Size in Retinotectal Microcircuits. *Current Biology*, 24(20):2376–2385.

Pujol, J., Vendrell, P., Junqué, C., Martí-Vilalta, J. L., and Capdevila, a. (1993). When does human brain development end? Evidence of corpus callosum growth up to adulthood. *Annals of neurology*, 34(1):71–75.

Purves, D. (2012). *Neuroscience*. Sinauer Associates.

Raichle, M. E., MacLeod, A. M., Snyder, A. Z., Powers, W. J., Gusnard, D. A., and Shulman, G. L. (2001). A default mode of brain function. *Proceedings of the National Academy of Sciences*, 98(2):676–682.

Rakic, P. (1988). Specification of cerebral cortical areas. *Science*, 241(4862):170–176.

Ramdya, P. and Engert, F. (2008). Emergence of binocular functional properties in a monocular neural circuit. *Nature neuroscience*, 11(9):1083–1090.

Recher, G., Jouralet, J., Brombin, A., Heuzé, A., Mugniery, E., Hermel, J.-M., Desnoulez, S., Savy, T., Herbomel, P., Bourrat, F., Peyriéras, N., Jamen, F., and Joly, J.-S. (2013). Zebrafish midbrain slow-amplifying progenitors exhibit high levels of transcripts for nucleotide and ribosome biogenesis. *Development (Cambridge, England)*, 140(24):4860–9.

Robles, E., Filosa, a., and Baier, H. (2013). Precise Lamination of Retinal Axons Generates Multiple Parallel Input Pathways in the Tectum. *Journal of Neuroscience*, 33(11):5027–5039.

Robles, E., Smith, S. J., and Baier, H. (2011). Characterization of genetically targeted neuron types in the zebrafish optic tectum. *Frontiers in neural circuits*, 5(February):1.

Rochefort, C., Gheusi, G., Vincent, J.-D., and Lledo, P.-M. (2002). Enriched odor exposure increases the number of newborn neurons in the adult olfactory bulb and improves odor memory. *The Journal of neuroscience*, 22(7):2679–2689.

Rochefort, N. L., Narushima, M., Grienberger, C., Marandi, N., Hill, D. N., and Konnerth, A. (2011). Development of direction selectivity in mouse cortical neurons. *Neuron*, 71(3):425–432.

Romano, S., Pietri, T., Pérez-Schuster, V., Jouary, A., Haudrechy, M., and Sumbre, G. (2015). Spontaneous Neuronal Network Dynamics Reveal Circuit's Functional Adaptations for Behavior. *Neuron*, pages 1070–1085.

Rothenaigner, I., Krecsmarik, M., Hayes, J. a., Bahn, B., Lepier, A., Fortin, G., Götz, M., Jagasia, R., and Bally-Cuif, L. (2011). Clonal analysis by distinct viral vectors identifies bona fide neural stem cells in the adult zebrafish telencephalon and characterizes their division properties and fate. *Development (Cambridge, England)*, 138(8):1459–1469.

Ruthazer, E. S. and Aizenman, C. D. (2010). Learning to see: Patterned visual activity and the development of visual function. *Trends in Neurosciences*, 33(4):183–192.

Ruthazer, E. S. and Cline, H. T. (2004). Insights into Activity-Dependent Map Formation from the Retinotectal System: A Middle-of-the-Brain Perspective. *Journal of Neurobiology*, 59(1):134–146.

Sakaguchi, D. S. and Murphey, R. K. (1985). Map formation in the developing Xenopus retinotectal system: an examination of ganglion cell terminal arborizations. *The Journal of neuroscience : the official journal of the Society for Neuroscience*, 5(12):3228–3245.

Sato, T., Hamaoka, T., Aizawa, H., Hosoya, T., and Okamoto, H. (2007a). Genetic single-cell mosaic analysis implicates ephrinB2 reverse signaling in projections from the posterior tectum to the hindbrain in zebrafish. *The Journal of neuroscience : the official journal of the Society for Neuroscience*, 27(20):5271–5279.

Sato, Y., Sato, Y., Kasai, T., Kasai, T., Nakagawa, S., Nakagawa, S., Tanabe, K., Tanabe, K., Watanabe, T., Watanabe, T., Kawakami, K., Kawakami, K., Takahashi, Y., and Takahashi, Y. (2007b). Stable integration and conditional expression of electroporated transgenes in chicken embryos. *Developmental biology*, 305(2):616–24.

Satou, C., Kimura, Y., Hirata, H., Suster, M. L., Kawakami, K., and Higashijima, S.-i. (2013). Transgenic tools to characterize neuronal properties of discrete populations of zebrafish neurons. *Development (Cambridge, England)*, 140(18):3927–31.

Schoonheim, P. J., Arrenberg, A. B., Del Bene, F., and Baier, H. (2010). Optogenetic localization and genetic perturbation of saccade-generating neurons in zebrafish. *The Journal of neuroscience : the official journal of the Society for Neuroscience*, 30(20):7111–7120.

Scott, E. K. and Baier, H. (2009). The cellular architecture of the larval zebrafish tectum, as revealed by gal4 enhancer trap lines. *Frontiers in neural circuits*, 3(October):13.

Semmelhack, J. L., Donovan, J. C., Thiele, T. R., Kuehn, E., Laurell, E., and Baier, H. (2014). A dedicated visual pathway for prey detection in larval zebrafish. *eLife*, 3:1–19.

Shadlen, M. N. and Newsome, W. T. (1998). The variable discharge of cortical neurons: implications for connectivity, computation, and information coding. *The Journal of neuroscience*, 18(10):3870–3896.

Shaner, N. C., Steinbach, P. a., and Tsien, R. Y. (2005). A guide to choosing fluorescent proteins. *Nature methods*, 2(12):905–909.

Shimokita, E. and Takahashi, Y. (2011). Secondary neurulation: Fate-mapping and gene manipulation of the neural tube in tail bud. *Development Growth and Differentiation*, 53(3):401–410.

Sillito, A. (1975). The contribution of inhibitory mechanisms to the receptive field properties of neurones in the striate cortex of the cat. *The Journal of physiology*, 250(2):305–329.

Smear, M. C., Tao, H. W., Staub, W., Orger, M. B., Gosse, N. J., Liu, Y., Takahashi, K., Poo, M. M., and Baier, H. (2007). Vesicular Glutamate Transport at a Central Synapse Limits the Acuity of Visual Perception in Zebrafish. *Neuron*, 53(1):65–77.

Smith, G. B., Sederberg, A., Elyada, Y. M., Hooser, S. D. V., Kaschube, M., and Fitzpatrick, D. (2015). The development of cortical circuits for motion discrimination. *Nature Neuroscience*, 18(2).

Song, J., Zhong, C., Bonaguidi, M. a., Sun, G. J., Hsu, D., Gu, Y., Meletis, K., Huang, Z. J., Ge, S., Enikolopov, G., Deisseroth, K., Luscher, B., Christian, K. M., Ming, G.-l., and Song, H. (2012). Neuronal circuitry mechanism regulating adult quiescent neural stem-cell fate decision. *Nature*, 489(7414):150–154.

Song, S., Sjöström, P. J., Reigl, M., Nelson, S., and Chklovskii, D. B. (2005). Highly nonrandom features of synaptic connectivity in local cortical circuits. *PLoS Biology*, 3(3):0507–0519.

Spalding, K. L., Bergmann, O., Alkass, K., Bernard, S., Salehpour, M., Huttner, H. B., Bostrom, E., Westerlund, I., Vial, C., Buchholz, B. a., Possnert, G., Mash, D. C., Druid, H., and Frisen, J. (2013). Dynamics of hippocampal neurogenesis in adult humans. *Cell*, 153(6):1219–1227.

Sperry, R. W. (1963). Chemoaffinity in the Orderly Growth of Nerve Fiber Patterns and Connections*. *Proceedings of the National Academy of Sciences of the United States of America*, 50(4):703–710.

Spitzer, N. C. (2006). Electrical activity in early neuronal development. *Nature*, 444(7120):707–712.

Streisinger, G., Walker, C., Dower, N., Knauber, D., and Singer, F. (1981). Production of clones of homozygous diploid zebra fish (Brachydanio rerio). *Nature*, 291(5813):293–296.

Sugiyama, M., Sakaue-Sawano, A., Iimura, T., Fukami, K., Kitaguchi, T., Kawakami, K., Okamoto, H., Higashijima, S.-i., and Miyawaki, A. (2009). Illuminating cell-cycle progression in the developing zebrafish embryo. *Proceedings of the National Academy of Sciences of the United States of America*, 106(49):20812–20817.

Sumbre, G., Muto, A., Baier, H., and Poo, M.-m. (2008). Entrained rhythmic activities of neuronal ensembles as perceptual memory of time interval. *Nature*, 456(7218):102–106.

Suster, M. L., Sumiyama, K., and Kawakami, K. (2009). Transposon-mediated bac transgenesis in zebrafish and mice. *Bmc Genomics*, 10(1):477.

Tabar, V. and Studer, L. (2014). Pluripotent stem cells in regenerative medicine: challenges and recent progress. *Nature reviews. Genetics*, 15(2):82–92.

Tao, H. W. and Poo, M. M. (2005). Activity-dependent matching of excitatory and inhibitory inputs during refinement of visual receptive fields. *Neuron*, 45(6):829–836.

Tawk, M., Bianco, I. H., and Clarke, J. D. W. (2009). Zebrafish. 546:145–151.

Temizer, I., Donovan, J., Baier, H., and Semmelhack, J. (2015). A Visual Pathway for Looming-Evoked Escape in Larval Zebrafish. *Current Biology*, 25(14):1823–1834.

Tseng, Q., Duchemin-Pelletier, E., Deshiere, A., Balland, M., Guillou, H., Filhol, O., and Théry, M. (2012). Spatial organization of the extracellular matrix regulates cell–cell junction positioning. *Proceedings of the National Academy of Sciences*, 109(5):1506–1511.

Turrigiano, G. (2012). Homeostatic synaptic plasticity: Local and global mechanisms for stabilizing neuronal function. *Cold Spring Harbor Perspectives in Biology*, 4(1):1–18.

Vierbuchen, T., Ostermeier, A., Pang, Z. P., Kokubu, Y., Südhof, T. C., and Wernig, M. (2010). Direct conversion of fibroblasts to functional neurons by defined factors. *Nature*, 463(7284):1035–1041.

Westerfield, M. (2000). *The zebrafish book: a guide for the laboratory use of zebrafish (Danio rerio)*. University of Oregon Press.

White, L. E. and Fitzpatrick, D. (2007). Vision and cortical map development. *Neuron*, 56(2):327–338.

White, R. M., Cech, J., Ratanasirintrawoot, S., Lin, C. Y., Rahl, P. B., Burke, C. J., Langdon, E., Tomlinson, M. L., Mosher, J., Kaufman, C., Chen, F., Long, H. K., Kramer, M., Datta, S., Neuberg, D., Granter, S., Young, R. A., Morrison, S., Wheeler, G. N., and Zon, L. I. (2011). DHODH modulates transcriptional elongation in the neural crest and melanoma. *Nature*, 471(7339):518–522.

White, R. M., Sessa, A., Burke, C., Bowman, T., LeBlanc, J., Ceol, C., Bourque, C., Dovey, M., Goessling, W., Burns, C. E., et al. (2008). Transparent adult zebrafish as a tool for in vivo transplantation analysis. *Cell stem cell*, 2(2):183–189.

Wong, R. O. (1999). Retinal waves and visual system development. *Annual review of neuroscience*, 22:29–47.

Xiao, T., Staub, W., Robles, E., Gosse, N. J., Cole, G. J., and Baier, H. (2011). Assembly of lamina-specific neuronal connections by slit bound to type IV collagen. *Cell*, 146(1):164–176.

Yaksi, E. and Friedrich, R. W. (2006). Reconstruction of firing rate changes across neuronal populations by temporally deconvolved ca2+ imaging. *Nature Methods*, 3(5):377–383.

Yamagata, M., Weiner, J. a., and Sanes, J. R. (2002). Sidekicks: Synaptic adhesion molecules that promote lamina-specific connectivity in the retina. *Cell*, 110(5):649–660.

Yang, D., Zhang, Z.-J., Oldenburg, M., Ayala, M., and Zhang, S.-C. (2008). Human embryonic stem cell-derived dopaminergic neurons reverse functional deficit in parkinsonian rats. *Stem cells*, 26(1):55–63.

Yates, P. a., Roskies, a. L., McLaughlin, T., and O'Leary, D. D. (2001). Topographic-specific axon branching controlled by ephrin-As is the critical event in retinotectal map development. *The Journal of neuroscience : the official journal of the Society for Neuroscience*, 21(21):8548–8563.

Yoshimura, Y. and Callaway, E. M. (2005). Fine-scale specificity of cortical networks depends on inhibitory cell type and connectivity. *Nature neuroscience*, 8(11):1552–1559.

Yoshimura, Y., Dantzker, J., and Callaway, E. (2005). excitatory cortical neurons from fine-scale functional networks: Fig 1. *Nature*, 5(February):2005–2005.

Yu, Y.-C., He, S., Chen, S., Fu, Y., Brown, K. N., Yao, X.-H., Ma, J., Gao, K. P., Sosinsky, G. E., Huang, K., and Shi, S.-H. (2012). Preferential electrical coupling regulates neocortical lineage-dependent microcircuit assembly. *Nature*, pages 4–9.

Zhang, M., Liu, Y., Wang, S.-z., Zhong, W., Liu, B.-h., and Tao, H. W. (2011). Functional elimination of excitatory feedforward inputs underlies developmental refinement of visual receptive fields in zebrafish. *The Journal of neuroscience : the official journal of the Society for Neuroscience*, 31(14):5460–5469.

Zhu, P., Fajardo, O., Shum, J., Zhang Schärer, Y.-P., and Friedrich, R. W. (2012). High-resolution optical control of spatiotemporal neuronal activity patterns in zebrafish using a digital micromirror device. *Nature Protocols*, 7(7):1410–1425.

Zou, D.-J., Chesler, A., and Firestein, S. (2009). How the olfactory bulb got its glomeruli: a just so story? *Nature reviews. Neuroscience*, 10(8):611–618.

Zupanc, G. K. H., Hinsch, K., and Gage, F. H. (2005). Proliferation, migration, neuronal differentiation, and long-term survival of new cells in the adult zebrafish brain. *The Journal of comparative neurology*, 488(3):290–319.

Zupanc, G. K. H. and Sîrbulescu, R. F. (2011). Adult neurogenesis and neuronal regeneration in the central nervous system of teleost fish. *European Journal of Neuroscience*, 34(6):917–929.